A Search for Supersymmetric Higgs Bosons in the Di-tau Decay Mode in Proton-Antiproton Collision at 1.8 TeV

by

Amy Lynn Connolly

B.S. (Purdue University, Indiana) 1996
M.A. (University of California, Berkeley) 1998

A dissertation submitted in partial satisfaction of the

requirements for the degree of

Doctor of Philosophy

in

Physics

in the

GRADUATE DIVISION

of the

UNIVERSITY OF CALIFORNIA, BERKELEY

Committee in Charge:
Professor Marjorie Shapiro
Professor Robert Jacobsen
Professor Stephen Derenzo

Fall 2003

The dissertation of Amy Lynn Connolly is approved:

Chair	Date
	Date
	Date

University of California, Berkeley
Fall 2003

Abstract

A Search for Supersymmetric Higgs Bosons in the Di-tau Decay Mode in Proton-Antiproton Collision at 1.8 TeV

by

Amy Lynn Connolly

Doctor of Philosophy in Physics

University of California, Berkeley

Professor Marjorie Shapiro, Chair

A search for directly produced Supersymmetric Higgs Bosons has been performed in the di-tau decay channel in 86.3 ± 3.5 pb^{-1} of data collected by CDF during Run1b at the Tevatron. We search for events where one tau decays to an electron and the other tau decays hadronically. We perform a counting experiment and set limits on the cross section for Higgs production in the high $\tan\beta$ region of the m_A-$\tan\beta$ plane. For a benchmark parameter space point where $m_A = 100$ and $\tan\beta = 50$, we set a 95% confidence level upper limit at 891 pb compared to the theoretically predicted cross section of 122 pb. For events where the tau candidates are not back-to-back, we utilize a di-tau mass reconstruction technique for the first time on hadron collider data. Limits based on a likelihood binned in di-tau mass from non-back-to-back

events alone are weaker than the limits obtained from the counting experiment using the full di-tau sample.

Chair Date

This dissertation is dedicated to

my mom and dad.

Contents

List of Figures

List of Tables

Acknowledgements

Looking back at the many people whose support that I had during the long journey towards completing my Ph.D., I realize that I have been very fortunate. I would like to first thank my parents, to whom this dissertation is dedicated. They are now the proud parents of two physics Ph.D.s and I know they are at least as happy as I am to see this completed. My dad, being a math teacher, fueled my interest in math since I was very young. My mom's supportive words were really valued during the emotional ups and downs that are inevitable in graduate school.

I would also like to acknowledge my grandparents that I wish could have lived to see this completed: Walter A. Connolly, Ruthanna Connolly and Wendell Barlage.

Thank you, Chris, for everything. From always answering "Yes" when I asked, "Do you think everything is going to be okay," to helping me fix my Makefiles to bringing the champagne when I finally got blessed. You're the greatest.

I would like to thank my advisor, Marjorie Shapiro. She urged me to pick a topic that I was genuinely interested in, even if it was not her specialization. Due to Marjorie's always-hectic schedule, on many occasions, meeting with me to discuss my analysis at Fermilab before rushing off to O'Hare meant putting many other people from her busy schedule on hold, which I really appreciated. Sometimes she could be seen making a beeline through the trailers toward my office repeating to people

requesting to speak to her, “I have to talk to my student!” Also, whenever I had a problem to cope with, be it personal or related to my dissertation, she made it a priority to help in whatever way she could.

Thanks also to the other members of my dissertation committee, Bob Jacobsen and Stephen Derenzo, and the other member of my qualifying committee, Robert Cahn.

My first experience in particle physics research was with the ZEUS group at Argonne National Lab under the advisement of Malcolm Derrick during the summer of 1993. I would like to thank that fun group for showing me how exciting this field could be. I would also like to thank Blair Stringfellow and Huan Huang, then at Purdue, for giving me the opportunity to work with them on the STAR project and experience hardware work in a physics lab for the first time.

I would like to thank the LBL group as a whole, they came to feel almost like family and I am going to miss them. I have come a long way since my first year at Berkeley because of the role models that they have been to me.

I want like to specially thank Weiming Yao, who has been almost a second advisor to me. He in fact suggested this analysis to me when I was studying the feasibility of various topics. His expertise in Higgs physics has been very helpful, and his broad hands-on experience in CDF analysis code was at times vital. Whenever I called him

with a question he would stop what he was doing to help me. And he offered many consoling or encouraging words when he could tell that I needed them.

Maurice Garcia-Sciveres was my mentor for several years while we worked on hybrid production and I am grateful for the enormous amount that he taught me about working in the lab.

Fortunately for me, Aaron Dominguez had just completed a search for the same particle at a different collider when he became my office mate in 1999. I am grateful to him for the time he spent helping me at many stages of this analysis.

During one year while I was at LBL, I was privileged to have Henry Frisch at the desk next to mine while he was on sabbatical there. Since then, he has offered me a lot of good advice and many encouraging words.

I was fortunate to have the experience of working on one other CDF analysis before I began the work for this dissertation because David Stuart took me under his wing to assist with the Run 1 CHAMP search. I am grateful for the time that he spent coaching me on my first CDF analysis. Having already worked with him on completing a CDF analysis, getting blessed, showing results at a conference, and writing a paper gave me a lot of confidence when it came to tackling this analysis.

I would also like to thank the conveners of the exotics group at Fermilab, Steve Worm and Stephan Lammel for their helpful suggestions and their assistance in getting this analysis blessed. Thanks to Anton Anastassov, Fedor Ratnikov and Pasha Murat for their helpful suggestions as well.

There were several theorists to whom I am indebted because they took time to sit down with me and deliberate on the many theoretical issues that were important to this analysis. For this, I am grateful to John Campbell, Keith Ellis, Ian Hinchliffe, Steve Mrenna, Michael Spira, and Scott Willenbrock.

I would also like to thank family and friends: Grandma Barlage, Phoebe Mack, Olga Lobban, Tony Affolder, Tim Nelson, Auke-Pieter and Jetske Colijn, Hung-Chung Fang, Julie Walters, John and Gayle Thayer, the Hacketts, the Wolfs, Chris's family, my brother Brian, Robin Walthery, and Brent, Matt and Charlie from Berkeley. Finally, I would like to thank the Old Town School of Folk Music, the national movement for Instant Runoff Voting, and the Fermilab women's book club.

Chapter 1

Introduction

Particle physicists study the most fundamental components of matter and seek to explain the nature of their interactions in concise, elegant physical laws expressed in the language of mathematics. When J.J. Thompson first discovered the electron in 1897, particle physics was born. During the first half of the 20^{th} century, physicists made many discoveries by literally detecting particles falling out of the sky (cosmic rays), while the same scientists tried to explain the particles' relationship to one another and by what processes they could have been produced. The 1930's saw the growth of man-made particle accelerators, at first inspired by J.J. Thompson's first table-top accelerator, so that they could produce these cosmic ray particles on earth[1]. This way, they could control the parameters of the experiment in their attempts to confirm or discredit their theories of particle physics interactions. As the experiments grew and theories became more sophisticated, particle physicists specialized, with some carrying out the experiments and others formulating the theories governing the interactions. Particle physics experiments serve as microscopes probing the most fundamental particles known, and the larger the accelerator, the more powerful the microscope. Consequently, these machines have now grown in size to several kilometers across and have probed distances down to 10^{-19} m, in precise agreement with the theoretical predictions.

[1] The study of cosmic rays, called particle astrophysics, has grown in parallel with the study of particles from man-made accelerators.

Today, the largest particle accelerator in the world is located at Fermi National Accelerator Laboratory in Batavia, Illinois. The "Tevatron," as the machine is called, accelerates protons and anti-protons in opposite directions along a circular path to the highest energies on earth, and collides them head-on at collision points around the ring. Two different detectors sit at separate collision points and measure the energy deposited by the remnants of the proton-anti-proton collisions. The detectors, named CDF (Collider Detector at Fermilab) and DØ, are each operated by a collaboration of hundreds of physicists. The Tevatron provides an ideal environment to search for the heaviest fundamental particles yet to be discovered. The Higgs Boson is one fundamental particle that has so far escaped detection, and is thought to be responsible for the origin of mass. Supersymmetry is a proposed new symmetry between bosons and fermions whose existence has also not yet been confirmed by observation.

Here, we report on a search for supersymmetric Higgs bosons produced from proton-anti-proton collisions recorded by the CDF detector at the Tevatron. We search for these yet undiscovered particles in their decays to two tau leptons. This is the first time that a search for Higgs Bosons has been carried out in this channel. We also demonstrate for the first time from data the feasibility of a technique to reconstruct the mass of a candidate di-tau system. The analysis also provides a measurement of the cross section for the production of Z bosons, since the decay of a Z boson is nearly indistinguishable from the Higgs decay sought after, and so inevitably are observed in the search. Thus, a modest measurement of the already well measured Z production process is presented.

In Chapter 2, the theoretical framework for this measurement is outlined. The Standard Model of particle physics is introduced, and the Minimal Supersymmetric extension to the Standard Model (MSSM) is motivated. A discussion of the mechanism by which Higgs bosons are expected to be produced and decay at the Tevatron is given.

In Chapter 3, the laboratory environment is discussed. A brief description of the Tevatron collider is given. The CDF detector is explained in detail, with emphasis on detector sub-systems that were critical in this analysis.

In Chapter 4, selection of data collected by CDF is discussed. We describe the variables used to select a data sample with optimal sensitivity to Higgs events. We also assess the detector simulation with regard to the variables used for this analysis. For the backgrounds that rely on the simulation for their prediction, we summarize the number of events expected.

In Chapter 5, we discuss the issues related to event generation that are unique to this analysis. We describe the procedures used to modify the Pythia Monte Carlo program for improved modeling of production and decay processes.

In Chapter 6, we estimate the rate of backgrounds that include fake hadronic taus. Tau fake rates are measured from data control samples and these fake rates are applied to the analysis data sample itself. Also, systematics associated with the fake tau backgrounds are quantified.

In Chapter 7, we outline the procedure used to optimize the cuts to maximize sensitivity to signal. First, the optimization is performed by considering only statistical errors. Then, the largest systematics are targeted with a second-pass optimization.

In Chapter 8, the results are presented. We show the track multiplicity of the tau candidates in the final event samples, with the cuts on the numbers of tracks relaxed. There are two experiments performed. The first is a counting experiment that includes both back-to-back and non-back-to-back events. The second is a binned search using the di-tau mass variable that considers only events where the tau candidates are non-back-to-back in the transverse plane.

In Chapter 9, we review what was learned from the analysis and draw conclusions.

In Appendix A, we list the events that pass all of the final analysis cuts, with the back-to-back events shown separately from the non-back-to-back events.

In Appendix B, we outline the selection cuts for both Monte Carlo samples and data control samples.

In Appendix C, we discuss the combinatorics issues that we confront in studies of electron identification variables using $Z \to ee$ samples.

In Appendix D, we describe the estimated sensitivity for this analysis in Run 2A and at the LHC. We also discuss what these experiments may learn from this analysis and offer suggestions for improving the sensitivity beyond that expected from the increased luminosity and center-of-mass energies.

In Appendix E, we outline the procedure for setting limits using the Bayesian method. This method is standard, but we describe it here for completeness.

Chapter 2

Theory and Motivation

2.1 The Standard Model of Particle Physics

The Standard Model (SM) of particle physics was developed in the 1970's and has been astonishingly successful in describing the known particles and their interactions. At this writing the SM does not show any definitive disagreement with any particle physics measurements to date[1]. The SM is a gauge field theory. In particular, fundamental particles are fields which extend in space and time, and predicting the interactions which occur between those fields comes from the assumption that the theory is invariant under gauge transformations.

There are three gauge groups which comprise the theory so that the Standard Model is said to be $SU(3)_{color}$ x $SU(2)_L$ x $U(1)$. $SU(3)_{color}$ describes the strong force and from $SU(2)_L$ x $U(1)$ the Standard Model derives the electromagnetic and electroweak forces.

The fermions in the theory include 6 flavors of quarks and 6 flavors of leptons. The fermion fields are arranged in SU(2) doublets or singlets of definite handedness[2].

$$\begin{pmatrix} u_L \\ d_L \end{pmatrix}, \quad u_R, \quad d_R \quad \begin{pmatrix} \nu_{e\,L} \\ e_L \end{pmatrix}, \quad e_R$$

[1]The strong experimental evidence for neutrino oscillations and thus nonzero neutrino masses is often cited as the first evidence for physics beyond the Standard Model. However, since the physics behind neutrino oscillations is believed to be understood (barring a confirmation of the LSND result [1] showing a third mixing angle in the neutrino sector), neutrino oscillations cannot be said to be evidence for "new physics."

[2]A right-handed particle has its spin aligned parallel to its momentum, a left-handed particle anti-parallel

$$\begin{pmatrix} c_L \\ s_L \end{pmatrix}, \quad c_R, \quad s_R \quad \begin{pmatrix} \nu_{\mu\, L} \\ \mu_L \end{pmatrix}, \quad \mu_R$$

$$\begin{pmatrix} t_L \\ b_L \end{pmatrix}, \quad t_R, \quad b_R \quad \begin{pmatrix} \nu_{\tau\, L} \\ \tau_L \end{pmatrix}, \quad \tau_R$$

The left-handed fermions form SU(2) doublets, and we call the upper members "up-type" and the lower members "down-type." The right-handed fermions are SU(2) singlets. Notice that unlike the other fermions, there are no right-handed neutrinos in the theory. This is by construction in the Standard Model, since only left-handed neutrinos are observed in nature[3].

For each gauge group in the theory, every particle has a "charge" associated with it, determining the relative strength with which the particle "feels" the corresponding force. For example, quarks and gluons exhibit a charge associated with the strong force called "color", so named because only quarks with three different colors bind into a colorless baryonic state, just as red, blue and green (r,b,g) light combine to give white light. Two quarks may also bind into colorless mesons, if their colors are opposite (r and $\bar{r}$, for example). The charges associated with $SU(2)_L$ and U(1) are "weak isospin" and "hypercharge," respectively. The third component of the weak isospin is denoted T_3. $T_3 = +\frac{1}{2}$ for up-type fermions, $-\frac{1}{2}$ for down-type fermions,

[3]Since it now appears as though neutrinos are not massless, right-handed neutrino states must then exist. However, they do not interact with any of the gauge fields in the SM, since they are not electrically charged and they are $SU(2)_L$ and $SU(3)_{color}$ singlet states.

and $T_3 = 0$ for right-handed fermions. Hypercharge is defined by $Y = T_3 + Q$ where Q is electric charge. The U(1) gauge boson and the $\mathrm{SU}(2)_L$ gauge boson mix to bring about two physical states, the Z boson and the photon. Electric charge gives the relative strength with which particles couple to the photon. Up-type quarks and their right-handed partners are observed with electric charge $Q = +\frac{2}{3}$. For down-type quarks and their right-handed partners, $Q = -\frac{1}{3}$. Neutrinos have no electric charge, and the remaining leptons have Q = -1. For every particle listed above, there is an anti-particle with identical mass and opposite charge ($Q \to -Q$, $Y \to -Y$, $b, r, g \to \bar{b}, \bar{r}, \bar{g}$).

Six bosons are mediators of the forces and they are: the photon (γ) for the electromagnetic force, the W^+, W^- and Z for the electroweak force, and the gluon for the strong force. W^+ and W^- couple only to the left-handed $\mathrm{SU}(2)_L$ doublets and connect up-type particles to down-type. The γ couples only to electrically charged particles. Both γ and Z only connect fermions of the same flavor (there are no flavor-changing currents at tree-level).

The Standard Model theory faces one major difficulty which comes about when one requires that the theory be gauge invariant: the masses for all particles in the theory vanish. For example, suppose we were to introduce a fermion mass term into the Lagrangian such as:

$$\Delta\mathcal{L}_e = -\frac{m_e^2}{2}\bar{e}_L e_R \; . \tag{2.1}$$

Recall that for $\bar{e}_L$, $Y = +\frac{1}{2}$ and for e_R, $Y = -1$. Therefore, this term would violate the conservation of weak hypercharge, which came from imposing gauge invariance on the theory. In order to introduce mass into the theory, we need an interaction that connects left and right-handed particles while keeping the underlying gauge invariance of the theory intact. This brings us to the Higgs Mechanism.

2.2 The Higgs Mechanism

The Higgs Mechanism offers a way to give particles mass in the Standard Model while preserving the gauge invariance of the theory. A new scalar field is introduced with a gauge invariant potential. It is only when the field takes on a specific ground state that the symmetry is broken. This is called "spontaneous symmetry breaking."

The new scalar field is called the Higgs field, and in the SM it is chosen to be an $SU(2)_L$ doublet of complex scalar fields with weak hypercharge, $Y = +\frac{1}{2}$ (so that hypercharge is conserved in Equation 2.1):

$$\phi = \begin{pmatrix} \phi^+ \\ \phi^0 \end{pmatrix} = \begin{pmatrix} \phi_1 + i\phi_2 \\ \phi_3 + i\phi_4 \end{pmatrix} . \tag{2.2}$$

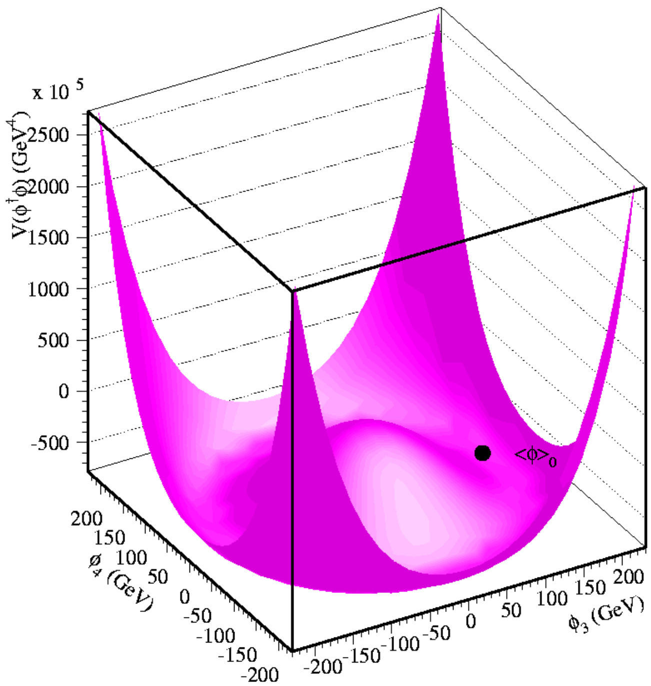

Figure 2.1: *Higgs potential for a Higgs mass of 100 GeV. From [6].*

The Standard Model Lagrangian is appended to include interactions between the scalar field and the gauge bosons and fermions ($\mathcal{L}^{\text{int}}_{\text{Higgs}}$), and also a potential energy term with interactions of the scalar field with itself ($V(\phi^\dagger\phi)$).

$$\mathcal{L}_{\text{Higgs}} = \mathcal{L}^{\text{int}}_{\text{Higgs}} - V(\phi^\dagger\phi) \tag{2.3}$$

where

$$V(\phi^\dagger\phi) = \mu^2(\phi^\dagger\phi) + \lambda(\phi^\dagger\phi)^2 \ . \tag{2.4}$$

When $\mu^2 < 0$, then $V(\phi^\dagger\phi)$ has a "Mexican-hat" shape as in Figure 2.1 with minima for non-zero ϕ. Nature presumably selects a value from the infinite possible minima of Equation 2.4. The possible minima satisfy $\phi_1^2 + \phi_2^2 + \phi_3^2 + \phi_4^2 = -\mu^2/(2\lambda)$. Due to the freedom of SU(2) rotations, we may set $\phi_1 = \phi_2 = \phi_4 = 0$ and write the ϕ with this choice of ground state as simply:

$$\phi_0 = \begin{pmatrix} 0 \\ \frac{h(x)+v}{\sqrt{2}} \end{pmatrix} . \tag{2.5}$$

The vacuum expectation value, v, is $v = \sqrt{-\mu^2/\lambda}$. By replacing the scalar field ϕ in the Lagrangian in Equation 2.3 with ϕ_0 in Equation 2.5, we have a new Lagrangian equivalent to the original one, but with $\mathrm{SU}(2)_L$ spontaneously broken since ϕ has now been chosen with a specific direction. Also, after this substitution mass terms appear in the Lagrangian. For example, Equation 2.3 includes terms which couple the Higgs to electrons:

$$\Delta\mathcal{L}_e = -k_e \bar{e}_L \phi e_R \, . \tag{2.6}$$

By replacing ϕ in Equation 2.6 with ϕ_0 in Equation 2.5, we get a term that looks like:

$$-\frac{1}{\sqrt{2}} k_e v \bar{e}_L e_R \tag{2.7}$$

which is a mass term for an electron with mass $\frac{1}{\sqrt{2}} k_e v$. Here, k_e is a seemingly arbitrary coupling constant which determines the mass of the electron. A different constant appears in the theory for each fermion. As stated earlier, all three neutrino masses are set to zero in the Standard Model due to lack of observation of the right-handed neutrino.

The photon and gluon remain massless, while the masses of the W and Z are now:

$$m_W = \frac{vg}{2} \tag{2.8}$$

$$m_Z = \frac{v}{2}\sqrt{g^2 + g'^2} \tag{2.9}$$

Finally, the Higgs boson itself picks up a mass given by:

$$m_h = \sqrt{-2\mu^2}\ . \tag{2.10}$$

We can see from Equation 2.8 that the value of the vacuum expectation value is revealed to us by a measurement of the Fermi coupling constant, G_F, which relates m_W to g. The muon lifetime and the muon mass give us G_F, and we find that $v \approx 250$ GeV.

So now the theory is fundamentally gauge invariant and yet contains mass terms for fermions and bosons. If the SM is correct, Nature has selected one ground state from many equivalent ground states and spontaneously broken SU(2) symmetry. We may test this Standard Model explanation for the origin of mass by measuring v, m_W, g' and m_Z independently and verifying that Equation 2.9 holds[4], and indeed it does.

[4] The best measurements of m_W and m_Z come from direct measurements at e^+e^- colliders. The weak coupling constant g is deduced from v, m_W and Equation 2.8. Then $g' = \frac{e}{\sqrt{1-\frac{e^2}{g^2}}}$, where e is the electromagnetic charge.

However, before the theory can be on firm footing, the existence of the Higgs Boson must be confirmed by observation. At this writing, no fundamental scalar particle has ever been definitively observed. Indirect measurements of electroweak observables limit m_h in the range 98^{+51}_{-35} GeV at 95% confidence level [7]. The combined data from the four experiments at the LEP e^+e^- collider have put the most stringent lower limit on m_h at 114.4 GeV/c^2 at 95% confidence level [4].

Even if a Higgs Boson consistent with the Standard Model were observed tomorrow, however, that would not mean that the Standard Model is the final theory of fundamental particles and interactions. First, the Standard Model has provided a theory for the origin of mass without providing any clues about the nature of gravity. Further, we expect that the energy scale at which gravitational interactions become important in comparison to the other forces is the Planck scale, $M_P = (G_N)^{\frac{1}{2}} = 1.22 \times 10^{19}$ GeV[5]. But the energy scale for electroweak interactions is set by m_W or v, both of order 100 GeV. This means that there are 17 orders of magnitude in energy scale between the electroweak scale and the Planck scale, with a desert between, with no new interactions predicted in the theory. To some, this is a seemingly unnatural prospect. However, any attempt to introduce new physical theories in this desert, or any attempt to incorporate gravity (and we know that we must incorporate gravity

[5]Two particles with Planck mass M_P separated by a distance $1/M_P$ would each have a gravitational potential energy equal to their rest mass.

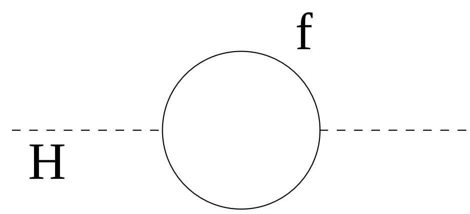

Figure 2.2: *Feynman diagram of the process which gives rise to fermion loop corrections to the Higgs mass.*

for a complete theory of particle interactions), must confront the Hierarchy Problem.

2.3 The Hierarchy Problem

Since $v \approx 250$ GeV, we would also expect the Higgs mass to be of order 100 GeV (the electroweak scale). At tree level, the Higgs mass is $m_H = \sqrt{-2\mu^2}$. A complete calculation of the Higgs mass, however, includes corrections due to fermion loops that interrupt a Higgs Boson as it propagates through space. Such a process is shown in Figure 2.2. For example, the fermion loop in Figure 2.2 brings the following correction to the Higgs mass [2]:

$$\Delta m_H^2 = \frac{|k_f|^2}{16\pi^2}\left[-2\Lambda_{UV}^2 + 6m_f^2\ln(\Lambda_{UV}/m_f) + ...\right] . \tag{2.11}$$

Λ_{UV} is called the ultraviolet cutoff, which may be considered to be the energy scale at which a new theory would come into play and keep the integral from diverging and the term quadratic in Λ_{UV} dominates. For example, suppose one would like to include a theory for gravity at the Planck mass scale (M_P) in the SM. Then the mass correction is of order 10^{36} GeV^2 compared to the expected squared Higgs mass of (100 GeV)^2. This means that some other parameter in the theory would need to be "fine-tuned" to cancel this correction and arrive at a Higgs mass at the electroweak scale. Supersymmetric models provide a way to cancel these large corrections in a natural way, without the need to fine-tune the parameters of the theory.

2.4 The Minimal Supersymmetric Standard Model

Supersymmetry is a proposed new symmetry of nature between fermions and bosons. For every particle in the Standard Model, there would exist a *super-partner*, with spin differing by $\frac{1}{2}$. These super-partners would also add corrections to Higgs mass. For example, a super-partner to a fermion is a scalar particle, whose correction to the Higgs mass comes from the diagram in Figure 2.3 and which looks like:

$$\Delta m_H^2 = \frac{k_S}{16\pi^2}\left[\Lambda_{UV}^2 - 2m_S^2 \ln(\Lambda_{UV}/m_S) + ...\right] . \tag{2.12}$$

Comparing Equation 2.12 with Equation 2.11, we see that the minus-signs appear in the right places for fermion loops and boson loops to cancel one another. In order to cancel the quadratic divergences from fermion loops, we need to introduce two scalar bosons with couplings given by $k_S = |k_f|^2$. In the Minimal Supersymmetric

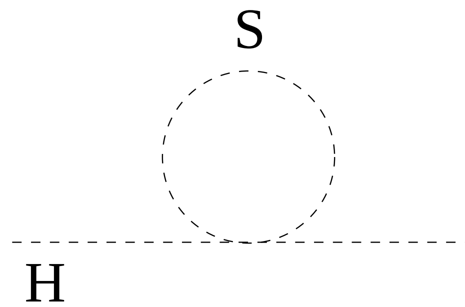

Figure 2.3: *Feynman diagram of the process which gives rise to scalar boson loop corrections to the Higgs mass.*

Standard Model (MSSM), one scalar is introduced as a super-partner to each left-handed fermion and another as a super-partner to each right-handed fermion.

The MSSM contains two Higgs doublets instead of one, the two giving mass to up-type fermions and down-type fermions separately. Each doublet acquires its own vacuum expectation value. Instead of just one physical Higgs boson, five are expected in the MSSM. Consider that in the Standard Model, the single Higgs doublet of complex scalar fields contains four degrees of freedom. Three of those degrees of freedom are "eaten" by the W^+, W^-, and Z as they pick up a mass from the Higgs and with it a new degree of freedom transverse to their momenta. This leaves one physical scalar Higgs boson in the Standard Model. In the MSSM, two Higgs doublets bring eight degrees of freedom to the theory. Again, three degrees of freedom get eaten by the three vector bosons, so that in the MSSM we are left with five physical Higgs bosons: a charged pair, $\mathrm{H}^{\pm}$; two CP-even scalars, H and h (where $m_{\mathrm{h}} < m_{\mathrm{H}}$ by convention); and a CP-odd pseudo-scalar, A.

2.5 Cross Sections and Branching Ratios

At tree level, there are only two parameters in the MSSM Higgs sector and we may choose them to be $\tan\beta$ and m_A[6]. The first parameter, $\tan\beta$, is the ratio of the vacuum expectation values of the two Higgs doublets. It is bound by $0 < \beta < \frac{\pi}{2}$. The second parameter, m_A, is the mass of the pseudo-scalar Higgs. This means that in the MSSM, all of the couplings are just the Standard Model couplings multiplied by factors which only depend on these two parameters. Table 2.1 [3] lists these factors for neutral Higgs couplings to up-type fermions, down-type fermions, and vector bosons. α is the mixing parameter for the neutral Higgs scalars and is bound by $-\frac{\pi}{2} < \alpha < 0$. At tree level,

$$\frac{\sin 2\alpha}{\sin 2\beta} = -\frac{m_A^2 + m_Z^2}{m_H^2 - m_h^2} \tag{2.13}$$

$$\frac{\cos 2\alpha}{\cos 2\beta} = -\frac{m_A^2 - m_Z^2}{m_H^2 - m_h^2} \tag{2.14}$$

As will be motivated below, we are particularly interested in the region of parameter space where $\tan\beta >> 1$. In this region, at tree level, $m_h \rightarrow m_Z$, $m_H \rightarrow m_A$.

[6]Alternatively, the two parameters may be chosen to be $\tan\beta$ and α, the mixing angle for the two neutral scalars.

Higgs Type	$d\bar{d}, s\bar{s}, b\bar{b}$	$u\bar{u}, c\bar{c}, t\bar{t}$	WW ZZ
	$e^+e^-, \mu^+\mu^-, \tau^+\tau^-$		
h	$-\sin\alpha/\cos\beta$	$\cos\alpha/\sin\beta$	$\sin(\beta-\alpha)$
H	$\cos\alpha/\cos\beta$	$\sin\alpha/\sin\beta$	$\cos(\beta-\alpha)$
A	$-i\gamma_5\tan\beta$	$-i\gamma_5\cot\beta$	0

Table 2.1: *The Standard Model Higgs couplings need to be multiplied by these factors, at tree level, to get the appropriate MSSM couplings.*

Therefore, from Equations 2.13 and 2.14, when $\tan\beta$ is large, $\alpha \to 0$. In this same region, one of the neutral Higgs scalars is always degenerate in mass with the pseudo-scalar, with nearly identical couplings. For $m_A \lesssim 120$ GeV, $m_A \approx m_h$ and for $m_A \gtrsim 120$ GeV, $m_A \approx m_H$. Throughout this thesis, we will simply use h to denote the scalar Higgs which is degenerate with the A particle for any value of m_A.

Notice that the coupling of A to down-type fermions is enhanced by $\tan\beta$. This means that at the Tevatron, the cross section for direct production of A through a bottom quark loop as in Figure 2.4 is proportional to $(\tan\beta)^2$. The h coupling to down-type fermions is enhanced by $\cos\alpha/\cos\beta$ [7], so at large $\tan\beta$ where $\cos\beta$ is small (and $\cos\alpha \approx 1$), the cross section for direct production of h through a bottom quark loop can also be sizable. The expected cross sections [5] for direct production

[7] At large $\tan\beta$, $\alpha - \beta \to \frac{\pi}{2}$, so $\cos\alpha/\cos\beta \to \frac{\pm 1}{\cos\beta}$.

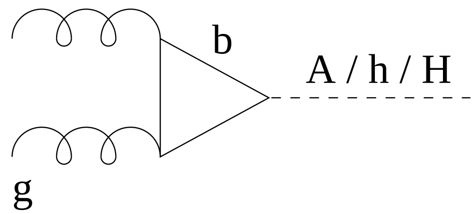

Figure 2.4: *The dominant process for producing MSSM Higgs boson directly at the Tevatron.*

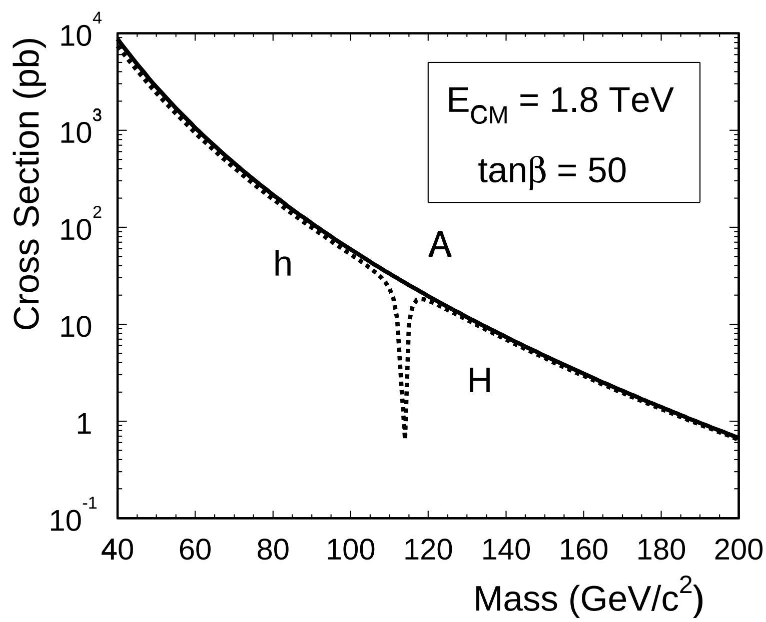

Figure 2.5: *Cross section for direction production of Higgs bosons in the MSSM at the Tevatron in Run 1.*

of neutral Higgs bosons at the Tevatron are plotted against m_A for $\tan\beta = 50$ in Figure 2.5 [5]. In the same high $\tan\beta$ region, A/h decay predominantly to fermions (approximately 90% to $b\bar{b}$ and 9% to $\tau\bar{\tau}$), even at large mass. This is in contrast to the Standard Model, where the Higgs couples predominantly to fermions at low mass (below about 120 GeV), but at high mass the Higgs branching ratio to fermions is swamped by the decay to W^+W^-. Because A is CP odd, it does not couple to vector bosons. This together with its enhanced coupling to down-type fermions at large $\tan\beta$ means that A still decays predominantly into $b\bar{b}$ and $\tau\bar{\tau}$ even beyond 300 GeV when the decay to $t\bar{t}$ would begin to turn on in the Standard Model. The branching ratios for h are very similar. At large mass, H lacks the W^+W^- turn-on as well, because $\cos(\beta - \alpha)$ vanishes in this region. Since both A and h have enhanced direct production cross sections and branching ratios to fermions at large $\tan\beta$, one can search for both A and h at once by searching for their decays to fermions. Decays to $b\bar{b}$ are expected to be swamped by the production of $b\bar{b}$ pairs, so we search for Higgs bosons decaying to τ pairs.

2.6 Experimental Limits on MSSM Higgs Bosons

Figure 2.6 shows the regions of the m_A-$\tan\beta$ plane that have been excluded by direct searches for Higgs production at colliders. Previous direct searches for Higgs bosons have constrained the MSSM in the m_A-$\tan\beta$ plane. At the LEP e^+e^- collider, the dominant production mechanisms for producing MSSM Higgs bosons were expected to be *Higgs-strahlung*: $e^+e^- \rightarrow hZ$, and Higgs pair production: $e^+e^- \rightarrow hA$.

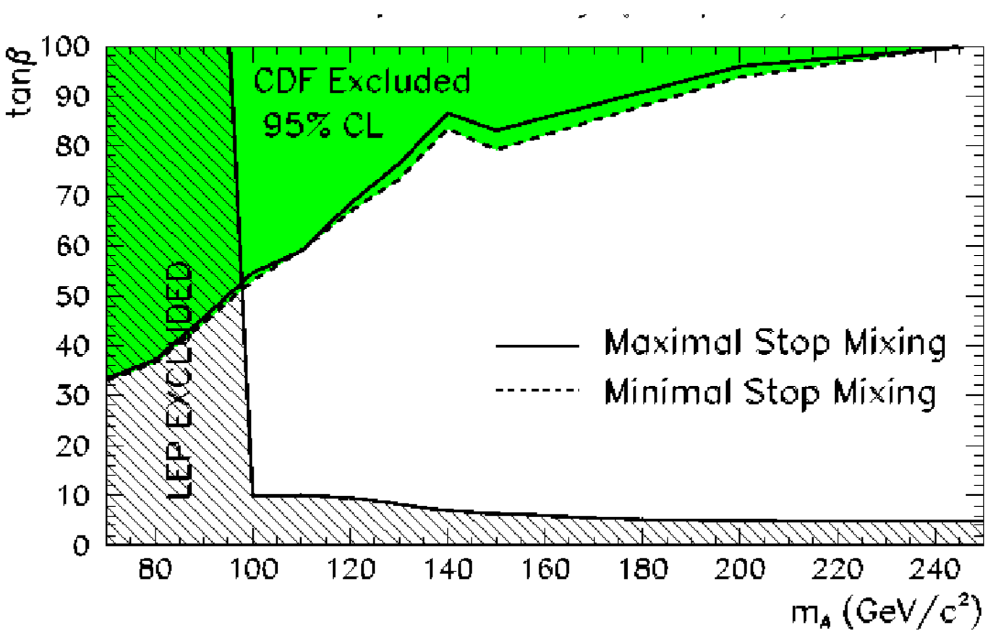

Figure 2.6: *Current limits on the MSSM in the m_A-$\tan\beta$ plane. From [9].*

At low $\tan\beta$, Higgs-strahlung is the dominating process, and the higher $\tan\beta$ region at low m_A is excluded by Higgs pair production. The four LEP experiments combined (ALEPH, L3, OPAL, and DELPHI) have excluded $m_A < 91.9$ GeV, $m_h < 91.0$ GeV and $0.5 < \tan\beta < 2.4$ at 95% confidence level [8]. A search has also been performed at CDF for MSSM Higgs bosons produced in association with two b quarks: $gg, q\bar{q} \to A/hb\bar{b} \to b\bar{b}$ [9]. Since the $A/hb\bar{b}$ coupling is proportional to $\tan\beta$, the cross-section for this process is also proportional to $(\tan\beta)^2$. The exclusion region for this search is shown in Figure 2.6.

Chapter 3

Experimental Apparatus

3.1 The Tevatron

The Tevatron is the highest energy particle accelerator on earth. Located in Batavia, IL, the Run 1 Tevatron accelerated proton and anti-proton beams to energies of 900 GeV each for a total center of mass energy of 1.8 TeV. The beams were made to collide at two interaction points along their opposing circular paths. At these interaction points sat particle detectors designed to study these collisions. Figure 3.1 shows a schematic view of the Run 1 accelerator complex. The machine has been upgraded to deliver data at a higher rate at a higher center-of-mass energy (1.96 TeV) for the current Run 2 stage of data taking. In what follows we give an overview of the machine that accelerated and collided the beams during Run 1, when the collisions being studied in this thesis occurred.

3.1.1 Proton Source

Each 900 GeV proton [10] at the Tevatron had originated from a cylinder of compressed hydrogen gas (H_2). Hydrogen atoms were stripped of their electrons in an electric field and the resulting protons then picked up two electrons each to form a hydrogen ion, H^-, through direct contact with Cesium metal. Thus, the protons underwent their first stages of acceleration in the form of H^- ions. The protons needed

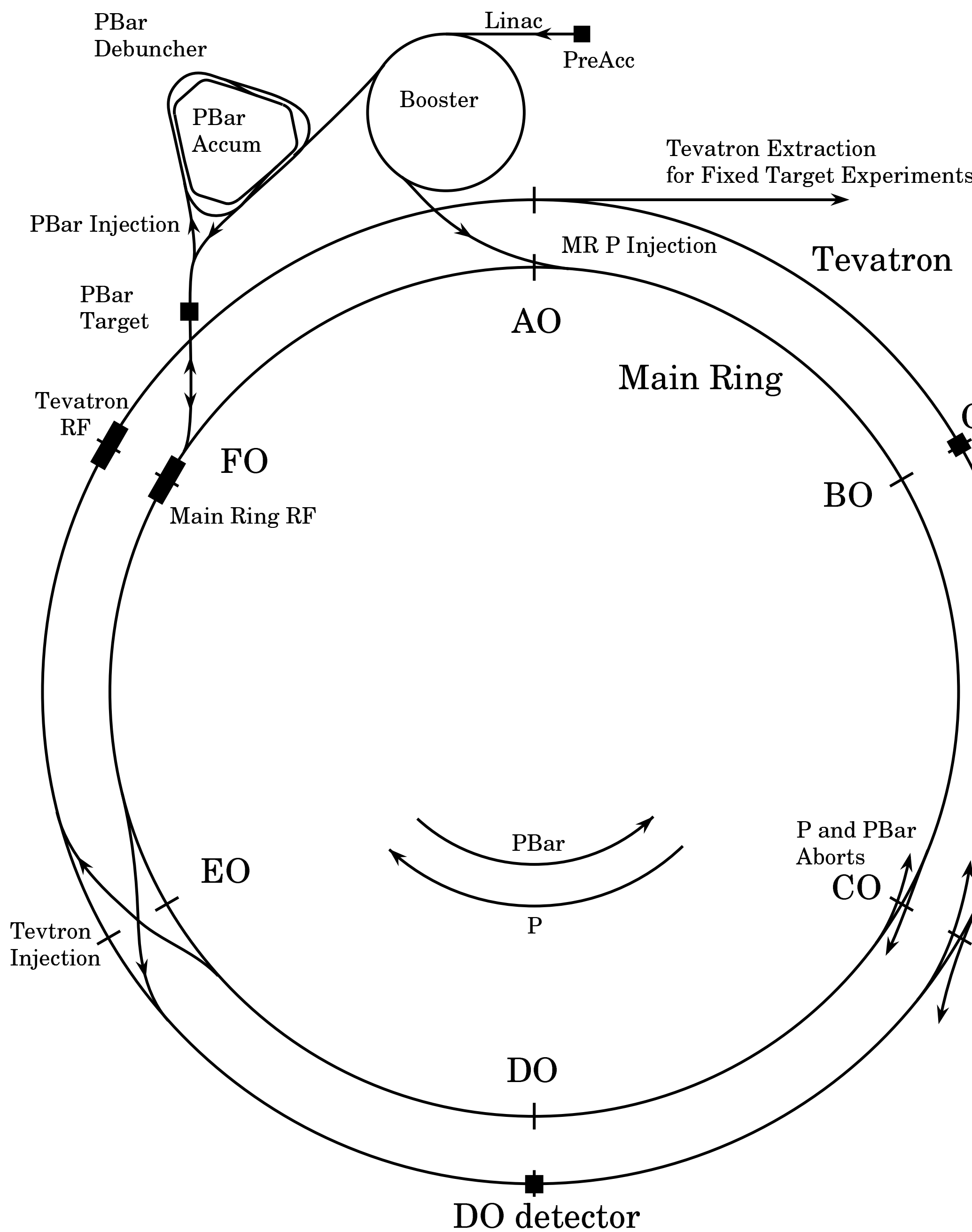

Figure 3.1: *Fermi National Accelerator Laboratory complex. From [27].*

to be accelerated in many stages due to the limitations in energy ranges handled by each machine type[28]. The first stage was a Cockroft-Walton pre-accelerator, a DC voltage divider that accelerated the ions to 750 keV. Next, the ions were accelerated to 400 MeV in a linear accelerator (LINAC) [11]. A LINAC is designed such that the particles are exposed to only one polarity of an oscillating electric field, and are shielded from the field when it is in the opposite polarity. At the end of the LINAC, the ions were stripped of their two electrons as they passed through a thin copper foil, leaving bare protons for the remaining stages of acceleration. These protons then entered the Booster, a 475 m circumference synchrotron accelerator. In a way similar to the LINAC, on each turn, the particles would see an oscillating electric field only in one polarity. A synchrotron takes advantage of a phenomenon known as "phase stability" and gives particles a kick on each turn as the frequency of the electric field is increased. After 20,000 turns, the protons would reach 8 GeV and were then ready to be injected into the Main Ring, also a synchrotron accelerator, but 6.28 km in circumference. In the Main Ring, the protons were accelerated to 150 GeV. Finally, the protons entered their final stage, the Tevatron, where they were accelerated to 900 GeV. The Tevatron [12] used super-conducting magnets for steering and focusing the beams, whereas all other accelerators at the lab used conventional electromagnets.

3.1.2 Anti-proton Source

A beam of anti-protons [13] is more difficult to produce than a beam of protons since anti-protons are not present in ordinary matter. A beam of 120 GeV protons was extracted from the Main Ring and is forced to collide with a Tungsten target. Many secondary particles would be produced from the nuclear interactions that occurred between the beam and the target, including some anti-protons. These secondary particles were focused into a beam with a Lithium lens, and anti-protons were selected by using a pulsed magnet as a mass spectrometer. The anti-protons were then sent to the Debuncher [14], which would take a beam with pulses of particles narrow in time and wide in energy spread and output a beam constrained in energy and spread out in time, again taking advantage of the phase stability feature. Next, the Accumulator would take pulses of anti-protons from the Debuncher and "stack" them for several hours or days at a rate of 4×10^{10} per hour. Both the Debuncher and the Accumulator used stochastic cooling [15] to make the beam of anti-protons more uniform in energy, position, and angles. When 100×10^{10} anti-protons were stored in the Accumulator [16], the anti-protons were reverse injected into the Main Ring where they are accelerated to 150 GeV before they were passed to the Tevatron for the final stage of acceleration to 900 GeV.

3.1.3 Collisions

When the Run 1 Tevatron was in colliding mode, six bunches of 2×10^{11} protons and six bunches of 3×10^{10} anti-protons were injected into the ring in opposite directions. Each bunch was 50 cm in length. Once the bunches were accelerated to 900 GeV, they were made to collide at two collision points. The CDF and DØ detectors sat at these collision points. The collisions occurred every 3.5 μs for runs up to 20 hours long. At the completion of a run, the ring was emptied and refilled with new bunches of protons and anti-protons. During a given run, the exact position of the collisions was well described by a Gaussian along the direction parallel to the beam ($\sigma \approx 30$ cm) and transverse to the beam ($\sigma \approx 35$ μm).

Instantaneous luminosity is given by the following equation:

$$\mathcal{L} = \frac{N_p N_{\bar{p}} B f_0}{4\pi\sigma^2} \tag{3.1}$$

where N_p is the number of protons per bunch, $N_{\bar{p}}$ is the number of anti-protons per bunch, B is the number of bunches of each type, f_0 is the revolution frequency of the bunches, and σ is a measure of the width of a bunch. During a given run, the transverse spread of the beam degraded and collisions caused losses to occur, so that the instantaneous luminosity fell off exponentially. Table 3.1 shows the peak and average instantaneous luminosities achieved during Run 1a (1992-1993) and Run 1b

Run	Average $\mathcal{L}$	Peak $\mathcal{L}$
Run 1a	$0.54 \times 10^{31} cm^{-2} s{-1}$	$0.92 \times 10^{31} cm^{-2} s^{-1}$
Run 1b	$1.6 \times 10^{31} cm^{-2} s{-1}$	$2.8 \times 10^{31} cm^{-2} s^{-1}$

Table 3.1: *Average and peak instantaneous luminosities during Run I of the Tevatron, from [17].*

(1994-1995) of the Tevatron.

3.2 The CDF Detector

The Run 1 Collider Detector at Fermilab (CDF) sat at one of the six collision points (named B$\emptyset$) along the Tevatron ring. CDF was 5,000 tons, and consisted of many detector sub-systems which in combination allowed us to make precise measurements of the energy, momentum and trajectory of a particle that emerged from a collision. Figure 3.3 is a three-dimensional illustration of the CDF detector. In subsections 3.2.1-3.2.5, we give a description of each detector sub-system in CDF. Figure 3.2 is a schematic drawing of a cross-section of one quadrant of CDF.

The Run 1 CDF detector was a cylindrical detector with its axis along the beamline, and was forward-backward symmetric about the nominal collision point. This nominal collision point defined $x = 0, y = 0, z = 0$ for the CDF coordinate system,

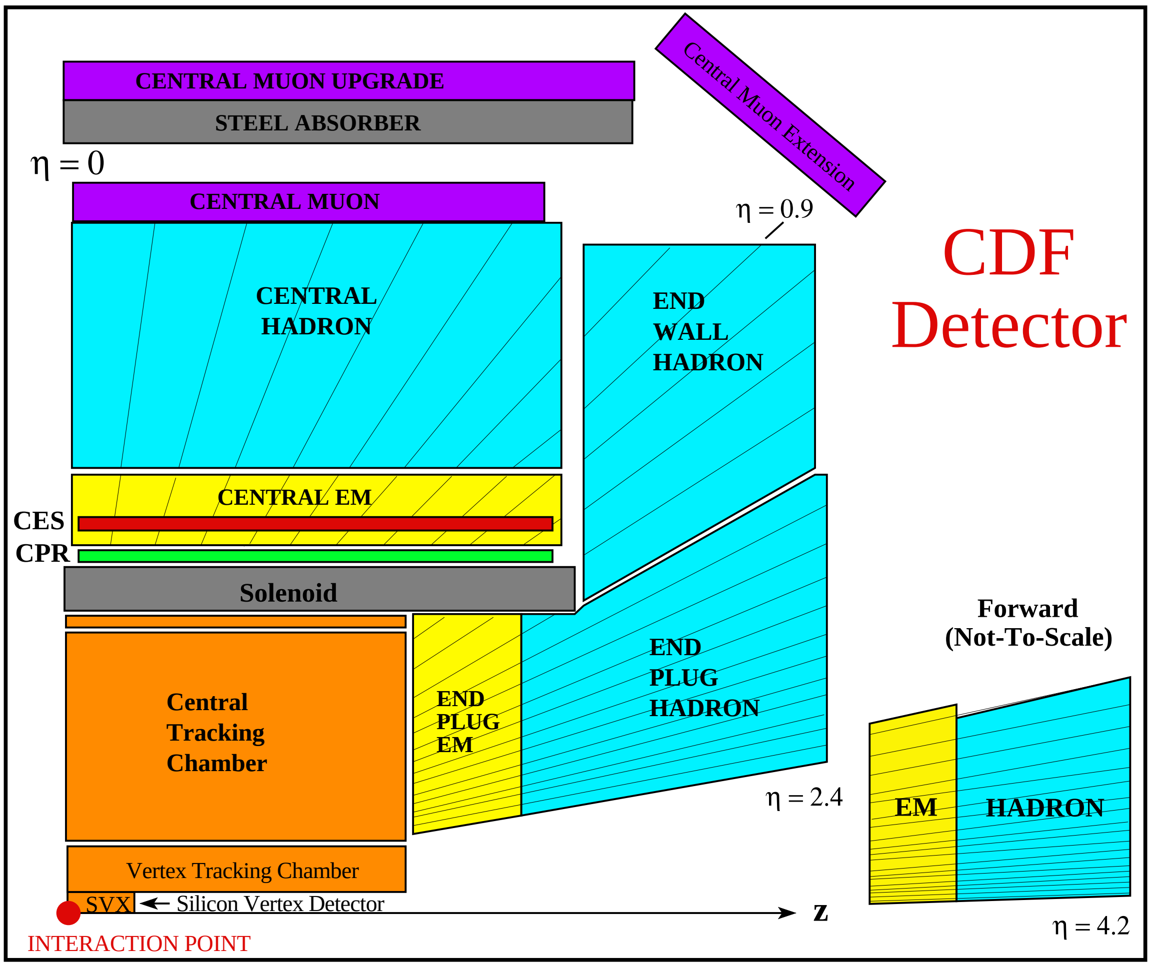

Figure 3.2: *Schematic of the Collider Detector at Fermilab. From [27].*

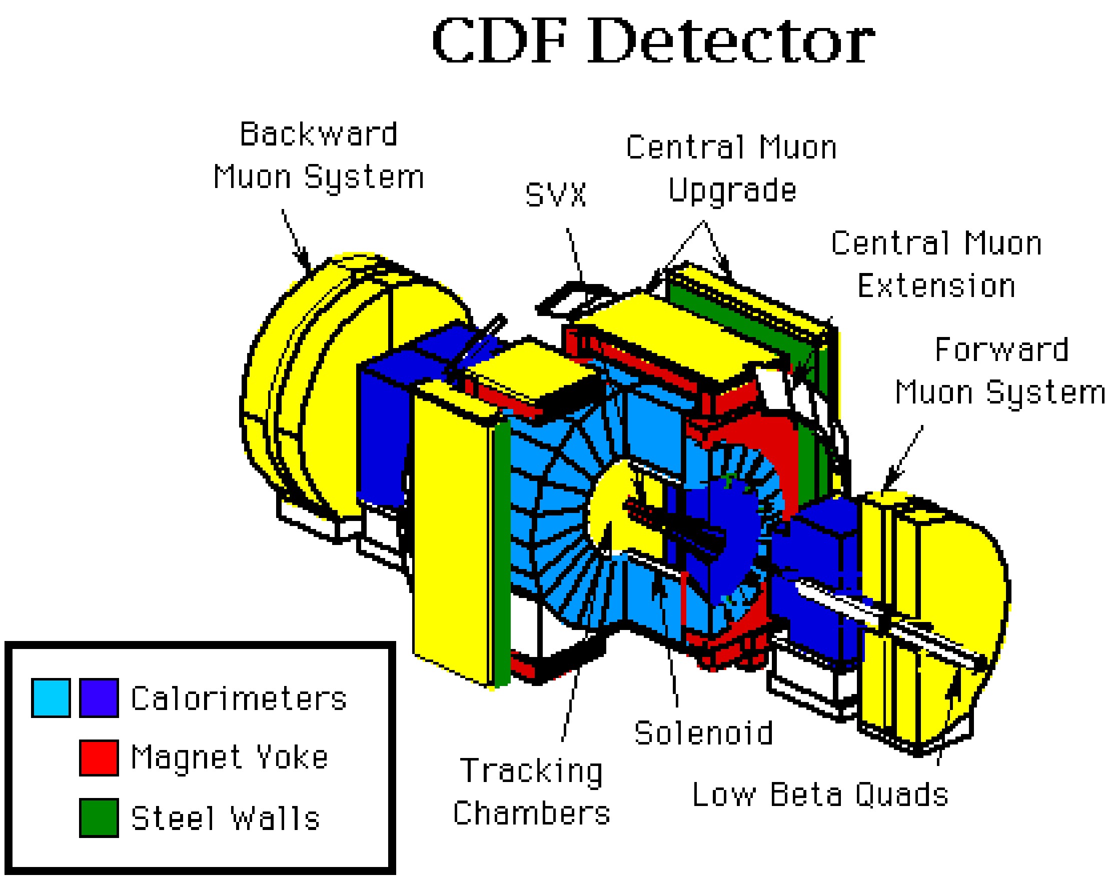

Figure 3.3: *Three dimensional rendering of the Collider Detector at Fermilab. From [27].*

chosen to be right-handed. The direction of the proton beam, which ran clockwise around the ring as observed from above, was the direction of positive z. "Up" was the positive y direction, so x was in the plane of the Tevatron, pointing radially outward from the center of the machine. The polar angle, θ, ran from 0 to π, with $\theta = 0$ along the positive z axis. We often use pseudo-rapidity η in place of θ because of its Lorentz-invariant properties. It is defined as:

$$\eta = -\log[\tan(\theta/2)] \tag{3.2}$$

Detector pseudo-rapidity (η_d) is the pseudo-rapidity of a particle as seen by the detector (assuming the particle originated from $z = 0$). For a particle which originates from the vertex at $z \neq 0$, $\eta \neq \eta_d$. The azimuthal angle, ϕ, is measured relative to the positive x direction, taking on values up to 2π as it wraps around the beam.

3.2.1 Calorimetry

Calorimeters measure the energy of an incident particle by detecting the energy deposition of that particle and its decay products as they are slowed by a dense medium. There were two types of calorimeters in use at CDF: electromagnetic, which measure the energy of electrons and photons, and hadronic, which measure the energy of hadrons, such as pions. The calorimetry at CDF was separated into three sections in pseudo-rapidity: central (CEM,CHA) in the region $|\eta| < 1.1$, plug (PEM,PHA) for

$1.1 < |\eta| < 2.4$, and forward (FEM,FHA) for $2.4 < |\eta| < 4.2$. In each η region, the calorimeter was divided into many projective towers in η-ϕ space so that they would point back to the nominal collision point.

EM calorimeters

An electromagnetic calorimeter measures the energy of incident electromagnetically interacting particles (photons and electrons). At CDF, sampling calorimeters were used, so the detector contained alternating layers of absorber and active material. As a particle was incident on the absorbing material, an electromagnetic shower was induced. An electron would radiate a photon, and that photon would produce an electron-positron pair, those electrons would in turn radiate photons, and so on. A shower from an incident photon is very similar, with pair production being the first step in the shower development. In either case, an electromagnetic shower would continue until the energy of each of the bremsstrahlung photons was below the threshold (E_c) for electron pair production. The shower electrons were measured in the active medium between the layers of absorber. The length of a shower induced by an incident particle depends on the type of absorber used. The radiation length X_0 of the absorber is defined by the distance an electron will travel on average before its energy falls to $1/e$ of its energy at incidence due to bremsstrahlung. The lateral size of a shower is set by the Molière radius, $R_M = X_0 E_s / E_c$, where $E_s \approx 21$ MeV.

The central electromagnetic calorimeter (CEM) [18] consisted of 30 layers of lead, each 1/8 inch thick, for a total of 18 radiation lengths of absorber. Interleaved were 5 mm thick layers of polystyrene scintillator serving as the active medium. When shower electrons were incident on the scintillator, it emitted blue light that was wavelength shifted to green light. Then, the green light was transmitted through acrylic light guides to photo-multiplier tubes (PMT's) radially behind the calorimetry. The CEM had 48 wedges, 24 on each side of the $z = 0$ plane, segmented in $15°$ slices in ϕ, each containing 10 towers. Each tower was approximately 0.1 units wide in η.

The CEM was calibrated initially with a test-beam of 50 GeV electrons. During the Run 1 data-taking period, the calibration was periodically measured with ^{137}Cs sources. The measured energy resolution for the CEM was:

$$\sigma(E)/E = 13.7\%/\sqrt{E_T} \oplus 2\% \qquad (3.3)$$

Located just inside the CEM in radius was a pre-radiator detector called the CPR, useful in distinguishing hadrons from electrons.

The plug electromagnetic (PEM) calorimeter was also a sampling calorimeter, with 34 layers of lead each 2.7 mm thick. Here, the active detector medium consisted of proportional tube arrays arranged along copper plated G-10 panels which served as cathode planes. The proportional tubes were filled with a 50% argon, 50% ethane

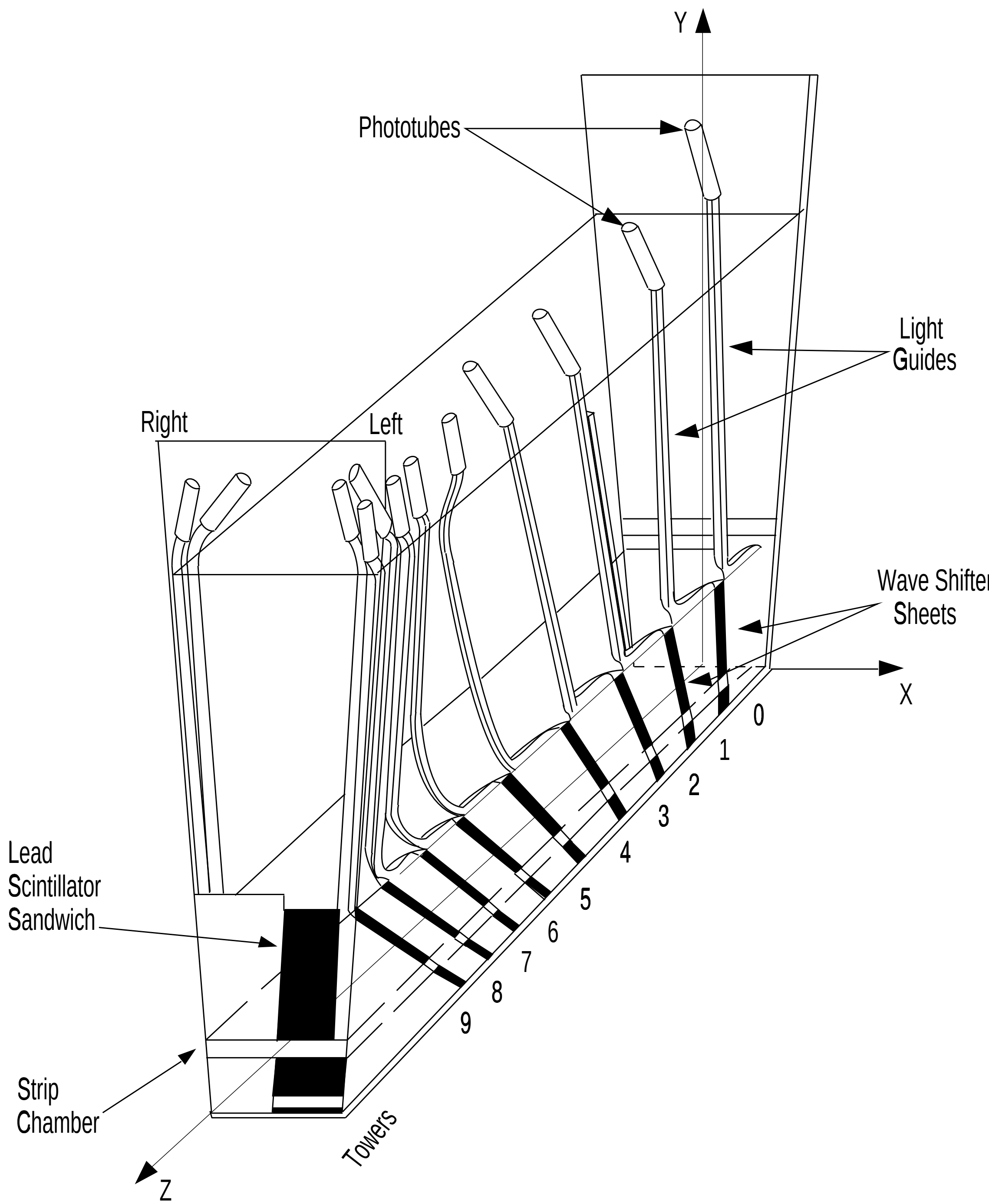

Figure 3.4: *Cross-section of a CEM wedge. From [27].*

gas mixture and contained a high voltage anode wire in the center. Incident shower electrons ionized the gas, and liberated electrons from the gas drifted towards the anode wire, whereby an avalanche of negative charge reached the anode and a positive charge was induce on the cathode plane. The cathode signal was proportional to the energy of the incident particle.

The energy resolution of the PEM was also measured with electrons from a test-beam and found to be:

$$\sigma(E)/E = 22\%/\sqrt{E} \oplus 2\% \tag{3.4}$$

The forward electromagnetic (FEM) calorimeter was also a sampling calorimeter, with 30 layers of antimony strengthened lead (totalling 80% of a radiation length) serving as the absorber. As in the PEM, proportional tube arrays interleaved with the absorber served as the active detector medium.

The energy resolution of the FEM was also measured with test-beam electrons:

$$\sigma(E)/E = 26\%/\sqrt{E} \oplus 2\% \tag{3.5}$$

CES

The Central Electron Strip Chamber (CES) was a proportional strip and wire chamber located six radiation lengths deep in the CEM ($r = 184.15$ cm), where the lateral size of the shower was expected to be maximal. Figure 3.5 shows a segment of the CES. Its purpose was to provide a measurement of the position of electromagnetic showers in the plane perpendicular to the radial direction. In each (east and west) half of the detector, for each 15° section in ϕ, 128 cathode strips measured the shower positions along the z direction. In the region $6.2 < z < 121.2$ cm ($121.2 < |z| < 239.6$ cm), the strip pitch was 1.67 (2.01) cm. There were no strips within 6.2 cm of the $z = 0$ plane. Additionally, in each 15^{o} wedge, 64 anode wires (ganged in pairs) with a 1.45 cm pitch measured the shower position in ϕ. The wires were split into two sections on each half of the detector, $6.2 < |z| < 121.2$ cm and $121.2 < |z| < 239.6$ cm. The resolution for cluster position measurement was $\lesssim 1$ cm in each dimension.

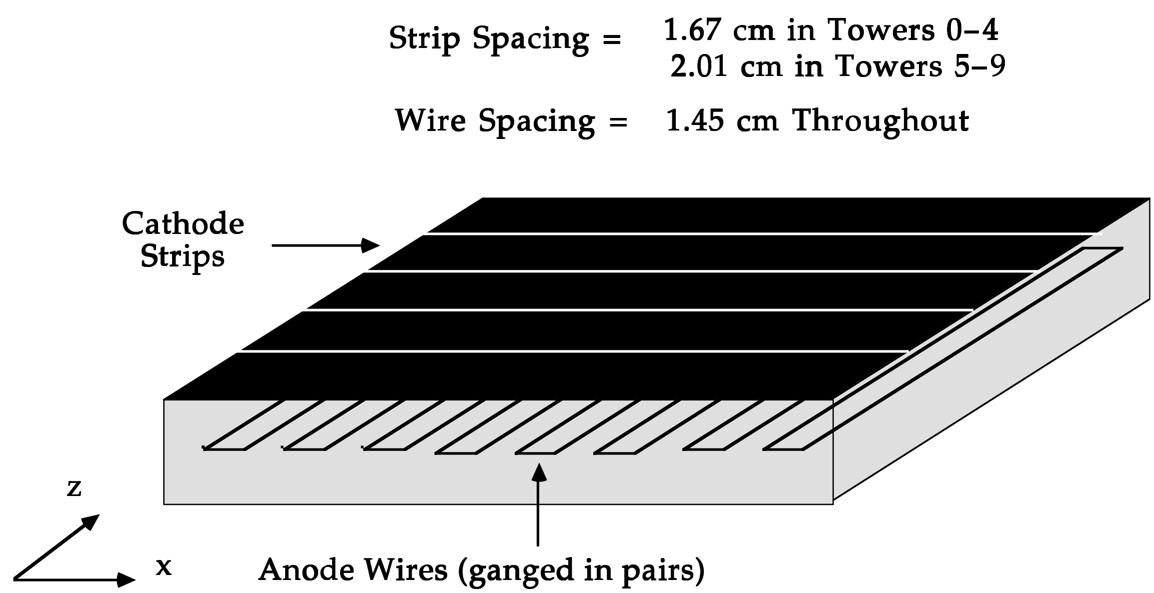

Figure 3.5: *Segment of the CES proportional chamber. From [27].*

HAD calorimeters

The hadronic calorimeters at CDF were also sampling. A shower would develop when an incident hadron produced secondary hadrons through a nuclear collision in the absorber, those secondary hadrons would produce more hadrons through their nuclear interactions and so on. Just as for an electromagnetic shower, the length of a hadronic shower depends on the absorber material used, but the relevant quantity is now the nuclear absorption length, λ. Typically $\lambda \gg X_0$, so hadronic calorimeters need to be much larger and placed behind the electromagnetic calorimeters.

The CDF central hadronic (CHA) [19] calorimeter was situated behind the CEM and it was segmented identically to the CEM in η and ϕ. There were 32 layers of steel 2.5 cm thick, for a total of 4.7 λ, with 1 cm thick plastic scintillator interleaved between the layers of absorber and serving as the active detector medium. Charged particles from the hadronic shower incident on the scintillator would cause light to be emitted which was read out as in the CEM.

The CHA was calibrated before the data taking period began with a beam of 50 GeV test-beam pions incident on each tower at its center. The energy resolution was measured to be:

$$\sigma(E)/E = 50\%/\sqrt{E_T} \oplus 3\% \tag{3.6}$$

Due to the square cylindrical shape of the CHA, particles originating from the interaction point would not traverse all layers of the CHA in the region $0.6 < |\eta| < 1.1$. The WHA sat beyond the CHA in z in the region $0.7 < |\eta| < 1.3$. The construction of the WHA was very similar to the CHA, with 15 layers of steel each 5 cm thick serving as the absorber and layers of plastic scintillator 1.0 cm thick serving as the active detector medium.

The plug hadronic calorimeter (PHA) sat behind the PEM in the region $1.1 < |\eta| < 2.4$. It consisted of 20 layers of steel each 5.1 cm thick serving as absorber with proportional tube arrays sandwiched in between and serving as the active detector medium, just as in the PEM.

The energy resolution of the PHA was measured with test-beam pions:

$$\sigma(E)/E = 90\%/\sqrt{E} \oplus 4\% \tag{3.7}$$

The forward hadronic calorimeter (FHA) contained 27 layers of 5 cm thick steel absorber with ionization chambers 2.5 cm thick interleaved between and serving as the active detector medium. The ionization chambers were rectangular cells filled with 50% argon, 50% ethane gas where ionization was induced from incident charged particles. Three sides of a chamber were aluminum while the third side was a copper cathode pad. A sense wire (50 μm diameter nickel-flashed, gold-plated tungsten) was fixed by molded Ryton plastic plugged in the end of the cell.

The energy resolution of the FHA was also measured with test-beam pions:

$$\sigma(E)/E = 137\%/\sqrt{E} \oplus 4\% \tag{3.8}$$

3.2.2 Tracking

CDF measured the trajectories of charged particles with its three-component tracking system. Sitting at the smallest radius was the Silicon Vertex Detector (SVX), providing high precision measurements of the tracks and allowing secondary vertices to be resolved from the primary vertex. The time projection chamber (VTX) sat further out in radius and measured the position of the collision point along the beam for each event. Beyond the VTX was the Central Tracking Chamber (CTC), measuring the trajectories of the charged particles.

The tracking system was immersed in a 1.4 Tesla magnetic field parallel to the beam, which allowed a determination of the momentum of the particles from the radius of curvature of their tracks through the relation:

$$p = qB\rho \tag{3.9}$$

where p is the particle momentum in the transverse plane, q is its charge, B is the magnetic field strength, and ρ is the radius of curvature.

Silicon Vertex Detector

The Silicon Vertex Detector (SVX′) [20] was a solid-state ionization detector at small radius which served two purposes. First, it was designed to measure the secondary vertices of particles which would travel a short distance (approximately 1 mm) before decaying. Second, it improved the momentum resolution for a track which passes through the fiducial volume of SVX′. The SVX′ provided $r - \phi$ information only. A gas tracking chamber in this region would be inadequate because of the high resolution required to detect secondary vertices, and because of the high track-density environment in the inner radius region.

Silicon was the ionization material chosen for SVX′. Silicon has many properties that make it advantageous as a detection medium [7]. For example, its low ionization energy allows for large signals from incident particles and its low Z means less multiple scattering. The energy required to liberate an electron (create an electron-hole pair) in silicon is only 3.6 eV compared to 20-40 eV for ionizing a gas. Since silicon is a semiconductor, large voltages may be applied to the medium without inducing large DC currents, which would make the signal induced by an incident particle indiscernible. An n-type silicon bulk (doped with valence-5 atoms) was used, with a metal ground plane on one side and the other side etched with strips of p-type silicon (doped with valence-3 atoms). The presence of the p-type strips on the n-type bulk set up a depletion region free of any mobile charge carriers (electrons or holes). The depletion region was enhanced by applying a reverse-bias voltage between the strips and the ground plane on the opposite side of the bulk. This way, a high electric field existed in a region free of mobile charge carriers in a material vulnerable to ionization by an incident charged particle. This situation is exactly analogous to a gas ionization detector, with electron-hole pairs instead of electron-ion pairs. A minimum ionizing particle traversing 300μ of silicon would liberate approximately 22,000 electrons which were quickly (in 10-30 ns) swept to the readout electronics by the electric field in the bulk.

CDF used two different silicon vertex detectors over the course of Run 1 of the Tevatron: SVX in Run 1a, SVX$'$ in Run 1b. SVX needed replacement due to radiation damage (the signal to noise ratio had degraded from 9:1 to 6:1). The SVX$'$ was designed for more durability in the high radiation environment at CDF with the use of a radiation-hard chip and AC-coupled sensors. Since the analysis in this thesis only considers data from Run 1b, we only provide a description of SVX$'$.

SVX$'$ consisted of two barrels, one on each side of the $z = 0$ plane, separated by a 2.15 cm gap. The silicon strip detectors were arranged into four concentric layers of "ladders" composed of 12 wedges, each wedge covering $30°$ in ϕ. The layer at the innermost radius sat 2.36 cm from the beam, and the outermost layer at 7.87

cm. There were two beryllium bulkheads, one for each barrel on the ends of the detector. The ladders were mounted to these bulkheads which provided mechanical support and also housing for tubes used for coolant and gas flow. Each ladder was constructed from three silicon sensors each 8.5 cm long and 300 μm thick. The sensors were AC-coupled with n-type bulk and p^+-type strip implants running parallel to the beam with a 60 μm pitch (55 μm pitch on the outermost layer) on a single side. Aluminum readout strips sat atop the strip implants with a 200μ layer of silicon oxide sandwiched between to form a capacitor. Each ladder was tilted 4.5° in $r-\phi$ to provide overlap between adjacent ladders on the same layer. On each ladder, the three silicon sensors had their strips (channels) wire-bonded end-to-end and then to the readout chips at the large z end of the ladder. The chips were mounted on the ear board, a hybrid circuit on an aluminum-nitride substrate. These hybrids also routed and filtered power, command signals and data to and away from the chips. The readout chip, called SVXH, was a custom-designed, radiation hard, mixed analog-digital ASIC[1] with 1.2μm feature size. The chips had 128 channels and each read out one strip on a sensor. 360 SVXH chips were required to read out the 46080 channels in SVX$'$. To reduce the readout time per event, only those channels with signal above the programmed threshold (and their nearest neighbors) were read out. The length

[1] Application Specific Integrated Circuit

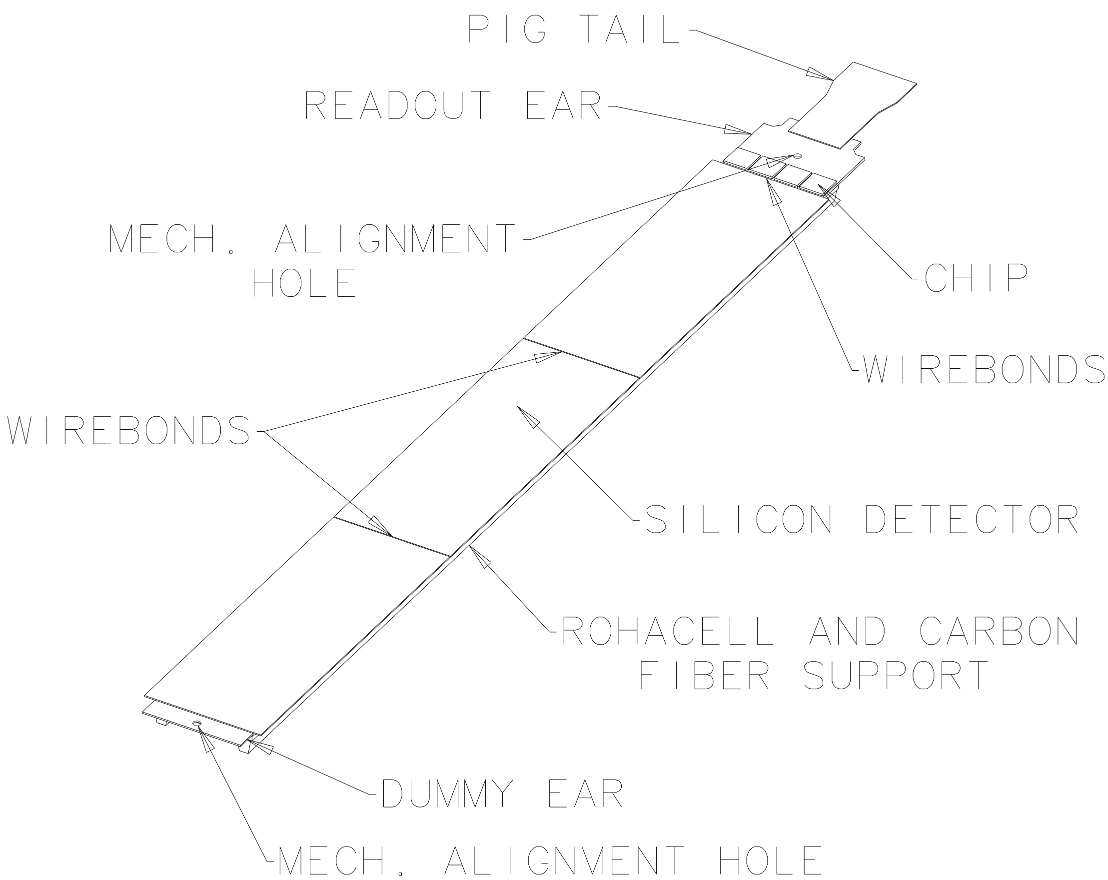

Figure 3.6: *Schematic of a Silicon Vertex Detector ladder. From [27].*

of the active detector region was 51 cm and the interaction region was 30 cm wide, which means that only $\sim 60\%$ of tracks traversed SVX$'$. Figure 3.6 shows a schematic of an SVX$'$ ladder and Figure 3.7 is a drawing of one of the SVX$'$ barrels.

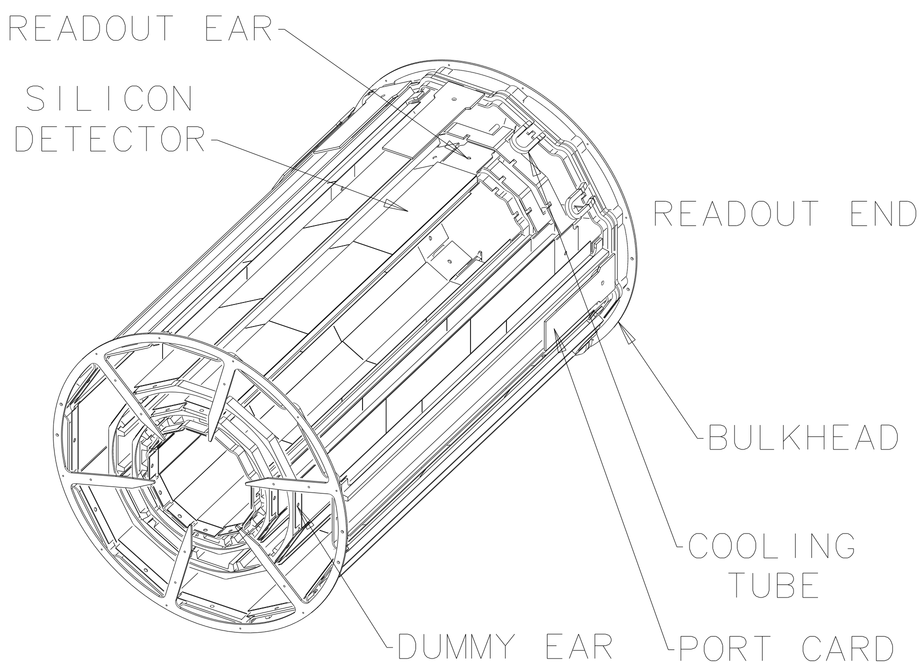

Figure 3.7: *Drawing of one of the Silicon Vertex Detector barrels. From [27].*

Vertex Tracking Chamber

Although the proton/anti-proton collisions occurred at $z = 0$ at CDF, the interactions occurred between partons and were Gaussian distributed around this nominal point with $\sigma \approx 30$ cm. Also, there was often more than one interaction between partons per crossing due the high luminosity at the Tevatron. The time-projection-chamber (TPC) was designed to determine the position of these interactions along the z direction by measuring the $r - z$ projection of the track trajectories.

The VTX consisted of 28 octagonally shaped TPC modules, each 9.8 cm in length (see Figure 3.8). Each module was rotated by $11°$ in ϕ relative to its neighbors. An aluminum high voltage grid, serving as a cathode plane, divided each module into two drift regions in z. Sense wires were situated close to the cathode and ran along the azimuthal direction. Incident particles ionized the 50% argon, 50% ethane gas mixture which filled the modules and the liberated electrons drifted to the sense wires. Their arrival time served as a measure of the z position of the incident particle at the wire radius. Modules in the region $|z| < 85$ cm had 16 sense wires between $r = 11.5$ cm and $r = 21.0$ cm while modules in the region $85 < |z| < 132$ cm had 24 sense wires from $r = 6.5$ cm and $r = 21.0$ cm. The VTX determined the position of a primary vertex to a resolution of 2 mm.

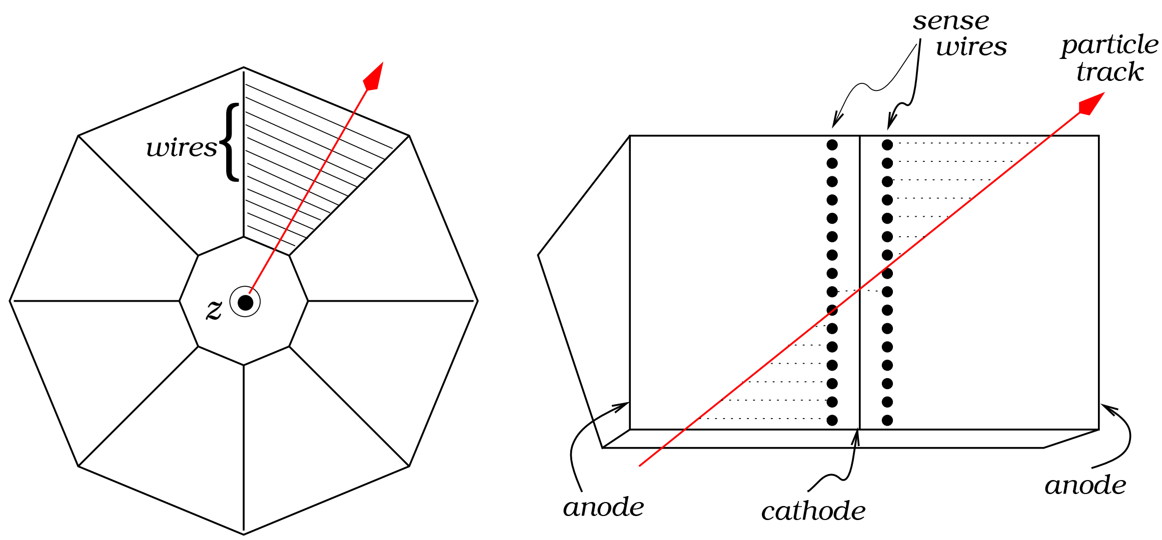

Figure 3.8: *Cartoon of the Vertex Tracking Chamber. From [27].*

Central Tracking Chamber

The central tracking chamber (CTC) [21] was the main thrust of the tracking system at CDF. It was a cylindrical drift chamber 3.2 m along its axis in the z direction, with its inner (outer) radius at 0.3 (1.3) m. A drift chamber measured ionization that occurred when charged particles traversed a volume of gas. As electrons were liberated in the gas, they drifted to anode sense wires in an electric field. With a known drift velocity for the electrons in the gas, the trajectories of the incident particles were measured with a position resolution better than the spacing between sense wires.

In the CTC the sense wires were arranged into 84 layers divided into 9 "super-layers." Within each super-layer, a drift cell consisted of a set of 40 μm gold-plated tungsten sense wires surrounded by a row of high voltage field wires on each side to set up an electric field 1350 V/cm in strength and uniform to within 1.5%. Five of the super-layers (axial) contained cells with 12 sense wires that ran parallel to the beam and provided measurements in $r - \phi$. The remaining four super-layers (stereo) sat between the axial layers in radius, contained 6 sense wires per cell, and were rotated in the $r - z$ projection by 2.5% with respect to the beam to provide measurements in $r - z$. The chamber was filled with a gas mixture of 49.6% Argon, 49.6% Ethane, and 0.8% Ethanol. The maximum drift time for liberated electrons in the gas was 800 ns compared to the 3.5 μs bunch spacing.

Within each super-layer, the cells were tilted by 45% in the $r - \phi$ projection to compensate for the azimuthal angle subtended by the drift electrons in the crossed electric and magnetic fields. This tilt in the drift cells also meant that a full range in drift times was always seen within a given super-layer for a high p_T track, which was advantageous for measuring the drift velocity. Also, the existence of at least one hit in each super-layer with a short (< 80 ns) drift time was utilized in the level 2 track trigger (see Section 3.2.5). Figure 3.9 shows the CTC end-plate as viewed in the $r - \phi$ projection. The transverse momentum resolution of the CTC was

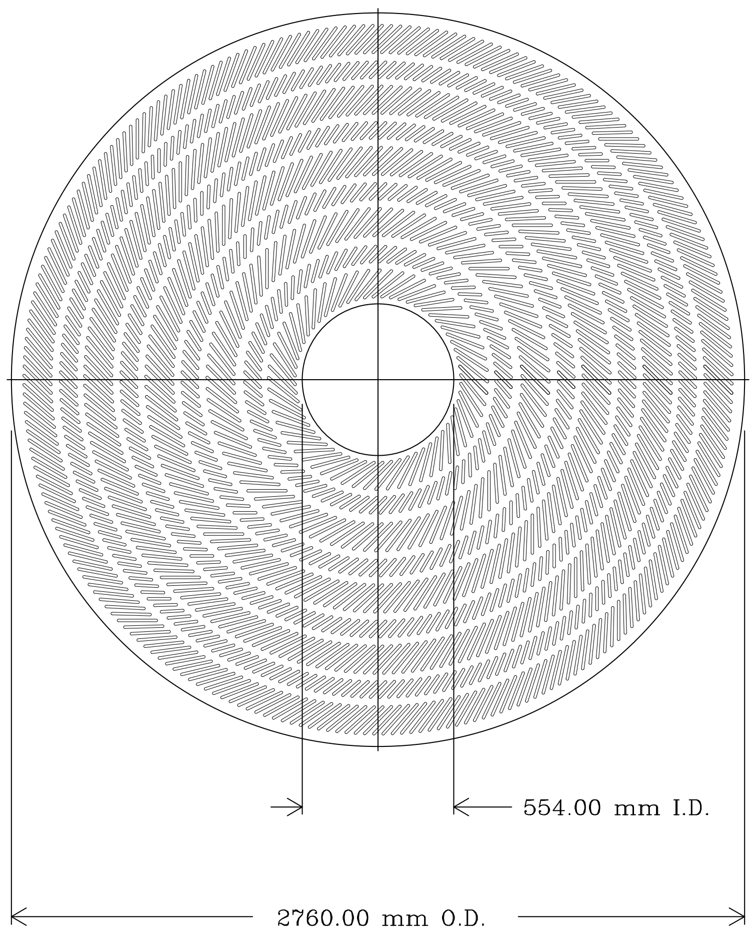

Figure 3.9: *The CTC end-plate as viewed in the $r - \phi$ projection. From [27].*

$$\delta p_T/p_T = 0.002 \text{ GeV}^{-1} \times p_T \tag{3.10}$$

By combining CTC and SVX′ tracking information when information from both sub-detectors was available, the resolution was improved. The transverse momentum resolution of CTC and SVX′ combined was

$$\delta p_T/p_T = 0.001 \text{ GeV}^{-1} \times p_T \tag{3.11}$$

The resolution on the impact parameter (d_0) of the track with respect to the beam was $\sigma_{d_0} = 0.07$ cm. The resolution on the z position of the track was measured in the CTC is 1.0 cm.

dE/dx

The CDF tracking system was also used for particle identification. The tracking system detected the ionization of charged particles as they traversed a material, and the ionization energy per unit length left by a particle depended on the velocity of that particle through the Bethe-Bloch formula [7]:

$$-\frac{dE}{dx} = Kz^2\frac{Z}{A}\frac{1}{\beta^2}\left[\frac{1}{2}\ln\frac{2m_e c^2\beta^2\gamma^2 T_{up}}{I^2} - \beta^2 - \frac{\delta}{2}\right] \tag{3.12}$$

where β is the velocity of the incident particle relative to the speed of light in a vacuum (c), $\gamma = 1/\sqrt{1-\beta^2}$, z is the charge of the incident particle relative to the electron charge, $K = 0.307075$ MeV g^{-1} cm^2, A is the atomic mass of the medium, m_e is the electron mass, I is the ionization energy of the material, $T_{up} = \max(T_{max}, T_{cut})$ where T_{max} is the maximum kinetic energy which could be imparted to a liberated electron in a single collision and T_{cut} is the maximum energy imparted to an electron in a tracking cell before the electron would escape the drift cell. Finally, δ is the correction due to the density effect, discussed below. Through a measurement of their ionization and momentum in the tracking system, particles with differing mass might have been resolved, since heavier particles would have a slower velocity for a given momentum.

Figure 3.10 shows the measured dE/dx from tracks in the CTC and in the SVX$'$ plotted against β and compared to the predictions. For this plot, control samples with known particle types were used so that the particle velocity could be deduced from the track momenta. In the CTC, the ionization energy was proportional to the pulse width on the sense wires[2]and was measured in nanoseconds. In the SVX$'$, dE/dx was by measured from the collected charge on the four silicon layers. Each curve falls like $1/\beta^2$ at low velocity but their shapes differ at high β. In the CTC, we saw a $\ln \beta^2\gamma^2$ dependence and this part of the curve is called the logarithmic rise. This is because an energetic particle emits a flattened and extended electric field causing interactions

[2]Pulse widths were only measured in the outer six super-layers of the CTC.

to occur from longer distances in the material. In the SVX$'$, we saw a suppressed logarithmic rise and there were two reasons for this. The first reason was a reduced T_{cut} in silicon compared to the gas in the CTC (electrons with $E \gtrsim 500$ keV escape detection in silicon). The second reason is named the density effect and it comes into play when the material becomes polarized as a result of the electric field emitted by the incident particle, truncating the logarithmic rise.

While the logarithmic rise in the CTC was valuable for identifying known particles at CDF, the lack of logarithmic rise in the SVX$'$ was advantageous in a recent search for new charged particles at high mass at CDF [29]. The analysis sought large ionization left by a massive charged particle with low velocity (in the region of the $1/\beta^2$ dependence). Ionization from both the CTC and the SVX$'$ were considered, with greater power to distinguish signal from background in the SVX$'$ due to the suppressed logarithmic rise resulting in reduce contamination in the region of large ionization. Also, the masses of the particles leaving candidate tracks were deduced from their measured ionization in the SVX$'$ and from their momenta. The search set limits on the cross-section for the production of a stable color-triplet quark with masses $M \gtrsim 190$ GeV for $q = \frac{1}{3}$ and $M \gtrsim 220$ GeV for $q = \frac{2}{3}$. Also, the cross section for Drell-Yan production of long-lived scalar taus was limited to $\lesssim 1$ pb, which is over an order of magnitude higher than the model prediction. Considering a benchmark

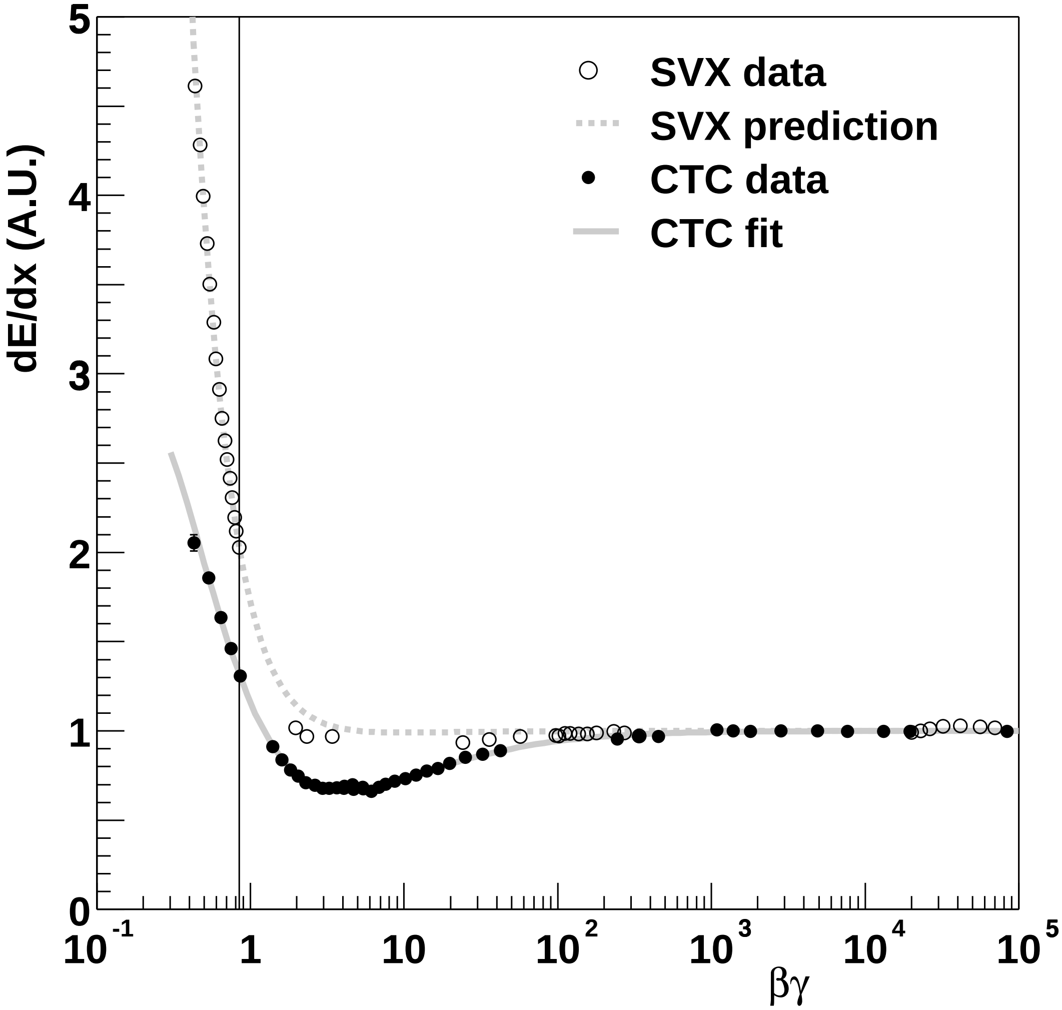

Figure 3.10: *dE/dx curves as measured in the CTC and in SVX′'. From [29].*

model where scalar leptons arise from cascade decays of heavy particles improved the sensitivity, resulting in an upper limit at 550 fb compared to a predicted 80 fb.

Detector Material

When designing a tracking system, it is important to use materials which will have a low impact on the momentum and energy of the particles that one would like to measure. Particles will lose energy and be deflected through the processes of ionization, radiation and multiple coulomb scattering. The impact of these electromagnetic processes increases by the number of radiation lengths traversed by a particle in the detector.

The following equation gives an approximation to the radiation length of a material, good to a few percent [7]:

$$X_0 = \frac{716.4\text{g cm}^{-2} A}{Z(Z+1)\ln(287/\sqrt{Z})} \tag{3.13}$$

Notice that a radiation length is expressed in g/cm^2, so that one needs to divide by the density to get a radiation length expressed in centimeters. Therefore, using materials with low Z whenever possible minimizes the number of radiation lengths a particle will traverse in tracking volume. For example, beryllium ($Z = 4$) was used to construct the beam-pipe which surrounded the beam as it passed through CDF. In the CDF Run 1 detector, a particle traversing the entire tracking system passed through less than 5.5% X_0, with 3.5% X_0 from the SVX$'$ alone.

For the Run 2 upgrade of CDF, a new silicon detector was constructed, and this time readout electronics were glued onto the silicon sensors themselves in the active detector volume[3]. Estimates were made of the contribution of this added material to the total material in the tracking volume in Run 2 at CDF. We summarize the results of those estimates here.

A hybrid consists of thick film circuitry printed on a beryllium substrate. It is this part that is glued to the silicon sensors in Run 2. Silicon chips[4]are attached to the hybrids with silver epoxy and wire bonds electrically connect the channels on the sensors to the chips. External components (resistors and capacitors) necessary for the function of the chip are soldered to the hybrids. Kapton cables carry signals from the hybrids to the next stage of readout, which is the transceiver chip on the portcard (a larger type of hybrid with circuitry printed on both sides of the substrate). Figure 3.11 illustrates how these various components are assembled together.

The material contributed by hybrids, portcards, cables are cable connectors were estimated as an average over each part, i.e., as if each component of the part were smeared over the entire surface. The composition of each component was deduced

[3]This choice was made in an effort to keep the lengths of the silicon channels as short as possible for a longer lifetime of the detector in a high radiation environment.

[4]These chips contain the circuitry necessary for fast readout of the detector and for storing data while trigger decisions are made.

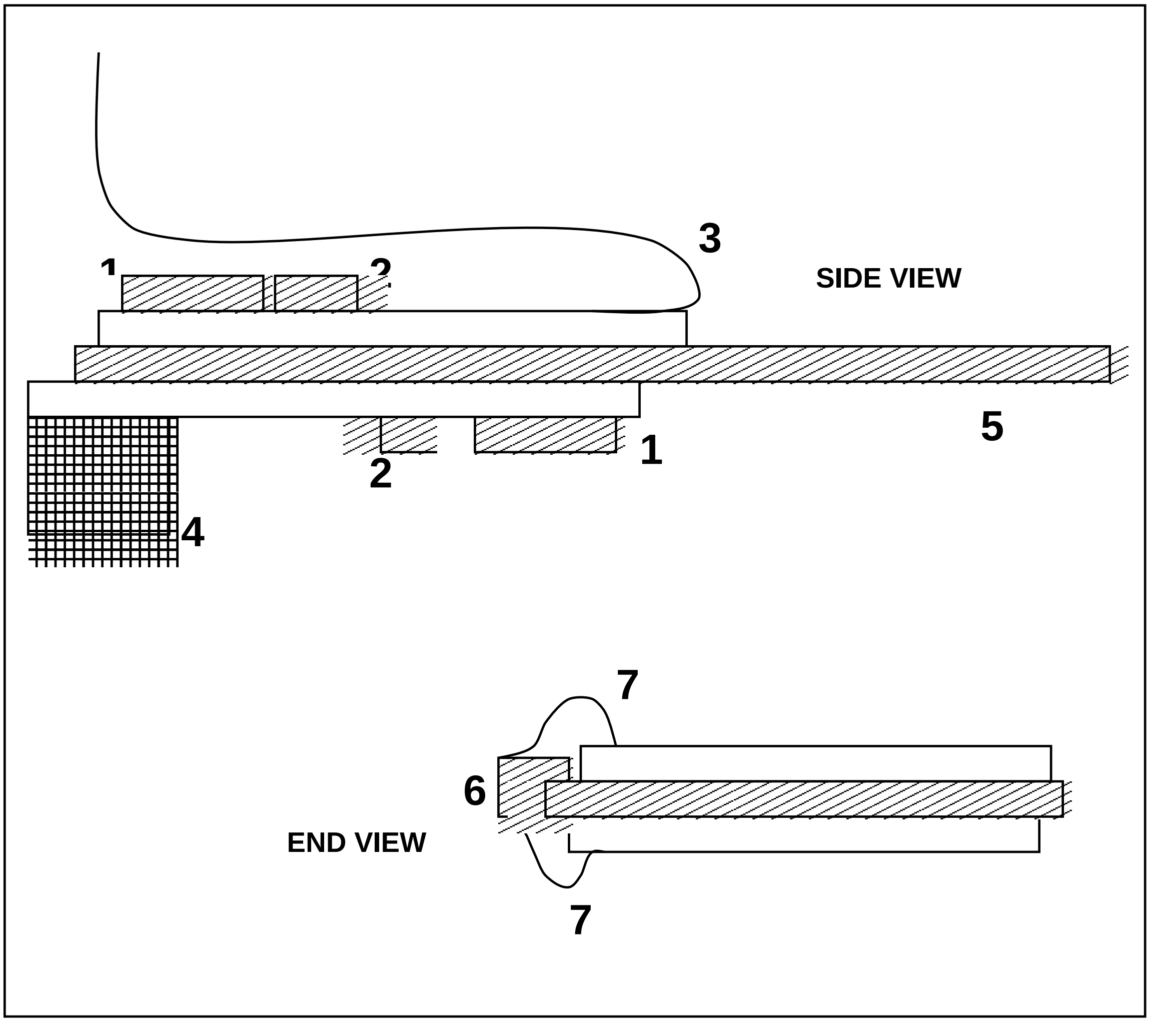

Figure 3.11: *This figure shows the side and end views of a readout unit, or the one of the two sensors in a half-ladder where the electronics are mounted. The components are labeled as follows: 1 (2): the front-end (back-end) chips (actually, the front-end and back-end chips were merged into one chip since this figure was drawn), 3: the readout cable, 4: the bulkhead, 5: the sensor, 6: jumper, 7: jumper wire-bonds. The open shapes are hybrids. From [30].*

from manufacturing specifications and by weighing and measuring the dimensions of the parts.

The effective radiation length of a mixture or compound is given by [7]:

$$1/X_0 = \sum w_j/X_j \tag{3.14}$$

where w_j and X_j are the weight and radiation length of each element in the compound. This equation was also used to find the effective radiation length of a part with many components.

For the hybrids and portcards, the largest contribution to their material is the printed circuitry. A typical radiation length of a hybrid is 20-22 g/cm^2 or 6-7 cm, including surface mounted components. From the thickness of the parts, the percentage of a radiation length that each hybrid contributes is typically 1.3%-1.6%. The cables connecting the hybrids to the portcard each contribute approximately 0.3% of a radiation length, including connectors for attachment. This means that a particle incident all four layers of SVX$'$ electronics would traverse approximately 15% of a radiation length of material. A track traversing a portcard, its cable or connectors will be see closer to 20% X_0. A particle which only traverses silicon sensors will see approximately 5% X_0 [31].

An additional layer of silicon called L$\emptyset\emptyset$ sits on the CDF beampipe in Run 2. A track will traverse typically 0.5-2.5% X_0 depending on whether it traverses a single sensor or two sensors in an overlap region, and whether it passes through the walls of the support structure.

Intermediate Silicon Layers (ISL) sitting beyond the SVXII in radius add additional material in the range of 0.5% to $\gtrsim$ 3% depending on whether a track passes through one or two layers of silicon and whether is passes through the ISL readout hybrids.

Figure 3.12 shows the estimates of the material in the tracking at CDF in Run 2 compared to the amount of material measured from events containing a photon that converted to an electron pair in the material. In the figure, the simulated curve is scaled to the data at the COT inner cylinder, near 42 cm. The plot shows fair agreement between data and simulation in the region of the SVXII detector ($\lesssim$ 11 cm). The peaks near 20 cm, 23 cm and 29 cm are due the ISL silicon layers along with their associated support structures and cabling. The high peak in the region near 15 cm is due to SVX II portcards and cables that sit between SVX II and ISL. The simulated curve shown is known to not adequately account for cable bundles in the region near 15 cm. Improving the simulation of the detector material continues to be work in progress.

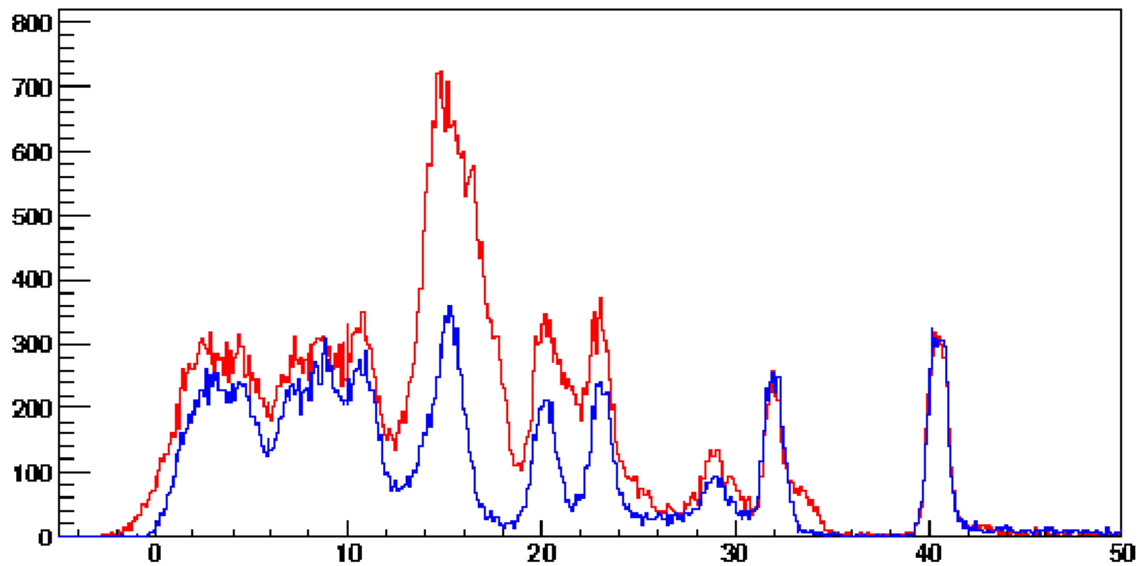

Figure 3.12: *Estimated material in the CDF Run 2 detector compared to the amount of material measured from conversions[32].*

3.2.3 Muon Systems

The muon detectors at CDF were drift chambers which sat behind the calorimetry in radius. A muon has a low probability to bremsstrahlung in the calorimetry due to its large mass compared to the electron. A muon does not interact through the strong force, so it also will not produce a hadronic shower. Thus, any charged particle which penetrated the calorimeters is expected to have been a muon.

Three separate detectors made up the CDF central muon system: the Central Muon Chambers (CMU) [22], the Central Muon Upgrade (CMP) and the Central Muon Extension (CMX) [23]. The latter two were added in 1992. Figure 3.13 shows the $\eta - \phi$ coverage of the central muon system.

Central Muon Chambers

The CMU sat radially behind the CHA at $r = 3.47$ m in the region $|\eta| < 0.6$. It was separated into twelve $12.6°$ wedges in ϕ with $2.4°$ gaps between modules, leaving only 85% coverage in ϕ. Each module consisted of three modules, each with four layers of four rectangular drift cells. The ionizing gas in the CMU was 49.6% argon, 49.6% ethane, and 0.8% ethanol. The sense wires running parallel to the beam at the center of each cell were 50 μm steel. The sense wires were held at 3150 V. The drift time was at most ~700 ns. To remove ambiguity in ϕ, sense wires were offset by 2 mm relative to those in neighboring layers. The drift time was used to determine the position of the track in ϕ, while charge separation determined the track position in z. The position resolution of the CMU was 250 μm in ϕ and 1.2 mm in z. Figure 3.14 illustrates a track left by a charged particle incident on a module in the CMU.

Central Muon Upgrade

An energetic hadron which did not lose all of its energy in the hadronic calorimeter (a "punch-through") would have faked a muon in the CMU. To reduce the rate for punch-throughs, the CMP was added behind the CMU in 1992, consisting of

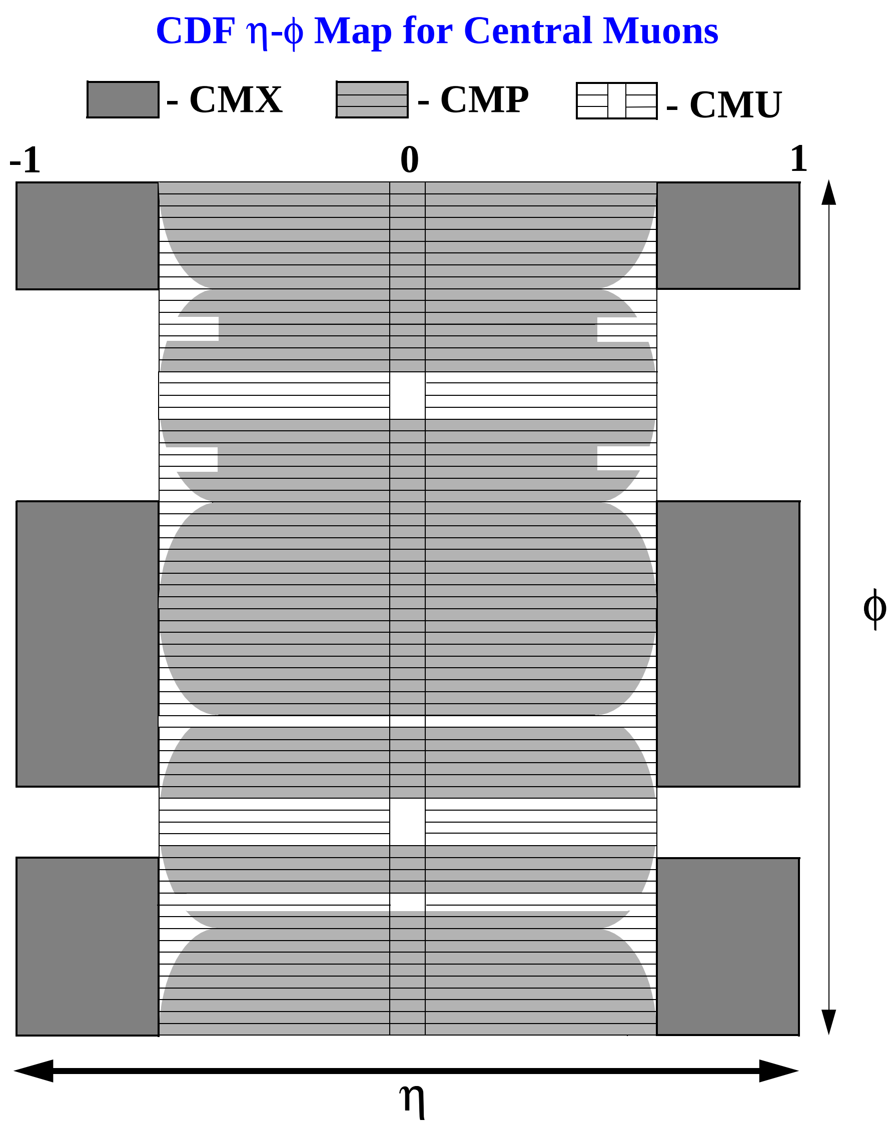

Figure 3.13: *Schematic showing central muon coverage. From [27].*

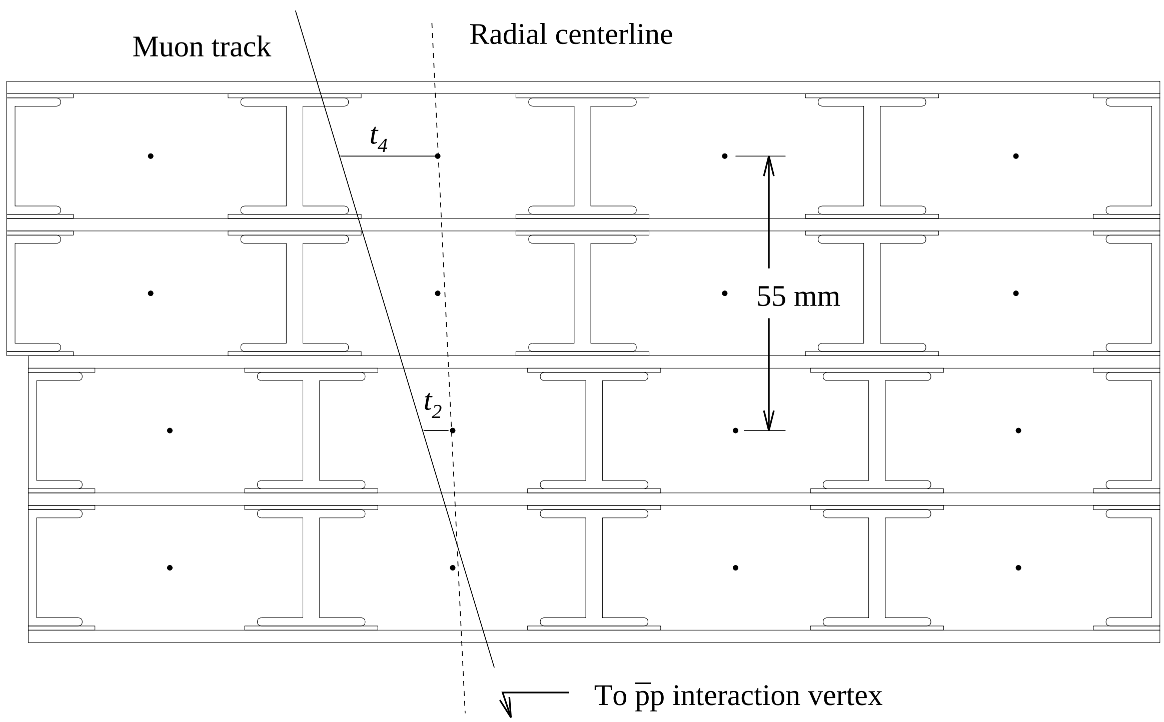

Figure 3.14: *Illustration of a track passing through four muon chambers. Note the sense wires are offset to remove ambiguity in ϕ. From [27].*

an additional 0.6 m of steel (2.4 interaction lengths) and four more layers of drift chambers. The CMP provided $r - \phi$ measurements only. The CMP also detected muons which fell in the gaps in ϕ in the CMU. At the inner and outer surfaces of the CMP were scintillator planes, which were used to provide timing information used in the trigger system.

Central Muon Extension

At the same time that the CMP was added, the CMX was added to extend the coverage for muon detection to the region $0.6 < |\eta| < 1.0$. The CMX consisted of four arches of drift tubes sitting about 6.2 interaction lengths deep in the detector. The CMX covered 71% of the solid angle in the region $0.6 < |\eta| < 1.0$. Just as for the CMP, at the inner and outer surfaces of the CMX were scintillator planes for timing information.

3.2.4 Luminosity Counters

The Beam-Beam Counters (BBC) [24] monitored the instantaneous luminosity delivered to CDF by the Tevatron. The BBC consisted of scintillators mounted in front of the forward calorimeters at $|z| = \pm 5.8$ m, covering the region $3.2 < |\eta| < 5.9$. The timing resolution of the BBC was 200 ps. The BBC counted coincident hits in the forward and backward scintillators as a measure of the instantaneous luminosity. The total luminosity is the instantaneous luminosity integrated over time. After considering only runs where all detector subsystems were working properly, the Run 1b data sample included 86.5 ± 3.5 pb^{-1} of data.

3.2.5 Data Acquisition

The Run 1 Tevatron delivered $p\bar{p}$ collisions every 3.5 μs with more than one event per crossing on average. Therefore, the event rate at CDF was ~280 kHz. However, CDF was only capable of transferring data to tape at a rate of < 10 Hz. A three-level trigger system was used to select interesting events for data storage. At each subsequent trigger level, events were received for consideration at a slower rate as the selection requirements became more sophisticated. Each trigger only considered events which pass a trigger at preceding level. Level 1 (L1) and level 2 (L2) triggers were implemented through hardware while level 3 (L3) is implemented through software.

Level 1 Trigger

The L1 trigger [25] used information from the calorimetry and muon chambers only. HAD and EM calorimeter towers were considered only in units of "trigger towers" which covered 0.2 units of η and 15° in ϕ. A calorimeter trigger at L1 made decisions based some energy threshold on the trigger towers. Muon triggers at L1 required that at least two hits were detected in a muon chamber. At L1 there was no dead time since the time required for a trigger decision was less than the time between bunch crossings. At L1, events were accepted and sent to L2 for consideration typically at a rate of 1 kHz.

Level 2 Trigger

The L2 trigger considered information from the calorimeter, muon systems and also the central fast tracker (CFT). The CFT provided preliminary measurements of the track momenta using only $r - \phi$ information from the axial super-layers of the CTC. The CFT measured transverse momenta with a resolution of $\delta p_T/p_T^2 = 3.5\%$. Also at L2, calorimeter clusters were formed, jets, electron and photon candidates were identified, and kinematic variables and missing transverse energy was calculated. A trigger decision was made based on whether or not one of these objects or some combination of them was found in the event. This L2 decision took approximately 40 μs. Any event which passed the L1 trigger during this time was ignored. This resulted in approximately 3% of bunch crossings being missed at L2. L2 typically accepted events at a rate of 20-35 Hz.

Level 3 Trigger

For each event that passed the L2 trigger, the full detector was read out, which took approximately 3 ms, causing about 5% dead time to be incurred at L3 [26]. Once the data had been formatted into event records ~100 kilobytes in size, it was passed to the L3 trigger, which was a farm of Silicon Graphics processors running `FORTRAN-77` reconstruction and filter algorithms. The L3 trigger accepted events at a rate of about 8 Hz in Run 1b. All events passing the L3 trigger were written to 8 mm tape for further processing.

Offline Reconstruction

Once the data had been written to tape, the events were fully reconstructed with the offline software. When the offline reconstruction was performed, there was more time available compared to when the L3 decision were made, allowing a more thorough reconstruction of each detector component. Also, calibrations which were not available at L3 were included in the offline reconstruction. The offline software recorded the raw data for the event as well as the reconstructed physics objects (jets, electrons, muons and so on) onto 8 mm tape.

Chapter 4

Data Selection

4.1 Strategy

In Chapter 2 we have outlined our intent to search for Supersymmetric Higgs bosons through the process $gg \to A/h \to \tau^+\tau^-$ and in Chapter 3 we have described the machine which provides the $p\bar{p}$ collisions and the apparatus used to detect the debris from those collisions. In this chapter, we describe the requirements made on the data to search for $A/h \to \tau^+\tau^-$ events among the debris in the Run 1b data sample. These requirements are the result of an optimization procedure (described in Chapter 7) that maximized the sensitivity of the search to the events of interest.

The lifetime of a tau at rest is 290.6 ± 1.1 fs [7], so we do not observe taus directly but instead we observe their decay products. A tau may decay to leptons or hadrons. Table 4.1 shows the branching ratios for the dominant tau decay modes. Notice that $85.35 \pm 0.07\%$ of the tau decays are "one-prong" (the decay products include only one charged particle) including 49.5% one-prong hadronic decays. Three-prong decays occur $15.20 \pm 0.07\%$ of the time. Notice that one-prong hadronic decays contain a neutral pion nearly half the time but rarely contain more than two. Three-prong decays contain one neutral pion at most. The advantage to searching for taus that decay leptonically is that their signature is distinct from the QCD backgrounds which are prevalent at CDF. However, hadronic decays claim larger branching ratios, so if one is able to separate them from QCD jets, then there is much to be gained in the

Decay Type	Decay Mode	Branching Ratio (%)
Leptonic (35.2%)	e $\nu_e \nu_\tau$	17.84 ± 0.06
	$\mu\ \nu_\mu \nu_\tau$	17.37 ± 0.06
Hadronic (64.8%)	$\pi + 0\pi^0 + \nu_\tau$	11.06 ± 0.11
	$K + 0\pi^0 + \nu_\tau$	0.686 ± 0.013
	$\pi + 1\pi^0 + \nu_\tau$	25.41 ± 0.14
	$\pi + 1K^0 + \nu_\tau$	0.89 ± 0.04
	$\pi + 2\pi^0 + \nu_\tau$	9.23 ± 0.14
	$\pi + 3\pi^0 + \nu_\tau$	1.08 ± 0.10
	$3\pi + 0\pi^0 + \nu_\tau$	9.52 ± 0.10
	$3\pi + 1\pi^0 + \nu_\tau$	4.37 ± 0.10

Table 4.1: *Here we list the dominant tau decay modes (where the central value of the experimentally measured branching ratio is at least 0.5%) [7].* π *and* K *denote* charged *pions and kaons and* ν_τ *denotes the tau neutrino (tau anti-neutrino) for a decaying* τ^- (τ^+).

expected rate of detection. In the analysis presented in this thesis, we search for events where one tau decays to an electron and two neutrinos ($\tau \rightarrow e\nu_e\nu_\tau$) and the other tau decays to hadrons. We name the former τ_l and the latter τ_h.

The backgrounds for this analysis may be divided into two categories: physics-dominated and detector-dominated. The former includes $Z/\gamma^* \rightarrow \tau\tau$ and $Z/\gamma^* \rightarrow e^+e^-$ and the latter included any event where a QCD jet fakes a lepton (W+jets or QCD events). We model signal and physics-dominated backgrounds by generating events with Pythia 6.203 [33] Monte-Carlo (MC) and model the detector response with a parameterized detector simulation called QFL.

As each selection requirement is described, we assess how well Pythia+QFL models the efficiency of that cut by comparing Pythia+QFL with Z control samples. Where the simulation does not describe the data, a scale factor or a systematic error is imposed or agreement is forced by weighting the events or by using the Acceptance Rejection Monte-Carlo Technique (ARMCT)[1]. Except where otherwise noted, we apply the identical scale factors and systematics to $A/h \rightarrow \tau\tau$ as $Z \rightarrow \tau\tau$ efficiencies.

We have selected the following samples for comparisons between data and Pythia+QFL. First, $Z \rightarrow e^+e^-$ and $Z \rightarrow \mu^+\mu^-$ data control samples. Next, $Z \rightarrow e^+e^-$, $Z \rightarrow \mu^+\mu^-$ and $Z \rightarrow \tau^+\tau^-$ Pythia+QFL samples. All $Z \rightarrow e^+e^-$ and $Z \rightarrow \mu^+\mu^-$ samples are

[1] By this method, we decide to accept or reject each event based on the probability the event would pass.

divided into Tight and Loose samples, the latter for electron identification studies. The selection of all data and Pythia+QFL samples used in this study is described in Appendix B.

4.2 Central Electron Trigger

The search begins with a data sample triggered by a high-E_T ($>$ 18 GeV at L3) electron candidate. Unfortunately, this trigger is less than ideal for this analysis since electrons from the tau decays of interest are typically closer to $E_T \sim 10$ GeV. $A/h \rightarrow \tau\tau$ events with one tau decaying to an electron are expected to pass this trigger only about 20% of the time. A trigger with a lower E_T threshold would give a sample with a higher rate of fake backgrounds. As discussed in Appendix D, in Run 2 at CDF, new triggers more suited for di-tau analyses have been implemented with a lower E_T threshold on a lepton candidate but also requiring a second stiff track in the event. There was no such trigger available in Run 1 at CDF.

QFL does not model trigger inefficiencies, so it is necessary implement our own trigger simulation based on the measured efficiencies for the trigger used. We describe this trigger simulation in what follows.

4.2.1 Level 1

The L1 calorimeter trigger requires one trigger tower[2]with $E_T > 8$ GeV in the CEM. The L1 electron efficiency was measured from muon-triggered events. Events with a central electron passing stiff electron identification cuts (similar to those described in Sections 4.3.2- 4.3.9) and that pass the L2 inclusive electron trigger are considered. From these events, the probability that the event passed the L1 calorimetry trigger was measured to be 100%, with an uncertainty at the level of 10^{-3}.

4.2.2 Level 2

At L2, the high-E_T inclusive electron trigger requires one calorimeter cluster with $E_T > 16$ GeV and the ratio of electromagnetic energy to hadronic energy (E_{HAD}/E_{EM}) less than 0.125. This cluster must be close in azimuthal angle to a CFT track with $p_T > 12$ GeV.

Since the L2 trigger requirement contains two parts ($E_{EM} > 16$ GeV, $p_T > 12$ GeV), the L2 trigger efficiency is measured in two steps [46]. This efficiency is measured per electron, not per event. First, the E_T dependence of the efficiency is measured by considering events which pass a trigger with lower thresholds ($E_{EM} > 8$ GeV, $p_T > 7.5$ GeV) and counting which pass the high E_T trigger in bins of E_T. This

[2]Remember that at L1, a calorimeter towers are paired in η to form trigger towers.

Parameter	Best Fit Value
ϵ	0.99809 ± 0.00095
E_0	16.769 ± 0.096
σ_E	1.0271 ± 0.0368
P_0	15.701 ± 0.483
σ_P	3.3478 ± 0.3837

Table 4.2: *Best fit values of the parameters in the functional form given in the text describing the E_T dependence of the L2 trigger efficiency. From [46].*

relative efficiency is fit to the following form as a function of E_T:

$$\epsilon(E_T) = \epsilon_0 \cdot Freq((E_T - E_0)/\sigma_E) \cdot Freq((E_T - E_0)/\sigma_P) \tag{4.1}$$

where

$$Freq(x) = \frac{1}{\sqrt{2\pi}} \int_{-\infty}^{x} \exp -\frac{1}{2}t^2 dt \tag{4.2}$$

The best fit parameters are summarized in Table 4.2 and the function is shown graphically in Figure 4.1.

Next, the η_d dependence of the trigger efficiency is measured for asymptotically high E_T. A pure $W \to e\nu$ sample is selected from a L2 trigger requiring $\not{E}_T > 20$ GeV and $E_{EM} > 16$ GeV. Offline, the electron is required to pass $E_T > 25$ GeV.

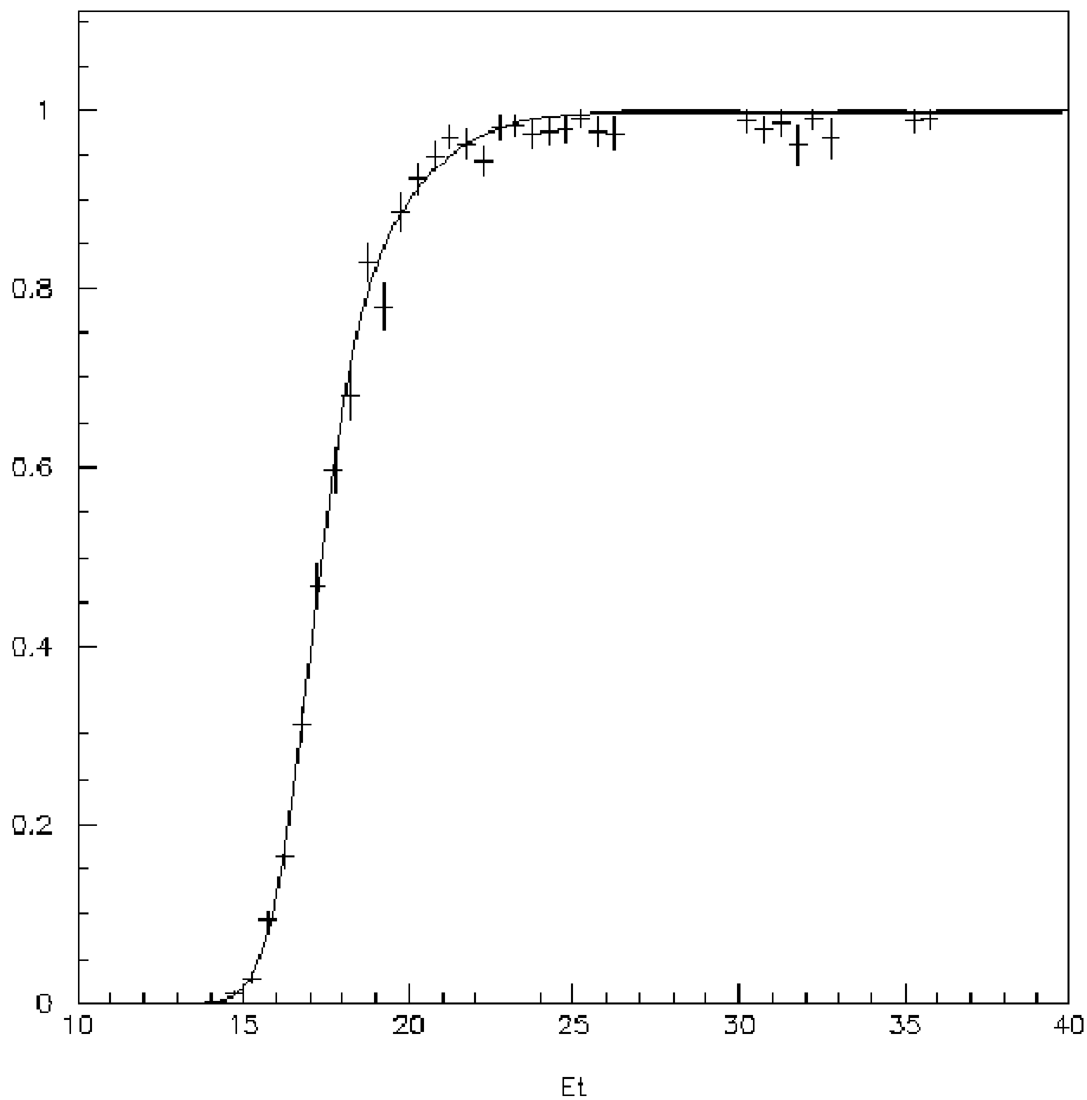

Figure 4.1: *L2 trigger efficiency measured against electron candidate E_T. From [46].*

Parameter	Best Fit Value
P_0	0.87346 $\pm$ 0.00286
P_1	-0.0035985 $\pm$ 0.0052895
P_2	0.26630 $\pm$ 0.01605
P_3	0.010393 $\pm$ 0.008467
P_4	-0.18473 $\pm$ 0.01850

Table 4.3: *Parameters of the fourth order polynomial which best fit the measured L2 efficiency vs. η_d distribution, for electrons which have $E_T > 25$ GeV. From [46].*

The rate at which the electron candidates in the sample pass the high E_T electron trigger binned in η_d is shown in Figure 4.2. This η_d dependence satisfies a fourth-order polynomial with the parameters listed in Table 4.3.

To simulate the L2 trigger, a MC event is weighted according to the probability that any electron in the event fired the L2 trigger, given the η_d and E_T of each electron in the event. So for a given event, the weight W is given by

$$W = 1 - \prod_{i=1,N} 1 - \epsilon(E_{Ti}, \eta_{d\,i}) \tag{4.3}$$

where $\epsilon(E_{Ti}, \eta_i)$ is the probability that an electron with detector pseudo-rapidity $(\eta_{d\,i})$ and transverse energy E_{Ti} fires the L2 trigger. N is the number of electron candidates in the event. To measure the overall efficiency of the L1 trigger, events we selected

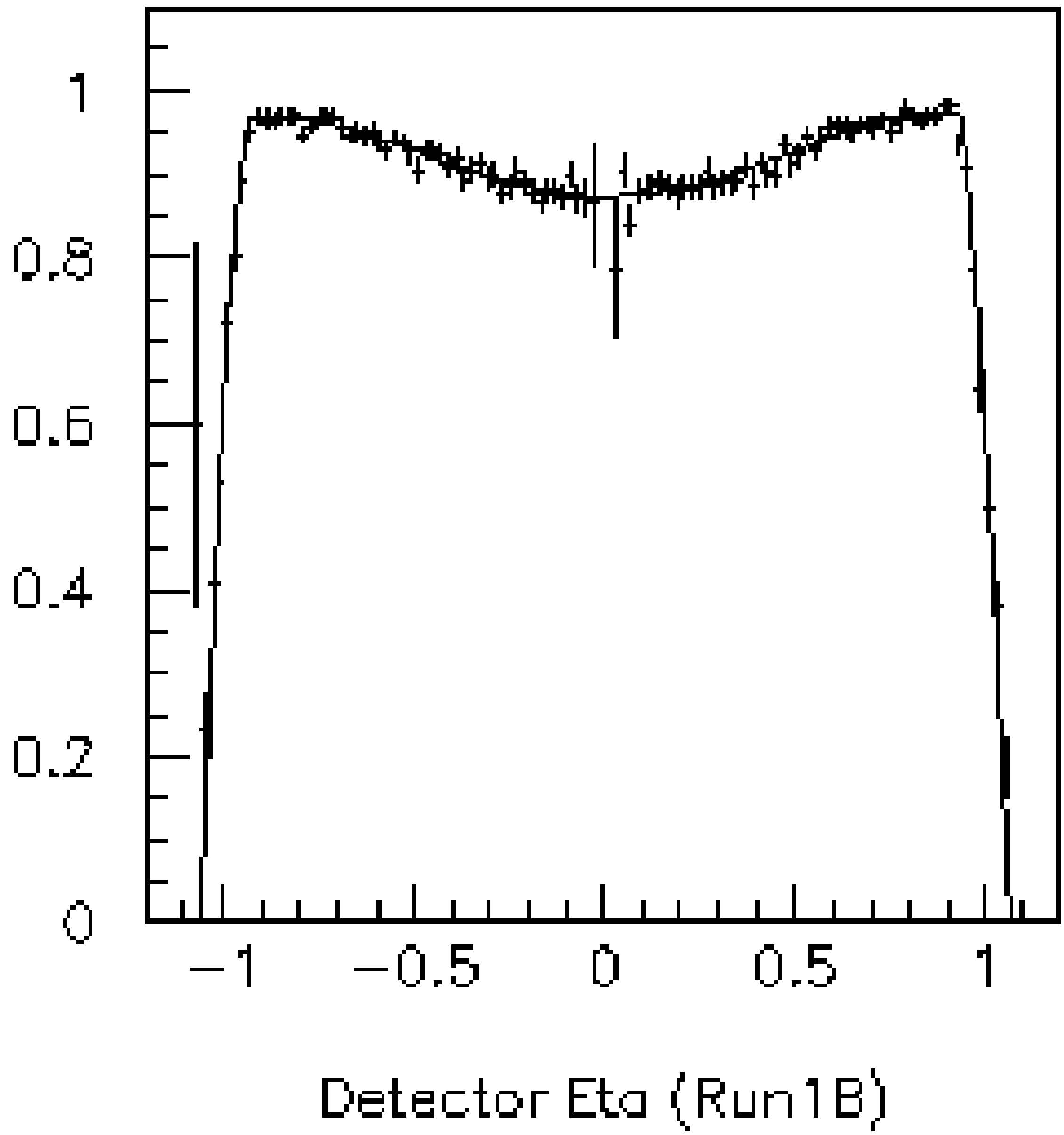

Figure 4.2: *L2 trigger efficiency measured against η_d. From [46].*

where one electron passes stiff electron identification requirements . Of these, 91% pass this L2 high-E_T electron trigger.

The systematic error for a simulated process due to the modeling of the trigger efficiency is obtained by moving the parameters in Table 4.3 by 1σ in each direction (such that they all move the efficiency in the same direction) and measuring the effect on the total efficiency of all cuts. This systematic is approximately 2%.

4.2.3 Level 3

At L3, the inclusive electron trigger requires a calorimeter cluster with $E_T > 18$ GeV and $E_{HAD}/E_{EM} < 0.125$ and an associated track with $p_T > 13$ GeV. Additional electron identification requirements are also made on the electron candidate, including $Lshr < 0.2$, $\chi^2 < 10$, $|\Delta x| < 3$ cm and $|\Delta z| < 5$ cm (these variables will be defined in Section 4.3.1).

4.2.4 Offline Sample Selection

Offline, further cuts (listed in Table 4.4) [3]are made on the candidate electron Then, the search begins with an inclusive electron sample containing 128,730 events.

[3]All of the electron variables shown in the table are defined in Sections 4.3.2- 4.3.9. The only exception is $Lshr_2$. The $Lshr$ variable defined in Section 4.3.3 is based on 3 towers, whereas here we also cut on $Lshr_2$, based on two towers.

4.3 Electron Identification

In this section, we describe the electron identification requirements made on the inclusive electron sample at the analysis level. As each cut is introduced, we check that the variable is well modeled in the QFL simulation by comparing $Z \rightarrow ee$ data and MC samples. In Figures 4.3 and 4.4 we show the comparison between data and simulation for each variable. The $Z \rightarrow ee$ samples used are described in Appendix B.

The $Z \rightarrow ee$ samples are named the Tight and Loose $Z \rightarrow ee$ Data and MC Samples. The Tight samples have stringent electron identification requirement made on both electron candidates and the Loose samples have stringent cuts applied to one candidate and loose cuts on the other. We call the highest (second highest) E_T electron in the event the first (second) electron.

4.3.1 Electron Clustering

A candidate electron begins as a calorimeter cluster in the CEM. The clustering procedure begins by searching for seed towers in the CEM, where a seed tower has transverse energy $E_T > 3$ GeV deposited. A seed tower and each of its neighboring

$E_T > 20$ GeV
$p_T > 13$ GeV
$E/p < 1.5$
$Lshr_2 < 0.2$
$Lshr_3 < 0.2$
E_{HAD}/E_{EM} (2 x 3) < 0.125
E_{HAD}/E_{EM} (3 x 3) < 0.05
$\|\delta x\| < 1.5$ cm
$\|\delta z\| < 3.0$ cm
$\chi^2_{strip} < 10.0$
$\|Z_v - Z_0\| < 5.0$ cm
$\|Z_v\| < 60.0$ cm
Conversion Rejection
Fiducial cuts on the electron

Table 4.4: *Cuts made offline to select the data sample used for the search. The electron identification variables are defined in Sections 4.3.2- 4.3.9*

towers in η with $E_T > 0.1$ GeV form an EM cluster[4].The highest E_T seeds are located first and the shoulder towers of each seed are not considered in subsequent searches for seed towers. The energy of the electron candidate is then the sum of energies deposited in the seed tower and its shoulder tower(s). To be called an EM cluster, $E_T > 5$ GeV is required. Corrections are made to the energy of an EM cluster to compensate for variable response across each tower, tower-to-tower gain variations, and time-dependent effects. A global correction to the energy scale is also imposed [34]. These corrections are typically a few percent.

To be considered an electron candidate a CTC track must point to a tower in the EM cluster. The highest p_T track pointing to the cluster is the "electron track." The measured direction of the track momentum sets the direction of the electron candidate.

We require that there be at least one EM cluster in the event with $E_T > 20$ GeV. We also require that at least one such EM cluster pass the electron identification requirements described in Sections 4.3.2- 4.3.9 and call that the *first tau candidate.* If there is more than one electron in the event that satisfies these requirements, then the first tau candidate is the electron candidate with the highest E_T.

We have verified the simulation of the measured electron E_T using the Tight

[4]If the seed tower is the outer most tower in η in the central detector, then it is only clustered with one shoulder tower.

$Z \to ee$ Data and MC Samples. Since we find good agreement, no systematic or scale factor is applied to the efficiency of the $E_T > 20$ GeV cut.

4.3.2 Fiducial Requirements

The electron track is required to originate no more then 5 cm from a vertex along the z direction as measured in the VTX ($|Z_e - Z_v| < 5$ cm). This vertex must lie within 60 cm (approximately 2σ) of the nominal collision point. This cut ensures that the track trajectories are in the same spirit as the projective design of the calorimeter.

Standard CDF fiducial cuts are made on the electron to ensure that the particle arrived at the calorimeter in an instrumented region with good response. The electron shower position as determined in the CES is required to lie within $x_{CES} < 21$ cm[5]to avoid the azimuthal cracks in the calorimeter. The track must not be incident on the calorimeter within $|z_{CES}| < 9$ cm, avoiding the uninstrumented region near $\theta = 90°$. The region $75° < \phi < 90°$ (called the "chimney") is also uninstrumented to allow connections to be made to the solenoid. No electron track may be incident on the chimney, nor in an outermost tower in η near $\eta = 1.0$ because an incident particle originating from the collision point will traverse a shallow depth in the calorimeter in this region.

[5]Here, x is defined within a tower to be the direction perpendicular to z and r, with $x_{CES} = 0$ at the center of the tower in ϕ.

4.3.3 Lateral Shower Profile

The lateral profile of the EM shower left by the first tau candidate is required to be consistent with electron shower profiles as measured in test beam data. The variable $Lshr$ is defined by:

$$Lshr = 0.14 \sum \frac{E_i^{Adj} - E_i^{Prob}}{0.14^2 E + (\Delta E_i^{Prob})^2} \tag{4.4}$$

where E_i^{Adj} is the measured energy in a tower (labeled i) adjacent to the seed tower and E_i^{Prob} is the expected energy in that tower based on the test beam measurements. $\sqrt{0.14E}$ appears in the denominator because it is the energy resolution of the EM Calorimeter. ΔE_i^{Prob} is the error on the test beam prediction. We require $Lshr < 0.2$.

4.3.4 Electron Shower Leakage in the Hadron Calorimeters

The EM calorimeters are designed to contain the complete electron showers. Hadrons will deposit energy in both the EM and HAD calorimeters. Thus, since the electrons from tau decays are not produced in association with nearby hadrons (as they would in semileptonic b decays), the ratio of energy measured in the CHA to energy measured in the CEM (E_{HAD}/E_{EM}) is used to identify electrons. We require $E_{HAD}/E_{EM} < 0.05$.

4.3.5 Energy to Momentum Ratio

An electron is expected to deposit energy in the EM calorimeter equal to the momentum of the electron track. We call the ratio of these two quantities E/p. A bremsstrahlung photon would tend to shower in the same tower as its parent electron, but the electron track momentum would be reduced, giving a higher E/p ratio. However, an even larger tail is seen from hadronic backgrounds from the process $\pi^0 \to \gamma\gamma \to \gamma e^+e^-$. We require $E/p < 1.8$.

4.3.6 Isolation

Electrons from tau decays are not expected to be produced in association with other particles. Therefore, we require that the first tau candidate is isolated in the calorimeter and in the tracking system.

In the calorimeter, we define:

$$Iso = \frac{E^{cone} - E^{cluster}}{E^{cluster}} \tag{4.5}$$

where E^{cone} is the energy deposited in the calorimeter in a cone of $\Delta R = 0.4$[6]around the first tau candidate and $E^{cluster}$ is the energy of the EM cluster. We require $Iso < 0.1$.

[6] $\Delta R = \sqrt{(\Delta\phi)^2 + (\Delta\eta)^2}$

We define N_{iso} to be the number of tracks with $p_T > 1$ GeV within $\Delta R < 0.524$[7]of the EM cluster. A track needs to have originated within 5 cm of the electron track along the beam line to be counted in the isolation cone. We require that $N_{iso} = 0$.

4.3.7 Matching tracks to CES position

A charged pion in the vicinity of a neutral pions decaying to two photons may fake an electron. To reduce this background, we require that the electron track projected to the plane of the CES is close to a shower position as measured in the CES. We require $|\delta x| < 1.5$ cm and $|\delta z| < 3.0$ cm.

4.3.8 CES profile

The CES clusters for electron candidates are 11 strips wide in z. The profile of the pulse heights across these strips is compared to electron test beam data and a χ^2 fit is performed. We require $\chi^2_{strip} < 10.0$.

4.3.9 Conversion Rejection

We reject electron candidates which are consistent with having originated from a photon that converted to an electron pair in the tracking material. A photon

[7]This cone size is 30°, chosen to be the same as the outer radius of the isolation annulus used for identifying hadronic taus.

which converts in the VTX would leave a track with low occupancy in that subdetector. Occ_{VTX} is the track occupancy in the VTX and so an electron is rejected if $Occ_{VTX} < 0.2$. Next, we search for the presence of a candidate electron partner. All tracks opposite in sign from the electron candidate are considered. If such a track is found within 90° in ϕ, separated in $r - \phi$ by no more than 0.3 and satisfying $\Delta \cot\theta < 0.06$ then the electron is a conversion candidate is therefore rejected.

4.3.10 Simulation of Electron Identification Variables

We assess the simulation of electron identification variables in QFL. Here, we consider the Loose $Z \rightarrow ee$ Data and MC Samples and in each sample we measure the efficiency of the electron identification cuts described above. The combinatorics need to be considered carefully for this study. The techniques used to account for combinatorics are described in Appendix C.

Figures 4.3 and 4.4 show the electron identification variables as observed in the data and simulation. The variables that show the largest discrepancy between data and simulation are: E_{HAD}/E_{EM}, $Lshr$, Iso and $|Z_e - Z_v|$. We account for all discrepancies at once by applying a scale factor to the simulated electron identification efficiency based on the measured efficiency from the data.

Table 4.5 shows the efficiency for each electron identification cut applied alone,

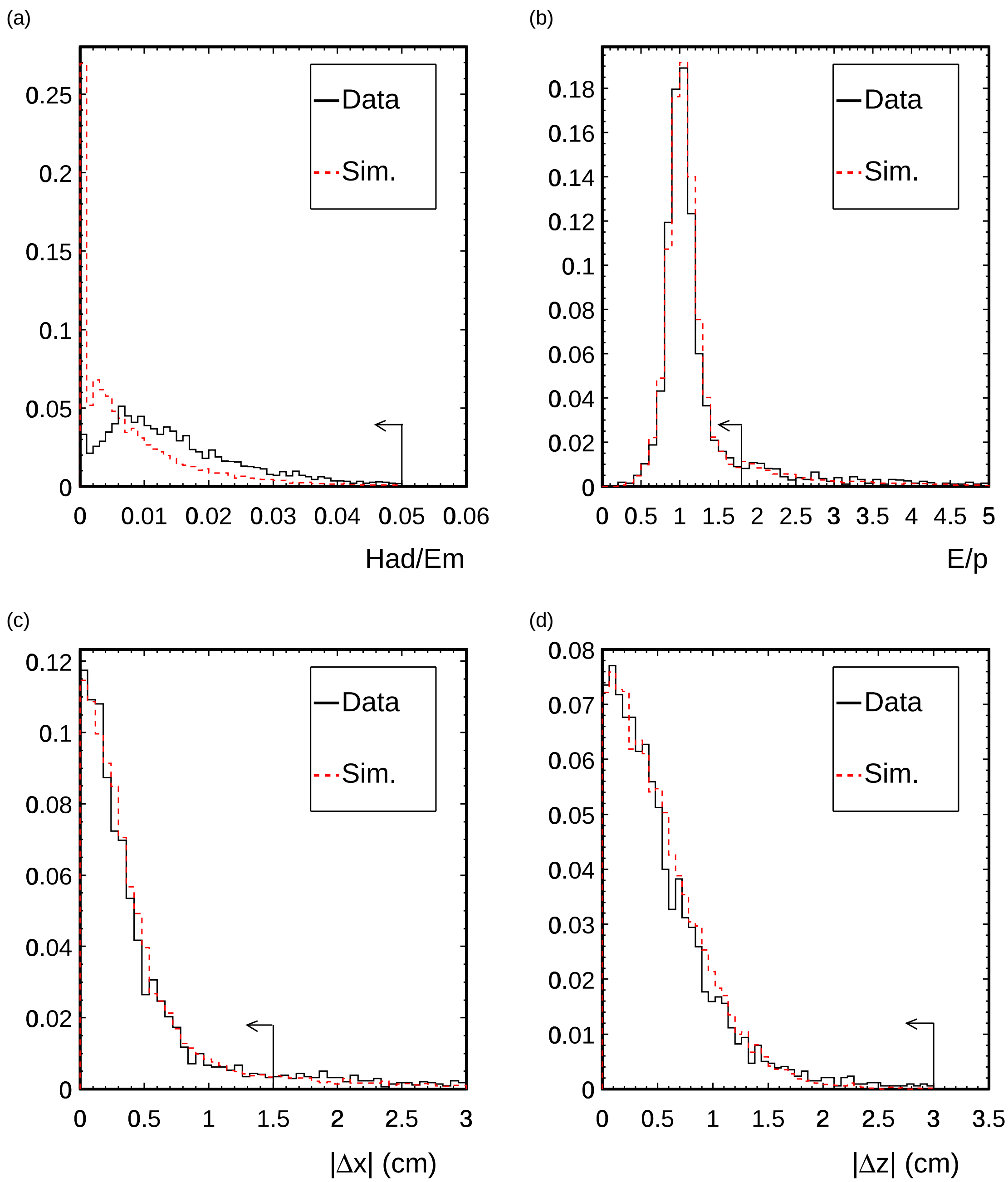

Figure 4.3: *Electron identification variables as measured in the Loose $Z \to ee$ Data Sample compared with QFL.*

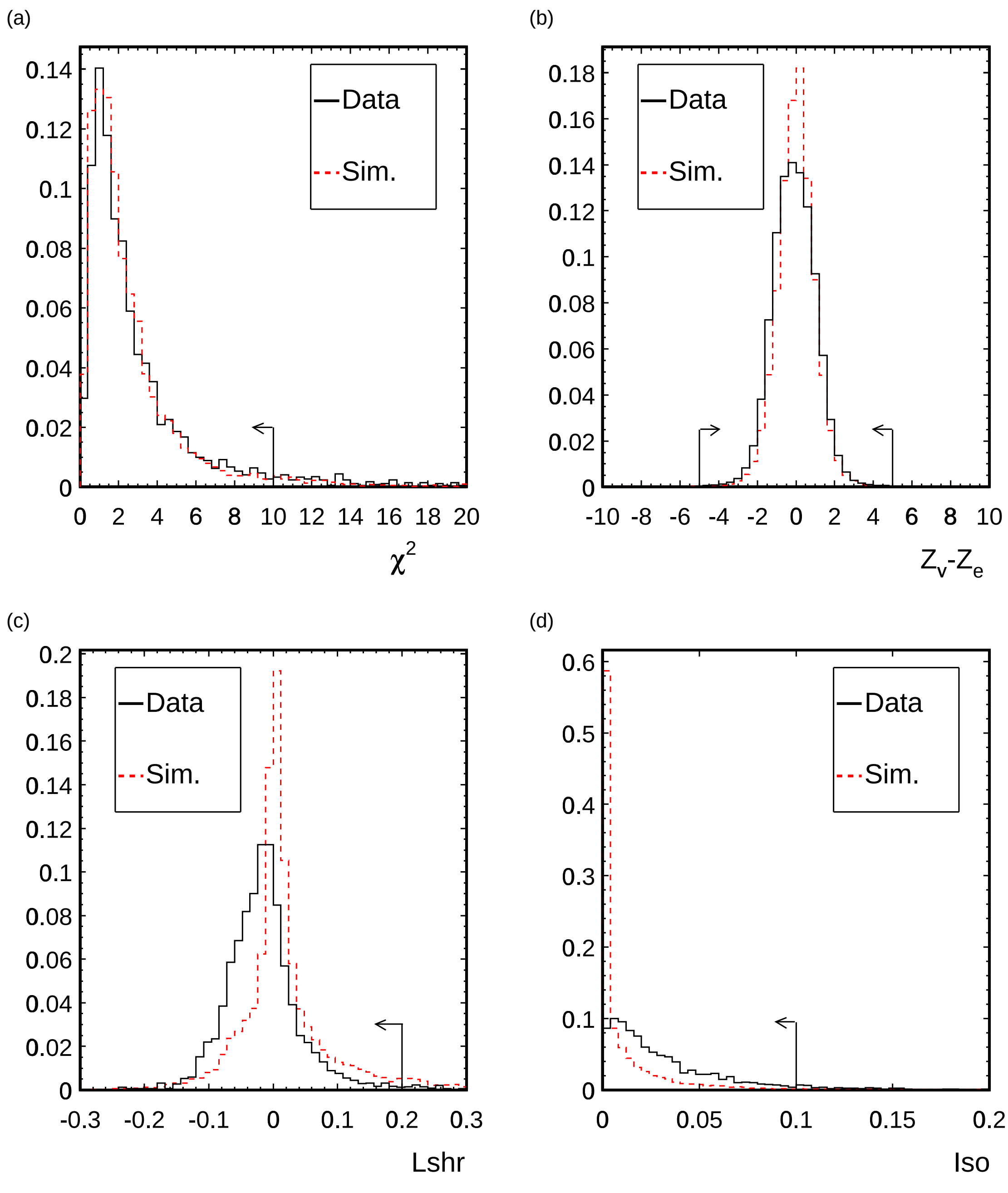

Figure 4.4: *Electron identification variables as measured in the Loose $Z \to ee$ Data Sample compared with QFL.*

comparing data with simulation. We have removed background contamination, which is assumed to have the same rate as same-sign events passing the same cuts, typically at a level of 1%. In the last row, we list the efficiency of all cuts applied cumulatively. All efficiencies in Table 4.5 are derived from Equation C.1 in Appendix C.

We also use the Loose $Z \to ee$ Data and MC Samples for a comparison of the measured efficiency of the tracking isolation cut, $N_{iso} = 0$. We consider only events where the second electron has passed all of the electron identification cuts described above. To calculate the efficiencies, we use the method described in Appendix C.3. The efficiency is $85.1 \pm 0.8\%$ from the data and $85.6 \pm 0.4\%$ from the MC. Although the two are consistent, they are each combined with the measured electron identification efficiencies measured above to get a total scale factor for electron selection.

We find that the scale factor we should apply to the simulation is:

$$k_1 = \frac{61.6 \pm 0.9}{70.9 \pm 0.4} = 0.869 \pm 0.016. \tag{4.6}$$

These studies were performed on electrons from $Z/\gamma^* \to ee$ events, which have a different E_T spectrum from electrons from tau decays in $Z/\gamma^* \to \tau\tau$ events. Therefore, we verify that the scale factor that we derive is not E_T dependent. The scale factor is shown binned in E_T in Figure 4.5. Although the scale factor cannot be said to be consistent with being flat in E_T, neither does it show a clear trend moving from high-E_T electrons from $Z \to ee$ events to low-E_T electrons in $Z/h \to \tau\tau$ events.

	Efficiency (%)	
	Data	Simulation
$E_{HAD}/E_{EM} < 0.05$	96.1 $\pm$ 0.5	98.6 $\pm$ 0.1
$Iso < 0.1$	96.1 $\pm$ 0.5	98.1 $\pm$ 0.1
$Lshr < 0.2$	98.2 $\pm$ 0.4	96.8 $\pm$ 0.2
$E/p < 1.8$	92.8 $\pm$ 0.5	93.2 $\pm$ 0.2
$\lvert\delta x\rvert < 1.5$ cm	93.3 $\pm$ 0.4	93.8 $\pm$ 0.2
$\lvert\delta z\rvert < 3.0$ cm	97.9 $\pm$ 0.4	98.7 $\pm$ 0.1
$\chi^2_{strip} < 10.0$	95.5 $\pm$ 0.5	96.6 $\pm$ 0.2
$\lvert Z_v\rvert < 60$ cm, $\lvert Z_v - Z_0\rvert < 5$ cm	94.4 $\pm$ 0.5	99.7 $\pm$ 0.1
Conversion Rejection	96.8 $\pm$ 0.5	97.7 $\pm$ 0.1
Total Cumulative	72.4 $\pm$ 0.8	82.8 $\pm$ 0.3

Table 4.5: *Efficiencies measured from the Loose $Z \to ee$ Data and MC Samples. Background contamination has been subtracted from the efficiencies measured from the data sample.*

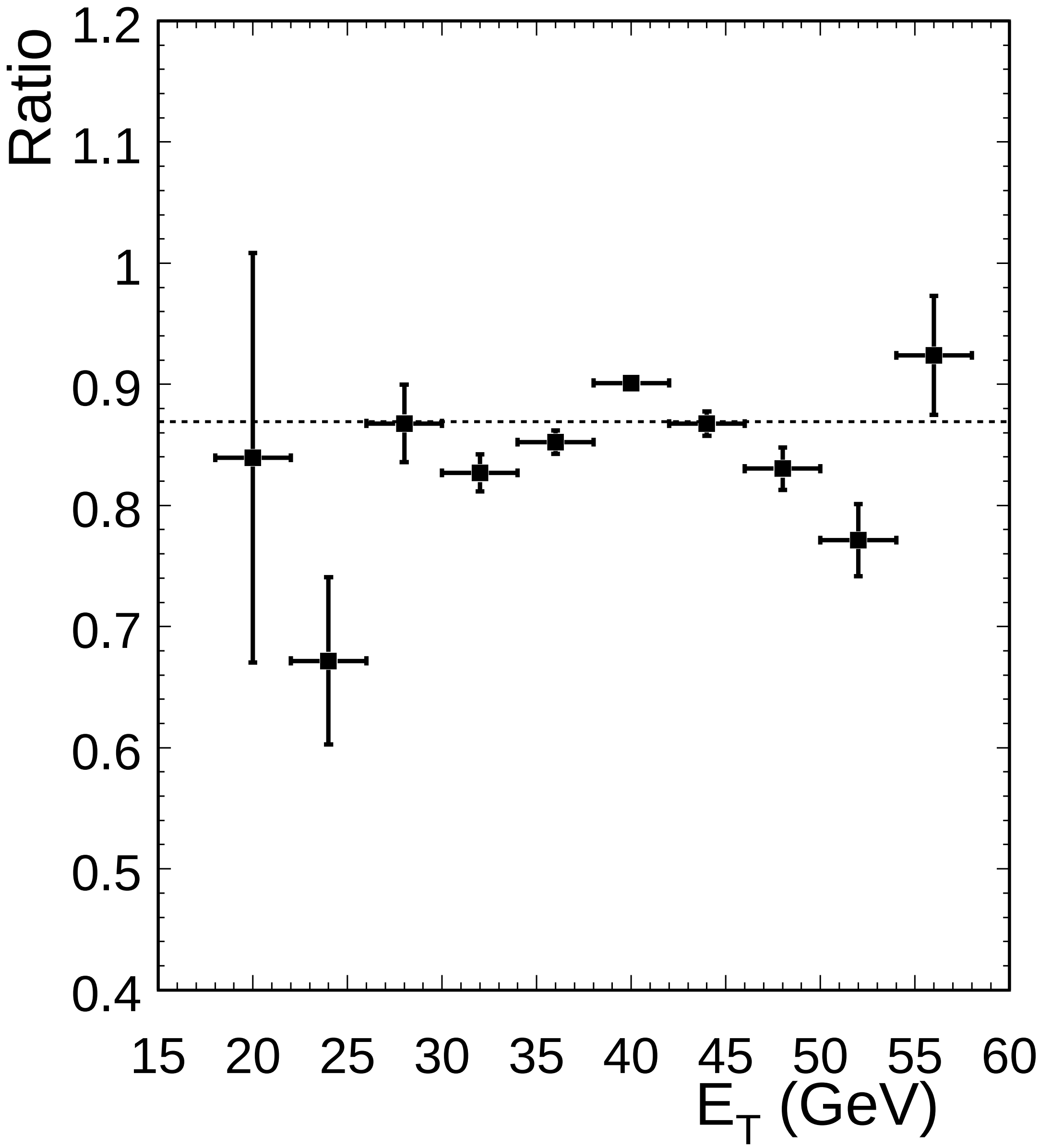

Figure 4.5: *Electron identification variables as measured in the Loose $Z \rightarrow ee$ Data Sample compared with QFL.*

4.3.11 Vertex Requirement

QFL smears the position of the vertices by a Gaussian distribution along the z axis with $\sigma = 30$ cm and centered at the nominal collision point. The data reveals that for a given run, the distribution of vertex positions is Gaussian, but across runs, the central value of the distribution varies on the level of a few centimeters. Also, the spread of the distribution shows an abrupt drop after run 60800. The vertex position is a crucial factor in determining whether or not a track falls in the fiducial region of the detector. Therefore, we force agreement between data and the simulation using the ARMCT.

4.4 Hadronic Tau Identification

Having located the first tau candidate in an event by looking for an EM cluster passing the stringent electron selection requirements, we then search for a hadronic tau in the same event. We call a hadronic tau candidate the *second tau candidate*, or τ_h. The tau identification cuts used here are based on those outlined in [35].

4.4.1 Hadronic Tau Properties

In the Higgs events of interest, the tau decay products are expected to be highly collimated, with an angular deviation from the direction of the tau parent of no more than $\Delta\phi \lesssim m_\tau/E_\tau$ which is $\sim 10°$ for a typical $E_\tau \sim 10$ GeV. From Table 4.1, in nearly all cases the tau decay products will include 1 or 3 charged tracks and ≤ 2 neutral pions each decaying to two photons.

4.4.2 Tau Seed Requirements

Kinematic Requirements

The search for a hadronic tau begins with identifying a stiff track associated with a jet cluster. We require a track with $p_T > 10$ GeV within $\Delta R < 0.4$ [8]of a jet cluster with $E_T > 10$ GeV. The jet energy used here does not include any corrections that are often made for detector effects. The track with the highest p_T satisfying this requirement is called the *tau seed*. Figure 4.7 shows the energy expected to be visible in the calorimeter from hadronic taus from signal events compared with a background-dominated data sample. Figure 4.6 shows the p_T of highest p_T charged particle associated with the hadronic tau candidate. The E_T cut is approximately

[8]Here we consider *particle* η (assuming the track and the jet each originate at $z = 0$) since there is no vertex measurement for a jet before requiring the existence of a track.

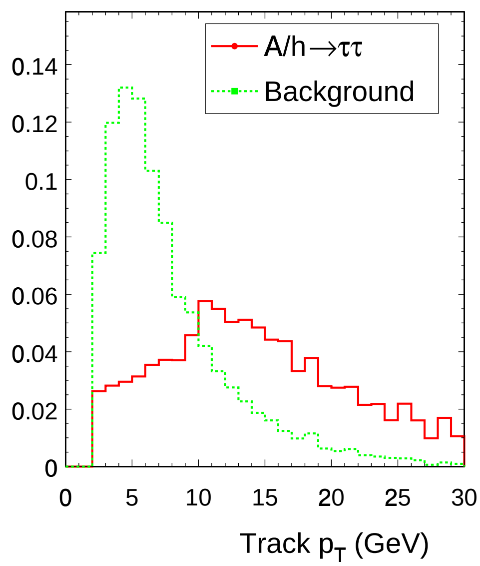

Figure 4.6: *This figure shows the transverse momentum of candidate seed tracks with $p_T > 2$ GeV. The red curve shows simulated signal events and the green curve is background-dominated data. Both curves are normalized to unity.*

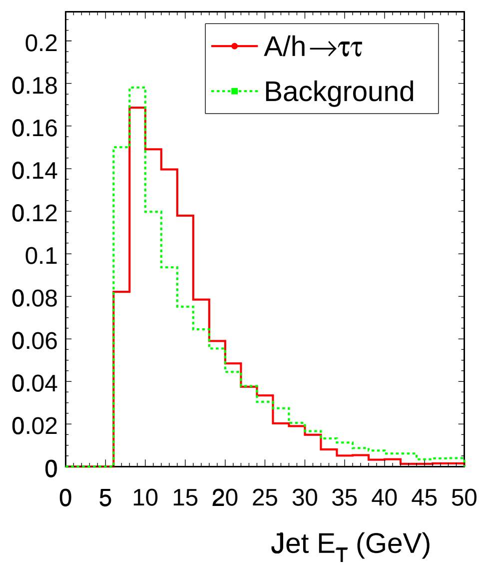

Figure 4.7: *This figure shows the transverse energy of tau candidates. The red curve shows simulated signal events and the green curve is background-dominated data. The sharp cutoff at* $E_T = 10$ *GeV is seen because a* $p_T > 10$ *GeV cut has already been imposed on the tau seed. Both curves are normalized to unity.*

75% efficient for signal while keeping 70% of the inclusive electron sample (where the tau candidate is predominantly a fake from a QCD jet). The p_T cut is approximately 65% efficient for signal and 20% efficient for QCD jets (after the E_T cut has already been imposed).

Fiducial Requirements

We make stringent fiducial requirements on the tau seed so that we may be sure that the tau candidate is well measured. The tau seed must satisfy $|\eta_d| < 1.1$ and $|z_{seed} + 130/\tan\theta_d| < 150$ cm. The former ensures that the track enters the central calorimeter and the latter that the particle stays within the tracking volume of the CTC up to its outer radius. The track must pass additional fiducial cuts similar to those imposed on the electron candidate to ensure that it is not incident on an uninstrumented portion of the calorimeter. Also, the tower that the track hits must read at least 0.5 GeV to guard against fake tracks. We define z^v_{seed} to be the closest primary vertex to the seed track and require $|z^v_{seed}| < 60$ cm and $|z^v_{seed} - z_{ele}| < 5$ cm, where z_{ele} is the position along z of the electron track.

4.4.3 Isolation

In the neighborhood of the tau seed, two isolation regions are considered separately with different requirements made in each region: the $\Delta R < 0.175$ cone and the $0.175 < \Delta R < 0.524$ annulus[9].

Tracking

In either isolation region, a track is a *shoulder* track if it satisfies $p_T > 1$ GeV, $|z_{sh} - z^{v}_{seed}| < 5$ cm, $|z_{sh}| < 60$ cm, and it deposits at least 0.5 GeV in the calorimeter tower that it hits. Here, z_{sh} is the position along z of the candidate shoulder track. The seed track is included in the track counting in the $R < 0.175$ cone.

We expect the number of tracks in the $\Delta R < 0.175$ cone (N^{trks}_{cone}) to be 1 or 3 (counting the seed track *and* shoulder tracks). We require $N^{trks}_{cone} < 4$. We then find the sum the charges of the tracks in the cone, which we call Q, and require $|Q|$=1. We also require that Q is opposite in sign from the electron charge.

We expect the number of tracks in the annulus $0.175 < R < 0.524$ around the tau seed (N^{trks}_{ann}) to vanish in signal events, so we require $N^{trks}_{ann} = 0$.

These tracking isolation cuts are approximately 80% efficient for signal events and 20-30% efficient for QCD jets[10].

---

[9] A cone size of 0.175 (0.524) radians corresponds to 10° (30°).

[10] Tau fake rates depend the control sample being considered, as described in Section 6.2.

CES

The CES clustering algorithm used is a modified version of the one used in previous CDF analyses [35]. The modifications made allow us to cut on CES cluster multiplicities in the annulus around the tau seed track. Also, we introduce some additional requirements (such as fiducial requirements) which are necessary for good agreement between data control samples and simulated MC.

The CES clustering algorithm treats data samples and simulated MC samples identically. The algorithm begins by looking for CES clusters in the $\Delta R < 0.6$ cone around each track in the event with $p_T > 4.5$ GeV. For each calorimeter tower in the cone, the algorithm finds the strip (wire) with the highest measured energy. If this strip (wire) carries a pulse height above 0.4 (0.5) GeV, then it is a strip (wire) seed. The seed, along with its 4 (6) nearest neighboring strips (wires) form a strip (wire) cluster. Next, the algorithm finds the next highest energy strip (wire) which is not already part of a cluster and the process continues until there are no strips or wires left above the seed threshold which have not been included in a cluster. The cluster position relative to the tower center is defined as the position of the center strip or wire in the cluster. This is then translated into a cluster ϕ or η position depending on the position of the tower. Pulse heights from strips and wires were corrected for $\eta-$ and $\phi-$dependent effects, measured from test-beam data. The energy of a cluster in a tower is recorded as the CEM energy of that tower, weighted by the energy deposited in the CES by that cluster compared to the energy deposited by all clusters in the tower. The predicted response in the CEM for a charged pion is subtracted from the energy in the tower impacted by the seed track.

A wire cluster in the $r-\phi$ view is matched to a strip cluster in the z view if their energies differ by no more than 1 GeV, and this cut is loosened to 5 GeV if the energy of each is greater than 10 GeV. If the sum of the energies of two strip clusters matches the energy of a wire cluster within 1.0 GeV, the three clusters are matched to form a single cluster. If the energies being compared are greater than 10 (20) GeV, the requirement is loosened to 5 (50) GeV. The same is not done for two clusters that differ in $r-\phi$ but match in z because of the wire cluster size is larger, so those tend to get merged anyway. If no wire cluster matches a strip cluster with $E >$1 GeV, then the cluster is still kept, and the ϕ of that cluster is taken to be the center of that tower. A CES cluster must satisfy $E_T > 1$ GeV to be counted as a *shoulder cluster* in one of the isolation regions.

A χ^2 requirement was used in previous CDF analyses to ensure that the CES cluster is consistent with electron test beam data. To avoid rejecting clusters where two photon clusters are merging into one cluster (we find that approximately 5-10% of taus were lost to this cut), the requirement is removed.

Some additional requirements on the CES clusters are necessary for good agreement between data and simulated MC. To improve the agreement between data and CDF simulation, some additional requirements are made on the CES clusters. First, the cluster position must not be consistent with coming from the seed track (the cluster is rejected if $|\eta_d^{seed} - \eta_d^{cluster}| < 0.03$ and either $|\phi^{seed} - \phi^{cluster}| < 0.01$ or $|\phi^{tower\ center} - \phi^{cluster}| < 0.01$ [11]). Finally, the cluster must not come from a region near a crack in the CES, where the cluster has the potential to be counted twice, once in each side of the crack.

We call the number of CES clusters found in the isolation cone (annulus) N_{cone}^{ces} (N_{ann}^{ces}) and require $N_{cone}^{ces} < 3$ and $N_{ann}^{ces} = 0$. In addition, in the cone, the CES cluster energies measured as 3-component vectors are combined with the measured momenta of the tracks to compute a tau mass, m_τ. We require $m_\tau < 2.0$ GeV. The cuts on N_{cone}^{ces}, N_{ann}^{ces} and m_τ give a combined efficiency for signal of approximately 95%. These three cuts keep 50-70% of QCD jets.

Simulation of Isolation Variables

As described above, a tau candidate is determined to be isolated through a measurement of track and CES cluster multiplicities in the neighborhood of a seed track.

[11] Remember that if no wire information is available, the cluster position is assigned to the center of the tower in ϕ.

We use the Tight $Z \to ee$ Data and MC Samples, the Tight $Z \to \mu\mu$ Data and MC Samples, and the $Z \to \tau\tau$ MC Sample[12]. to compare simulation to data, and cross-check events with electrons to events with muons. In the $Z \to ee$ and $Z \to \mu\mu$ samples, both lepton candidates in each event are considered *seeds*, each seed mimicking the tau seed in the analysis. In the $Z \to \tau\tau$ sample, we consider only hadronic tau decays. In the $Z \to \tau\tau$ MC Sample, we select tau seeds as described in Section 4.4.2.

We count the number of tracks found in the region near the seeds in the five samples. We compare $Z \to \tau\tau$ with the other samples only when considering the region outside the 0.175 cone so that none of the tracks or CES clusters found are from decay products of the tau. The criteria for a track other than the seed (in the isolation region being considered) to be counted are described in 4.4.3.

In Figure 4.8 we plot the mean number of tracks in the $\Delta R < 0.175$ cone around the seeds in the $Z \to ee$ and $Z \to \mu\mu$ data and MC samples. Agreement is good between data and MC, and between electrons and muons.

In Figure 4.9 we plot the mean number of tracks in the $0.175 < \Delta R < 0.524$ radian annulus around the seeds in all five samples. Agreement is good between data and MC, and between electrons, muons and taus. Both data and MC show an E_T dependence which is not understood, but since the agreement between data and MC

[12] These samples are all described in Appendix B.

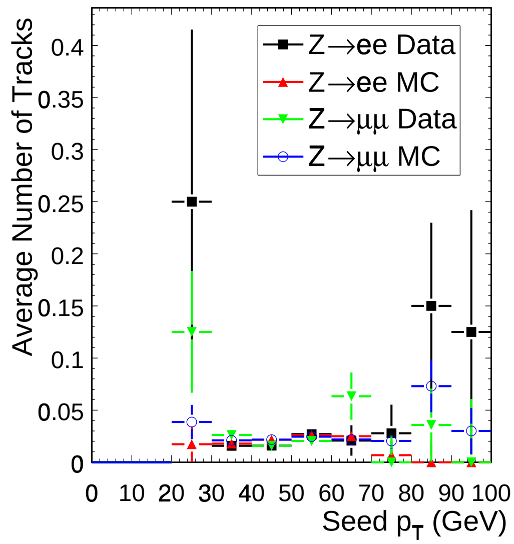

Figure 4.8: *Average number of tracks in the* $\Delta R < 0.175$ *cone surrounding the tau seed in the control samples considered.*

is good, this E_T dependence does not introduce a systematic error on the modeled efficiency.

In Figure 4.10 we plot the mean number of CES clusters in the 0.175 radian cone surrounding the seeds in the Tight $Z \to ee$ and $Z \to \mu\mu$ Data and MC Samples. There is a significant discrepancy between electrons and muons. From the $Z \to ee$ MC sample we find that the expected contribution from bremsstrahlung photons is the correct size to account for the difference.

Figure 4.11 shows the mean number of CES clusters in the 0.175-0.524 radian annulus around the seeds from the all five samples. The figure shows good agreement

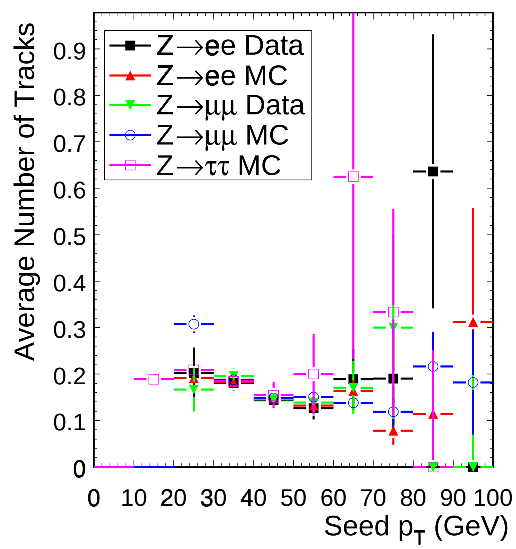

Figure 4.9: *Average number of tracks in the* $0.175 < \Delta R < 0.524$ *annulus surrounding the tau seed in the control samples considered.*

between data and simulation.

Simulation of CES Cluster Energies

Recall that the CES cluster energies are derived from the energy deposited in the CEM weighted by the relative charge observed in clusters within a tower. The CES cluster energies from the CES clustering algorithm are used only in measuring the tau mass, and the efficiency of the m_τ cut imposed is nearly 100%[13].

We use the Conversion Data Sample and the Conversion MC Sample described in

[13] Actually, the CES cluster energies are also to used to test that the cluster in the isolation region passes the 1 GeV threshold required to be counted.

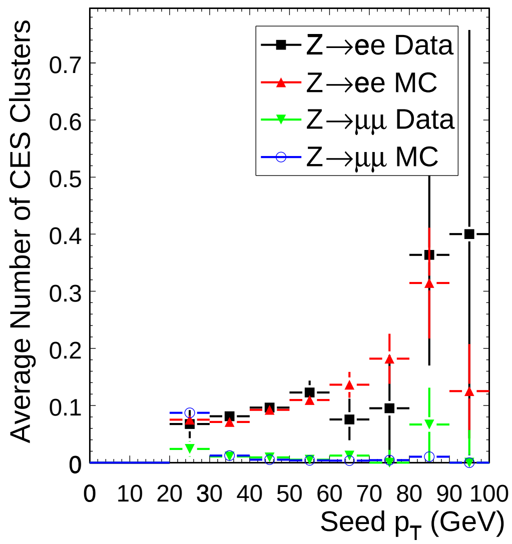

Figure 4.10: *Average number of CES clusters in the $\Delta R < 0.175$ cone surrounding the tau seed in the control samples considered.*

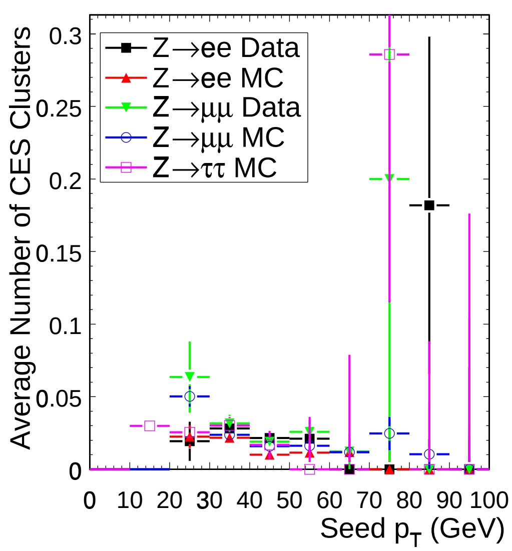

Figure 4.11: *Average number of CES clusters in the $0.175 < \Delta R < 0.524$ annulus surrounding the tau seed in the control samples considered.*

Appendix B for this study so that we may use the low p_T electrons from conversion pairs to measure the resolution of the CES cluster energy measurement.

We require that one electron in the event passes the electron identification cuts described in Section 4.3.1 (call this the "first electron"), with the E_T cut loosened to 10 GeV for increased statistics. We then select events with an opposite sign track consistent with forming a vertex with the first electron in the region where the VTX lies ($25 < r < 29$ cm). Low multiplicity in the VTX is also required. This second track is called the *partner electron*.

Figure 4.12 shows the fractional difference between the CES cluster energy associated with the partner electron and the momentum of the track, plotted against CES cluster energy. CES cluster energies from *both data and MC* are given an energy dependent correction factor measured from the data (the black curve in Figure 4.12) so that the cluster energy is on average the same as the track momentum. Although a systematic difference between the data and MC curves is apparent, this has a negligible effect on the analysis since the efficiency of the m_τ cut on the second tau candidate in the simulated samples is nearly 100%.

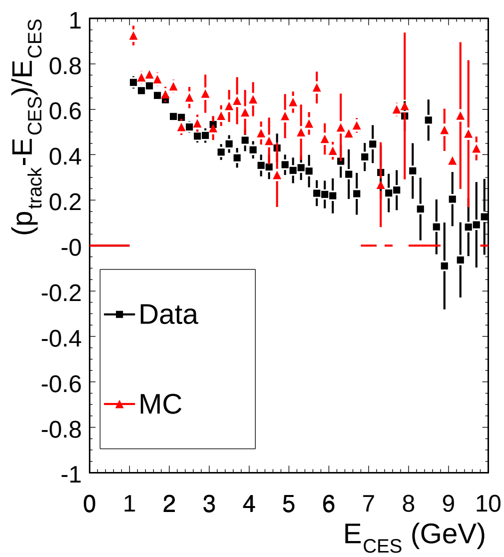

Figure 4.12: *Comparing the CES cluster energies to track momenta from conversion electrons. Notice that if the CES cluster energies were properly measured then all points would lie at* $(p_{track} - E_{CES})/E_{CES} = 1$.

4.4.4 Electron Rejection

We reject events where both taus decay to electrons to reduce to impact of $Z/\gamma \rightarrow ee$ background on the sensitivity. We use the method used in previous CDF analyses involving taus [48]. We define:

$$\xi = \frac{E_T^{had}}{\Sigma p_T} \tag{4.7}$$

where Σp_T is the sum in p_T of all tracks with $p_T > 1$ GeV within the cone $\Delta R < 0.175$ surrounding the jet direction. Uncorrected jet E_T is used. We require $\xi > 0.15$.

We use the Loose $Z \rightarrow ee$ Data and MC Samples to get a scale factor or systematic error for this cut. We measure the rate at which the electrons passing loose requirements in each sample pass the $\xi > 0.15$ requirement. The level of background is measured from same-sign events and is accounted for in the measurement. Before it is considered for this study, the electron must deposit at least 0.5 GeV in the calorimeter tower on which it is incident, it must be in the fiducial region, and it must satisfy $p_T > 5$ GeV. In Figure 4.13, we plot ξ as measured in the data and MC samples. We find that 1.9 $\pm$ 0.5 % of the data events and 1.0 $\pm$ 0.1 % of the MC events pass $\xi > 0.15$. This leads us to a scale factor of

$$k_2 = \frac{1.9 \pm 0.4\%}{1.0 \pm 0.1\%} = 1.9 \pm 0.4. \tag{4.8}$$

This scale factor is only applied to events where the second tau candidate is a real

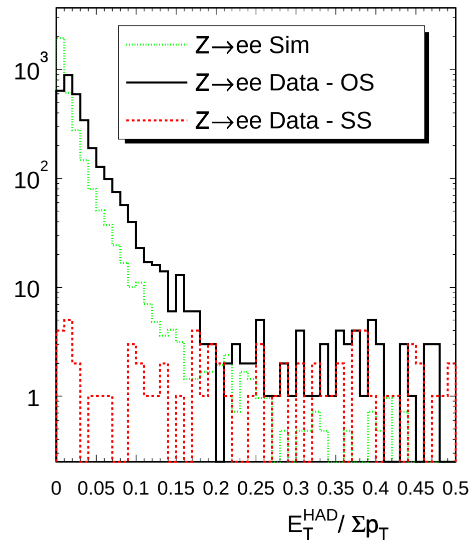

Figure 4.13: *The variable used to reject electrons as observed in $Z \to ee$ data and MC samples. For the data sample, the opposite-sign events and same-sign events are shown separately.*

electron which passes the $\xi > 0.15$ cut in the simulation. This represents a fraction of an event as modeled in each of the $Z \to ee$ and $Z \to \tau\tau$ MC samples, and even fewer in the $A/h \to \tau\tau$ samples.

This variable is also not modeled sufficiently for hadronic decays. From studies of isolated pions [49], the hadronic energy deposited by charged pions is underestimated by QFL, so that QFL underestimates the efficiency of this cut. Since the size of this discrepancy is difficult to quantify, we take the efficiency to be the average of the QFL efficiency for hadronic taus and 100%, which is $(100.0{+}95.5)/2 = 97.8\%$. The systematic error on this cut is half the difference between the QFL efficiency and

100%, which is (100.0-95.5)/2 = 2.2%..

4.4.5 Jet Width

Since the decay products of a hadronically decaying tau are highly collimated, such a tau should leave a narrow cluster of energy in the calorimeter. We cut on the $\phi-\phi$ and $\eta-\eta$ moments of the jet cluster associated with the hadronic tau candidate which are defined as follows:

$$I_{\phi-\phi} = \frac{\sum_i {E_T}^i \cdot (\phi_i - \phi_0)^2}{\sum {E_T}^i} \tag{4.9}$$

$$I_{\eta-\eta} = \frac{\sum_i {E_T}^i \cdot (\eta_i - \eta_0)^2}{\sum {E_T}^i}. \tag{4.10}$$

The sum is over calorimeter towers in the jet cluster, and ϕ_0 and η_0 are the E_T weighted center of the jet in the ϕ and η directions. We require $I_{\phi-\phi} < 0.1$ and $I_{\eta-\eta} < 0.1$. Figures 4.15 and 4.14 show $I_{\phi-\phi}$ and $I_{\eta-\eta}$ from simulated hadronic tau decays compared with jets from the Jet20 data sample. These two cuts together reject approximately 30-45% of QCD jets.

Studies of isolated pions [49] have shown that QFL overestimates the width of jets from charged pions. This means that QFL would only underestimate the efficiency of this cut on the hadronic tau candidates. Therefore, we take the efficiency to be the average of the QFL efficiency and 100%, which is (100.0+92.2)/2 = 96.1%. The

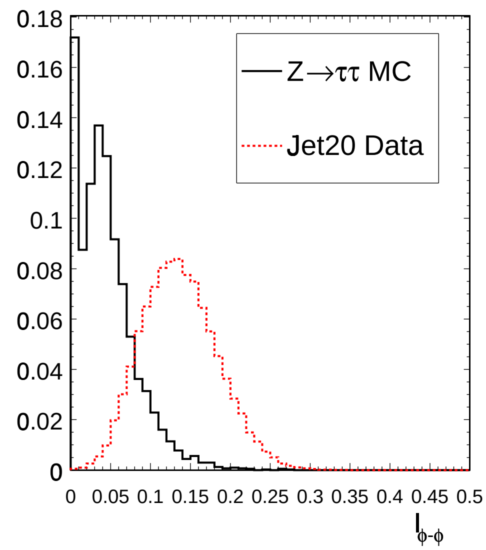

Figure 4.14: *Comparing $I_{\phi-\phi}$ for simulated hadronic tau decays and jets from the Jet20 data sample.*

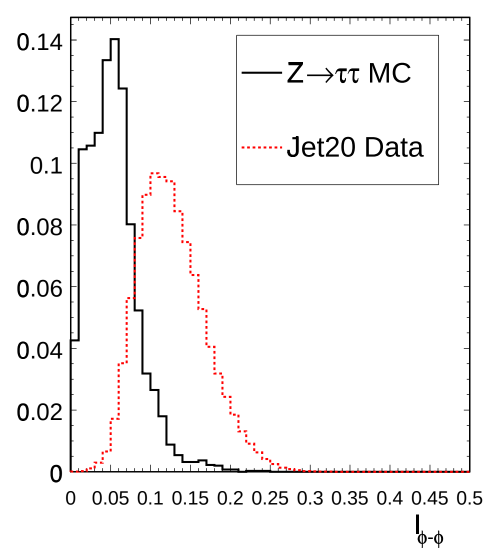

Figure 4.15: *Comparing $I_{\eta-\eta}$ for simulated hadronic tau decays and jets from the Jet20 data sample.*

systematic error on this cut is half the difference between the QFL efficiency and 100%, which is (100.0-96.1)/2 = 3.9%.

From the Loose $Z \to ee$ Data and MC Samples, we find that this cut is nearly 100% efficient for electrons. This means that no systematic or scale factor needs to be applied to the simulated efficiency for $Z \to ee$ events, and that neutral pions are not expected to contribute significantly to the systematic error on simulated di-tau events.

4.5 Tau Efficiencies

Figure 4.16 shows the efficiency of the hadronic tau identification cuts on hadronic taus as seen in the simulation, after each cut is applied in succession. We bin the efficiencies according to the E_T of the visible energy from the tau as seen at the generator level. The total efficiency plateaus near 55% for $E_T \gtrsim 35$ GeV. Of course, not all taus are in this high E_T region. For hadronic taus from $Z \to \tau\tau$ events that lie in the fiducial region and satisfy $E_T > 10$ GeV, 40% pass all of the tau identification cuts.

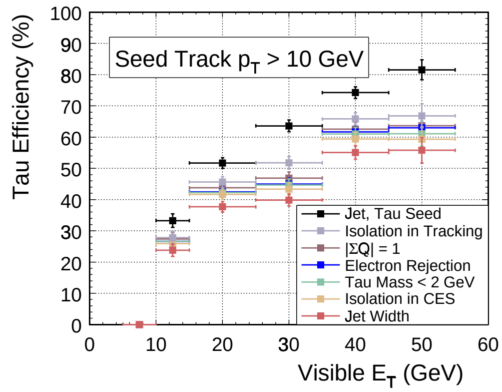

Figure 4.16: *Efficiencies of the tau identification cuts applied to hadronic taus from* $Z \to \tau\tau$ *events* .

4.6 Opposite Sign Requirement

We also require that the sum of the measured charges of the tracks in the 10° cone surrounding the hadronic tau candidate is opposite in sign from the first tau (the electron candidate). The efficiency of this cut is measured from data control samples as described in Chapter 6.

4.7 Kinematic Requirements

4.7.1 Jet Multiplicity

For this cut only, we define a jet the same way as in the CDF W+jets analysis [36] and call the number of such jets N_{jets}. We consider jet clusters in the region $|\eta| < 2.4$.

We do not include jets that qualify as EM clusters, so the first tau candidate is not counted, but the second tau candidate and any recoil QCD jet may be included in N_{jets}. Any pair of jet clusters less than 0.52 radians apart, each with $E_T > 12$ GeV are combined into a single jet. Then, N_{jets} is the number of jets with $E_T > 15$ GeV. Here, we use jet energies corrected for detector effects such as variations in detector response tower-to-tower and over the time span of the run. The corrections are η-and run-dependent and they also include an overall scale factor [37].

From the Loose $Z \to ee$ Data and MC Samples, we determine that there is sufficient agreement between data and MC so that we do not apply a scale factor or a systematic error to this cut.

4.7.2 $Z \to ee$ Rejection

We reject any event with two electrons or one electron and one track which reconstruct a mass M_{ee} between 70 and 110 GeV. This is approximately 99% efficient in removing $Z \to ee$ events while rejecting approximately 10% of signal events.

The Tight $Z \to ee$ Data and MC samples are used to assess the simulation of the variable M_{ee}. We consider events in the region $66 < M_{ee} < 116$ GeV. Since we reject events in the region $70 < M_{ee} < 110$ GeV, we compare the number of events which lie in the regions $66 < M_{ee} < 70$ GeV and $110 < M_{ee} < 116$ GeV in data and MC. We find 20/1822 events in the data for an efficiency of $1.10 \pm 0.24\%$ and 117/8096 events in the MC for an efficiency of $1.45 \pm 0.13\%$. Since the rate at which events appear in the tails of these two distributions are consistent between the samples within errors, we do not apply a scale factor or a systematic for this variable.

4.7.3 Tau Candidates are Away

We require that the tau candidates be away from one another in the azimuthal plane, $|\Delta\phi_{\tau_l,\tau_h}| > 1.5$. This is nearly 100% efficient for signal while 80% efficient for non-tau backgrounds as measured from a background-dominated data sample.

4.8 Mass Reconstruction

Di-tau events will contain at least two neutrinos, which escape CDF undetected. At hadron colliders, the resulting energy imbalance may only be determined in the transverse plane because the center-of-momentum of the interaction is not known along the z direction [14].

However, the energy of the neutrinos from each tau decay, and thus the full mass of the di-tau system, may be deduced if [38], [39], [40].

[14] CDF sits in the center-of-momentum frame of the collisions between protons and anti-protons, but the interactions occur between partons (the quarks, anti-quarks and gluons that make up the protons and anti-protons.)

1. The tau candidates are not back-to-back in the azimuthal plane

2. The neutrino directions are assumed to be the same as their parent taus

We solve a system of two equations and two unknowns, where the unknowns are the contributions to the event missing energy from each τ ($\not{E}_l$ and $\not{E}_h$, the l and h subscripts denoting the leptonically and hadronically decaying taus, respectively.).

$$(\not{E}_l)_x + (\not{E}_h)_x = (\not{E}^{meas})_x \tag{4.11}$$

$$(\not{E}_l)_y + (\not{E}_h)_y = (\not{E}^{meas})_y. \tag{4.12}$$

Here, $(\not{E}^{meas})$ is the missing energy measured for the event. Equations 4.11 and 4.12 may be written,

$$\not{E}_l \cos\theta_l \cos\phi_l + \not{E}_h \cos\theta_h \cos\phi_h = (\not{E}^{meas})_x \tag{4.13}$$

$$\not{E}_l \cos\theta_l \sin\phi_l + \not{E}_h \cos\theta_h \sin\phi_h = (\not{E}^{meas})_y \tag{4.14}$$

where $\theta_{l,h}$ are the polar angles of the taus and $\phi_{l,h}$ are the azimuthal angles of the taus. The tau candidate directions are measured from the visible decay products.

Figure 4.17 highlights the reason for the first of the two criteria for the mass technique outlined above. When the tau candidates are back-to-back in the azimuthal plane, the system of equations tends to give many high mass, nonsense solutions. We

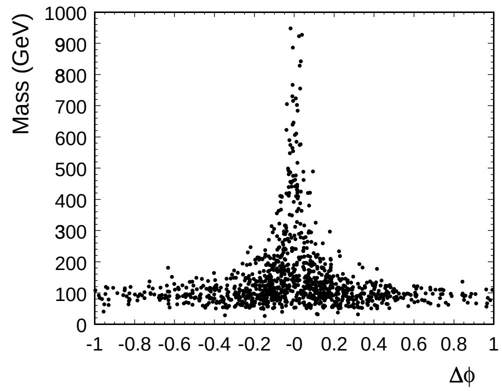

Figure 4.17: *Reconstructed di-tau mass plotted against the azimuthal angle between the tau candidates. Here, only events with a nonzero solutions for* $\not{E}_l$ *and* $\not{E}_h$ *appear on this plot.*

have chosen $|\sin \Delta\phi| > 0.3$ to select non-back-to-back events. This cut is approximately 20% efficient for $A/h \to \tau\tau$ and $Z \to \tau\tau$ events. With a stiffer cut, the mass resolution would improve, as can be seen from Figure 4.17, but the efficiency of the $|\sin \Delta\phi|$ cut would be significantly degraded. Figure 4.18 shows the steeply falling $\Delta\phi$ distribution for signal events.

The second of the criteria is necessary since we do not detect the directions of the neutrinos as they leave the detector. As mentioned above, the decay products of a tau in the events of interest are deflected by no more than $\sim 10^\circ$.

Due to the the criteria necessary for the mass technique and due to the resolution of the detector, some events may give negative solutions for $\not{E}_l$ and $\not{E}_h$. We require $\not{E}_{l,h} > 0$ for the non-back-to-back events. This reduces non-di-tau backgrounds in

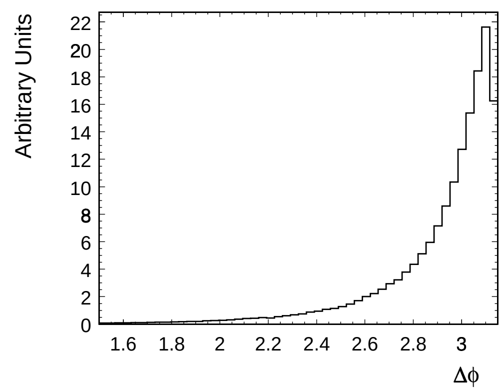

Figure 4.18: *Azimuthal angle* $\Delta\phi$ *between the taus in* $A/h \to \tau\tau$ *events for* $m_A = 100$ *GeV,* $\tan\beta = 50$.

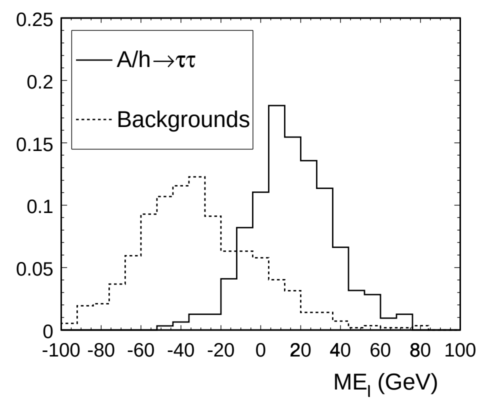

Figure 4.19: $\not\!\!E_l$ *from simulated* $A/h \to \tau\tau$ *events compared with a background-dominated data sample.*

this region. Figures 4.19 and 4.20 show $\not\!\!E_l$ and $\not\!\!E_h$ from a background-dominated sample of the data compared with simulated $A/h \to \tau\tau$ events. The $\not\!\!E_{l,h} > 0$ requirement is 55-60% efficient for signal, increasing with mass, while reducing non-di-tau background by approximately a factor of 10. When the di-tau mass is reconstructed

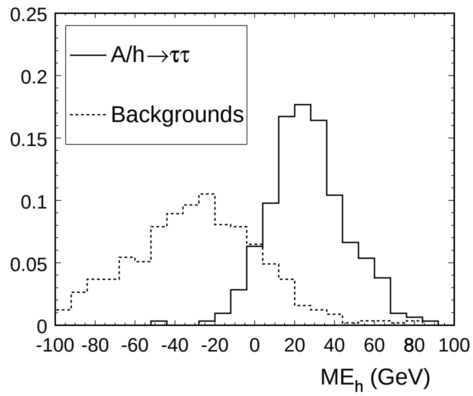

Figure 4.20: $\not{E}_h$ *from simulated* $A/h \to \tau\tau$ *events compared with a background-dominated data sample.*

as described next, this cut also improves the mass resolution.

The total reconstructed mass is calculated from

$$\begin{aligned} m^2_{Z/h} &= (p_l + p_h)^2 \\ &= p_l^2 + p_h^2 + 2p_l \cdot p_h \\ &= 2m_\tau^2 + 2E_l E_h(1 - \cos\psi) \\ &= 2m_\tau^2 + 2(\not{E}_l + E_l^{vis})(\not{E}_h + E_h^{vis})(1 - \cos\psi) \end{aligned}$$

where p_l and p_h are the 4-momenta of each tau, and E_l and E_h represent the total energy of each tau. E_l^{vis} and E_h^{vis} represent the energy left by their visible decay products. ψ is the angle between the two taus in 3-d space. $\not{E}_l$ and $\not{E}_h$ are together the solution to Equations 4.11 and 4.12.

Figure 4.21 shows the di-tau mass distribution reconstructed from events contain-

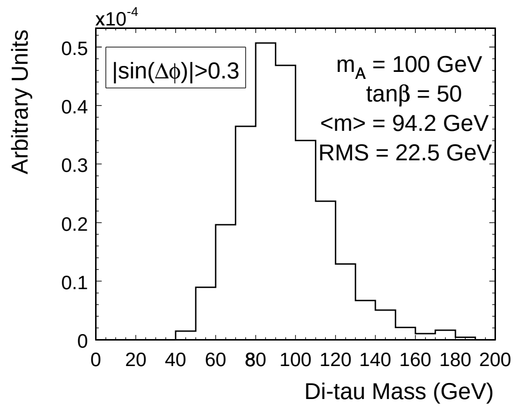

Figure 4.21: *Di-tau mass distribution as modeled in Pythia 6.203 + QFL.*

ing a directly produced Higgs for the parameter point $m_A = 100$, $\tan\beta = 50$. For this parameter point, the A or h particle has an inherent width of 5.7 GeV. The contribution from the calorimeter resolution may be qualitatively seen from Figure 4.22 below, since $Z \to ee$ events would have a vanishing measured missing energy in the transverse direction in an ideal detector. The remaining contribution to the width of the distribution in Figure 4.21 comes from the two criteria that were necessary to implement the technique. Notice that the mass reconstruction gives a mean that is low by approximately 6%.

4.9 Missing Transverse Energy

We call the event-wide energy imbalance in the transverse plane the missing transverse energy ($\not{E}_T$). Theoretically, $\not{E}_T$ is equal in magnitude to the sum of visible energy in the event, pointing in the opposite direction in the azimuthal plane. In practice, the measured magnitude and direction of the $\not\!\!E_T$ depends on whether or not we include jet energy corrections, electron energy corrections, etc. First, we define uncorrected $\not\!\!E_T$ in the following way:

$$\vec{\not\!\!E_T}^{uncorr} = -\sum_{towers} \vec{E_T}^{i} - \sum_{muons} \vec{p_T}^{j}. \tag{4.15}$$

The first sum is over the calorimeter towers where we add the transverse component of the energy deposited in each tower. The second sum is over the transverse momenta of the muon candidates.

We define a corrected $\not\!\!E_T$ as

$$\vec{\not\!\!E_T}^{corr} = \vec{\not\!\!E_T}^{uncorr} - \Delta\vec{E_T}^{ele} - \sum_{jets} \Delta\vec{E_T}^{i} \tag{4.16}$$

where $\Delta\vec{E_T}^{ele}$ is the transverse component of the energy correction applied to the electron candidate, and the final term accounts for the energy corrections applied to jets.

We do not make a straight cut on $\vec{\not\!\!E_T}^{corr}$. However, for the non-back-to-back events, we use the magnitude and direction of $\vec{\not\!\!E_T}^{corr}$ to find $\not\!\!E_{l,h}$ so that we may calculate the di-tau mass as outlined in the previous section. If we were to use the uncorrected quantity, the di-tau mass that we calculate would on average be too low.

It is necessary to verify that $\vec{\not\!\!E_T}^{corr}$ (magnitude and direction) is well modeled

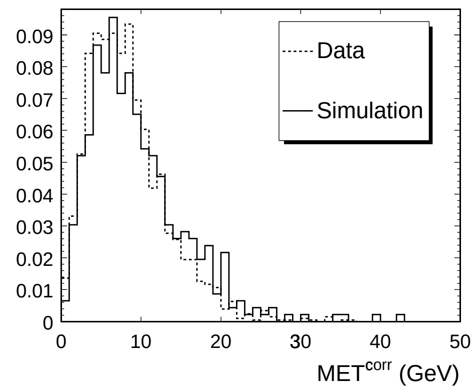

Figure 4.22: $\not\!\!E_T{}^{corr}$ *as measured in the Tight* $Z \to ee$ *Data and MC Samples for events where* $p_T^Z > 15$ *GeV.*

to be confident that the efficiency for the $\not\!\!E_{l,h} > 0$ cut from QFL is correct and to be confident that di-tau mass is properly simulated. We compare the Tight $Z \to ee$ Data and MC Samples for this verification. As described in Section 4.8, the di-tau mass may only be reconstructed when the taus are not back-to-back, and that the $|\sin\Delta\phi| > 0.3$ requirement is nearly equivalent to a $p_T^{A,h,Z} > 15$ GeV cut. Therefore, it is necessary for the simulation to model the data well only in the region $p_T^{A,h,Z} > 15$ GeV. We use the Tight $Z \to ee$ Data and MC Samples to validate the simulation in this region. In Figure 4.22, we plot $\not\!\!E_T{}^{corr}$ only for events where $p_T^Z > 15$ GeV, where p_T^Z is the sum of the transverse momenta of the two electron candidates in each event. We find good agreement in this region. It is also important that the direction of $\vec{\not\!\!E}_T{}^{corr}$ is well modeled because it impacts the $\not\!\!E_{\tau_1,\tau_2} > 0$ cut and the di-tau mass reconstruction. Figure 4.23 shows good agreement in the relevant region of $p_T^Z > 15$

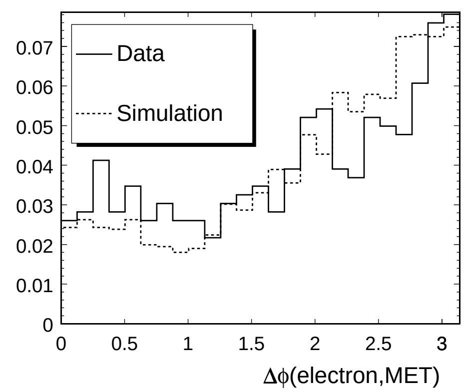

Figure 4.23: *The azimuthal angle between $\not\!\!E_T{}^{corr}$ and the electron candidate direction as measured in the Tight $Z \to ee$ Data and MC Samples for events where $p_T^Z > 15$ GeV.*

GeV for this variable as well.

4.10 Separating Back-to-Back Events from Non-Back-to-Back Events

Events where the taus are back-to-back in the transverse plane are considered separately from those that are not back-to-back. We do this because when the tau candidates are not back-to-back, we may make a cut on $\not\!\!E_l$ and $\not\!\!E_h$, whereas when they are back-to-back, the quantity is undefined. The back-to-back (non-back-to-back) events satisfy $|\sin\Delta\phi_{\tau_l,\tau_h}| < 0.3$ ($|\sin\Delta\phi_{\tau_l,\tau_h}| > 0.3$) [15].

[15] This strange-looking variable, $\sin\Delta\phi$, is chosen because it is the determinant of the system of equations solved to determine the di-tau mass. When $\sin\Delta\phi = 0$, the system cannot be solved.

Cut	No. Events
Total	128,761
Electron ID & $N_{iso} = 0$	58534
Z Rejection	50943
$N_{jets} < 3$	50415
Fiducial Jet	9097
Jet $E_T > 10$ GeV	6478
≥ 1 Tau Seed	1265
$\Delta\phi > 1.5$	1117

Table 4.6: *A summary of the cuts imposed and the number of events remaining in the data sample after each successive cut.*

4.11 Summary

Tables 4.6 and 4.7 summarize the cuts that we impose and the number of events remaining in the sample after each cut.

Table 4.8 summarizes the scale factors and systematic errors contributed by each cut. If the cut is not listed, it is either shown in this note to be modeled sufficiently

$\sin\Delta\phi = 0.3$ corresponds to $\Delta\phi \approx 160°$

	$\|\sin\Delta\phi\| < 0.3$	$\|\sin\Delta\phi\| > 0.3$
Cut	No. Events	No. Events
$\|\sin\Delta\phi\|$	510	607
# Tracks	189	146
Elect. Reject	98	93
$m_\tau < 2$	93	84
# CES	80	72
Jet Width	64	54
$\|Q\| = 1$	48	39
Opp. Sign	39	28
ME>0	NA	8

Table 4.7: *Continued from Table 4.6. A summary of the cuts imposed and the number of events remaining in the data sample after each successive cut.*

well, or we have assumed that to be so. All systematics are assumed to be the same for $A/h \to \tau\tau$ and $Z \to \tau\tau$ except for one: the systematic from modeling the production cross-section at low center-of-mass energy. This will be described in Section 5.1.1 and is called the "low $\sqrt{s}$" systematic in Table 4.8.

Tables 4.9 and 4.10 list the efficiency for $Z \to \tau\tau$ events after each cut is applied in succession, after including all scale factors that need to be applied to the simulation. Tables 4.11 and 4.12 show the same for $A/h \to \tau\tau$ events for the $m_A = 100$ GeV, $\tan\beta = 50$ benchmark point.

Cut	$Z \to \tau\tau$	$Z \to ee$
Cross Section	Systematic: 1.7%	
Electron ID, $N_{iso} = 0$	Scale factor: 0.869 ± 0.016	
Primary Vertex Position	Force agreement	
Trigger	Weight events: systematic $\approx 2\%$	
$\Delta\phi > 1.5, \lvert \sin \Delta\phi \rvert$	p_T^Z(Pythia) reshaped	
Electron Rejection (Hadrons)	Systematic: 2.2%	NA
Electron Rejection (Electrons)	Scale factor: 1.9 ± 0.4 (=$\pm$ 21%)	
$m_\tau < 2$ GeV	CES Energies Corrected	
Jet Width	Systematic: 3.9%	Sufficient agreement

Table 4.8: *Summary of variables where a scale factor or a systematic was necessary, or where we force agreement between data and MC through the acceptance rejection Monte Carlo technique.*

Cut	Efficiency (%)	No. Events
Total $Z \to \tau\tau$		21,900
BR($\tau \to e$)	32.5	7121
$\|\eta_e\| < 1.2$	19.8	1410
Electron ID & $N_{iso} = 0$	35.6	503
L2 Trigger	90.8	457
Z Rejection	93.3	426
$N_{jets} < 3$	97.7	416
Fiducial Jet	35.3	147
Jet $E_T > 10$ GeV	89.4	131
≥ 1 Tau Seed	64.0	84.0
$\Delta\phi > 1.5$	100.0	70.7

Table 4.9: *Efficiency of each cut imposed on $Z \to \tau\tau$ simulated events. We also list the number of $Z \to \tau\tau$ events expected after each cut. Continued in Table 4.10.*

	$\lvert\sin\Delta\phi\rvert < 0.3$		$\lvert\sin\Delta\phi\rvert > 0.3$	
Cut	Eff. (%)	No. Events	Eff. (%)	No. Events
$\lvert\sin\Delta\phi\rvert$	84.1	70.7	15.9	13.4
# Tracks	84.3	59.6	85.9	11.3
Elect. Reject (Had)	95.5	46.0	96.0	8.6
Elect. Reject (Ele)	1.1	0.13	2.0	0.05
$m_\tau < 2$	98.5	45.5	98.6	8.5
# CES	97.0	44.2	96.6	8.2
Jet Width	92.2	40.7	92.5	7.6
$\lvert Q\rvert = 1$	93.1	37.9	92.9	7.1
Opp. Sign	99.8	37.8	100.0	7.1
ME>0	NA		56.8	4.0

Table 4.10: *Continued from Table 4.9. Efficiency of each cut imposed on $A/h \to \tau\tau$ simulated events. We also list the number of $A/h \to \tau\tau$ events expected after each cut.*

Cut	Efficiency (%)	No. Events
Total $A+h \to \tau\tau$		872
$\tau_1 \to e$	32.5	283
$\lvert\eta_e\rvert < 1.2$	26.5	75.1
Tight Electron	44.2	33.2
Electron Trk. Iso.	84.8	28.1
L2 Trigger	91.0	25.6
Z Rejection	90.3	23.1
# jets< 3	96.4	22.3
Fiducial Jet	40.6	9.1
Jet $E_T > 10$ GeV	90.3	8.2
≥ 1 Tau Seed	65.1	5.3
$\Delta\phi > 1.5$	100.0	5.3

Table 4.11: *Efficiency of each cut imposed on $A+h \to \tau\tau$ simulation. We also list the number of $A+h \to \tau\tau$ events expected after each cut. Continued in Table 4.12.*

Cut	$\lvert\sin\Delta\phi\rvert < 0.3$		$\lvert\sin\Delta\phi\rvert > 0.3$	
	Eff. (%)	No. Events	Eff. (%)	No. Events
$\lvert\sin\Delta\phi\rvert$	80.7	4.3	19.4	1.0
# Tracks	82.3	3.5	83.0	0.85
Elect. Reject (Had)	95.2	2.7	95.0	0.64
Elect. Reject (Ele)	1.4	0.01	0.8	0.003
$m_\tau < 2$	98.5	2.7	98.4	0.63
# CES	96.9	2.6	97.7	0.61
Jet Width	92.7	2.4	92.0	0.56
$\lvert Q\rvert = 1$	92.7	2.2	92.8	0.52
Opp. Sign	99.8	2.2	100.0	0.52
ME> 0	NA		58.0	0.30

Table 4.12: *Continued from Table 4.11. Efficiency of each cut imposed on $A/h \to \tau\tau$ simulation. We also list the number of $A/h \to \tau\tau$ events expected after each cut.*

Chapter 5

Event Generation

The Pythia event generator is used as the first stage in simulating signal events and physics-dominated backgrounds. The cross sections and MC samples that are the output of the standard Pythia package need some modifications before the events are passed through the QFL detector simulation. This chapter reviews the modifications made.

5.1 Issues Unique to Supersymmetric Higgs Events

5.1.1 MSSM Cross-Section

A re-summed calculation of the cross sections for direct Higgs production at the Tevatron have been performed by Michael Spira [5]. The program `HIGLU` allows a user to estimate cross sections as a function of mass, $\tan\beta$ and other parameters. Naively, one might think that simply scaling the Pythia cross section to the `HIGLU` cross section would be adequate to estimate the signal rate. However, for a given Higgs mass `HIGLU` gives the *on-shell* cross section only. A Supersymmetric Higgs produced at large $\tan\beta$ has a significant width and a tail at low values of $\sqrt{\hat{s}}$ (see Figure 5.1). Therefore, scaling the Pythia cross section to the `HIGLU` one would underestimate the cross section because the off-shell events would not be accounted for.

The total cross section is therefore estimated through the following procedure [50].

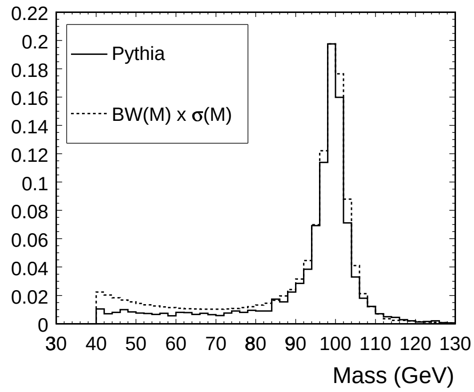

Figure 5.1: *The figure shows the expected mass distribution of Higgs bosons produced directly at the Tevatron. We compare the output of Pythia 6.203 with that obtained from the method introduced in this thesis: folding in a simple Breit-Wigner distribution with the mass-dependent cross section calculation.*

First, using the `HIGLU` program we retrieve the on-shell cross section as a function of mass in bins 1 GeV wide. Next, we construct a simple Breit-Wigner shape:

$$BW(Q^2) = \frac{M_{A/h}\Gamma(Q^2)/\pi}{(Q^2 - M_{A/h}^2)^2 + M_{A/h}^2\Gamma(Q^2)^2}. \tag{5.1}$$

Here, Q^2 is the momentum transfer of the event. Since the Higgs is produced directly, $Q^2 = s$ where $\sqrt{s}$ is the center-of-mass energy of the collision. The width is chosen to be proportional to Q^2:

$$\Gamma(Q^2) = \Gamma(M_{A/h})\frac{Q^2}{M_{A/h}^2}. \tag{5.2}$$

$\Gamma(M_{A/h})$ is taken to be the Higgs width from Pythia at the parameter space point of interest. Then, the mass-dependent cross section is folded into the Breit-Wigner shape. For a given bin in Q^2, the cross section is given by:

$$\sigma_{\texttt{HIGLU}}(Q_0^2) \times \left(\arctan \frac{Q_+^2 - M_H^2}{M_H \Gamma(Q^2)} - \arctan \frac{Q_-^2 - M_H^2}{M_H \Gamma(Q^2)} \right) \tag{5.3}$$

where Q_+ (Q_-) is the upper (lower) edge of the mass bin. $\Gamma(Q^2 = M_H)$ is the Pythia width for a given m_A and $\tan\beta$. We sum in 1 GeV bins from $Q^2 = (40 GeV)^2$ to $Q^2 = (200 GeV)^2$. For $m_A = 100$ GeV at $\tan\beta = 50$, the MSSM cross-section for $A + h$ production is 122.48 pb.

There is a significant uncertainty in the rate of Higgs production in the region of low $\sqrt{\hat{s}}$. The low tail seen in Figure 5.1 originates from a steeply falling cross section folded in with an increase in parton luminosities at small momentum transfer, folded in with a broad Higgs width. When we use the method outlined above to obtain a Q^2 dependent cross section, the size of the tail is between those from Pythia and Isajet [43]. We take the systematic error on the Higgs cross section to be the percentage difference between the total efficiency of all of our cuts when two different Q^2 dependent cross sections are used: first, the one from the standard Pythia output and second, the one obtained from Equations 5.1 and 5.3. At $m_A = 100, \tan\beta = 50$, this uncertainty is 2%. At higher mass and higher $\tan\beta$, this systematic can become quite significant. At $m_A = 140$, $\tan\beta = 80$ the systematic is 30%.

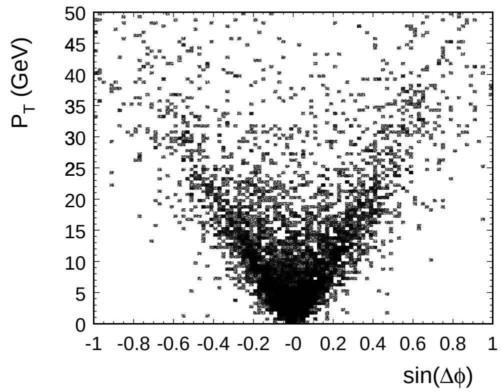

Figure 5.2: *Higgs P_T plotted against the azimuthal angle between the tau daughters.*

5.1.2 Transverse Momentum Distributions

It is important to properly model the boson p_T distributions in Higgs and Z events, particularly in the non-back-to-back region where the mass technique is used. As seen in Figure 5.2, the p_T distribution is strongly correlated with the $\Delta\phi$ distribution, which affects the mass resolution and the relative rates of back-to-back and non-back-to-back events. Figure 5.3 shows the p_T distribution of the A ($m_A = 100$ GeV) after the $|\sin\Delta\phi| > 0.3$ cut is imposed and we see that a $|\sin\Delta\phi| > 0.3$ cut on the tau daughters of the Higgs is approximately equivalent to a cut of $p_T > 15$ GeV imposed on the parent Higgs bosons.

In the high-$\tan\beta$ region of parameter space relevant to this thesis, the direct-production process occurs predominantly through a triangular bottom quark loop as in Figure 2.4 (in the Standard Model, the process occurs predominantly through a

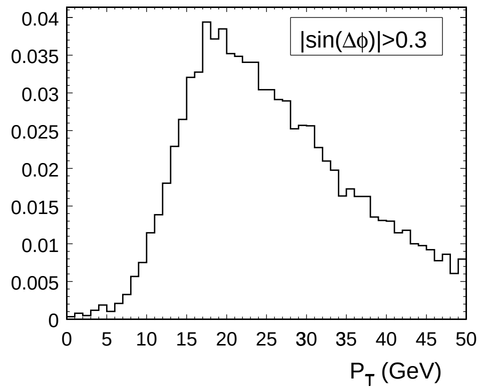

Figure 5.3: *P_T spectrum of directly produced Higgs bosons after a $|\sin\Delta\phi| > 0.3$ cut has been imposed.*

top quark loop). The p_T distribution of the Higgs bosons from the events generated in Pythia are calculated assuming the process occurs through a top quark loop, even if the couplings have been set to reflect the enhanced couplings to bottom-type fermions in the high-$\tan\beta$ region [44]. We correct for this as much as possible by using a program written by Keith Ellis and Ian Hinchliffe [38], which performs a perturbative calculation for the differential cross section to order α_s^3 with a variable quark mass in the triangular loop. The perturbative calculation is valid in the region $p_T^{Higgs} \gtrsim$ 15 GeV. As has been pointed out, this cut is nearly equivalent to the requirement $|\sin\Delta\phi| > 0.3$. Using the acceptance rejection Monte-Carlo method, the Higgs p_T distributions in the region $p_T^{Higgs} > 15$ GeV are forced to match the expectation for a 5 GeV quark in the loop from the Ellis-Hinchliffe program. Then, having set the overall cross section using the method outlined in Section 5.1.1, and since the p_T

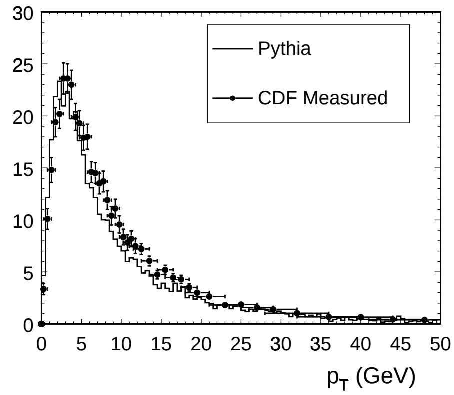

Figure 5.4: *P_T spectrum of Z bosons as measured by CDF compared with that from Pythia.*

distribution is strongly correlated with the $\Delta\phi$ distribution, this gives us the proper efficiency for the $|\sin \Delta\phi|$ cut.

5.2 Z Production

The p_T distribution of the Z bosons from $Z/\gamma^* \to ee$ events has been measured by CDF [45] in the region 66 GeV $< M_{ee} <$ 166 GeV. In Figure 5.4, we compare the measured Z p_T distributions to that from Z production from Pythia 6.203. Z bosons from Pythia tend to be too soft. Therefore, using the acceptance rejection Monte Carlo method on both the $Z/\gamma^* \to \tau\tau$ and $Z/\gamma^* \to ee$ samples, we force agreement between the MC events and the measured spectrum. Only events that lie in the measured region 66 GeV $< M_{ee} <$ 166 GeV are subject to rejection since that is the region where the p_T distribution was measured. Those outside the window are left as they are. Figure 5.4 also shows the Z p_T distributions from Pythia after agreement has been forced. This correction makes a significant difference in the relative rates of back-to-back and non-back-to-back events. Before the correction, 20% of the Z events from Pythia are in the non-back-to-back region (here, defined by $p_T^Z > 15$ GeV). After the correction, 26% of the events are in the non-back-to-back region.

5.2.1 $Z/\gamma^* \rightarrow \tau\tau$

CDF reports the cross section for $Z/\gamma^* \rightarrow ee$ in the range 66 $\texttt{GeV} < M_{ee} < 116$ GeV to be (248 ± 11 pb) [45]. We assume that the cross section for $Z/\gamma^* \rightarrow \tau\tau$ is identical and scale the generated $Z \rightarrow \tau\tau$ sample to this cross section. Since we generate $Z \rightarrow \tau\tau$ events with $\hat{s} > 40$ GeV, we need to account for the cross section from events beyond the measured range (as was done for the generated Higgs events). The cross-section that we use is:

$$\sigma(\sqrt{\hat{s}} > 40\ \texttt{GeV}) = \sigma(\texttt{CDF}, 66 < M_{ee} < 116\ \texttt{GeV}) \times \frac{\sigma(\texttt{Pythia}, \sqrt{\hat{s}} > 40\ \texttt{GeV})}{\sigma(\texttt{Pythia}, 66 < \sqrt{\hat{s}} < 116\ \texttt{GeV})} \tag{5.4}$$

where $\sigma(\texttt{CDF}, 66 < M_{ee} < 116\ \texttt{GeV})$ is the CDF measured Z cross section. $\sigma(\texttt{Pythia}, R)$ is the cross section from the standard Pythia output in the range R.

Since the CDF measured cross section is used to scale the Z MC samples to the expected rate at CDF, the systematic error on that measurement gives us an error on the Z cross sections used. The CDF measurement reports a 4.4% systematic error on the cross section which includes a 4.1% systematic from the error on the luminosity. Since this luminosity systematic is accounted for separately in this thesis, we factor it out so not to over-count. Then, the systematic error on the cross section is $\sqrt{(4.4\%)^2 - (4.1\%)^2} = 1.7\%$ for each of $Z/\gamma^* \to \tau\tau$ and $Z/\gamma^* \to ee$.

5.2.2 $Z/\gamma^* \to ee$

Since the $Z/\gamma^* \to ee$ sample was generated with a $\sqrt{\hat{s}} > 20$ cut, the cross section that we use for this process is similar to that described in Section 5.2.1 with $\sqrt{\hat{s}} > 40$ GeV replaced with $\sqrt{\hat{s}} > 20$ GeV:

$$\sigma(\sqrt{\hat{s}} > 20\ \texttt{GeV}) = \sigma(\texttt{CDF}, 66 < M_{ee} < 116\ \texttt{GeV}) \times \frac{\sigma(\texttt{Pythia}, \sqrt{\hat{s}} > 20\ \texttt{GeV})}{\sigma(\texttt{Pythia}, 66 < \sqrt{\hat{s}} < 116\ \texttt{GeV})}. \tag{5.5}$$

5.3 Tau Daughters

When a Z or Higgs boson decays to two taus, the taus carry information about the spin of their parent. We use `TAUOLA` [42], a software module, to properly treat the effect of the parent boson polarization on the tau lepton kinematics. The effect is that Higgs (spin 0) events tend to produce one tau with hard (high-p_T) visible decay products and one with soft visible decay products. Z events tend to produce tau pairs where the visible decay products from each are either both hard or both soft.

Chapter 6

Fake Backgrounds

The backgrounds to $A/h \to \tau\tau$ signal at CDF may be divided into two categories: physics-dominated backgrounds and detector-dominated backgrounds. The former include $Z \to \tau\tau$ and $Z/\gamma \to ee$. The predicted rates for these backgrounds have been described in Chapter 4. Detector-dominated backgrounds come from events where leptons are faked by QCD jets. Either the electron candidate or the hadronic tau candidate, or both, may be faked by a jet. This can occur in W+jets events or QCD events. For example, in some QCD events, a real electron from a conversion pair may be identified as the first tau candidate while a recoil jet fakes a hadronic tau. From $W \to e\nu$+jets events, we may also observe a real electron and a fake hadronic tau from a recoil jet. Some QCD events may contain both a fake tau and a fake electron. The only background which could potentially give a real hadronic tau and a fake electron is $W \to \tau\nu$+jets, which we have shown from MC studies to be insignificant. Therefore detector-dominated backgrounds are encompassed by the following three categories: events containing a conversion pair and a recoil jet, $W \to e\nu$+jets events, and events containing a jet that fakes an electron. All of these contain a fake hadronic tau.

Estimating the rate of each of these sources individually is difficult for two reasons. First, we are not confident in the simulation of the tau ID variables for jets, so one cannot just generate each process and count how many events pass the analysis cuts. Second, we have attempted to use data control samples to estimate each background separately and have found that we do not have enough statistics in any of the control samples to measure the efficiency of all of the cuts applied together. Instead, we estimate the rate of all fake tau contributions combined. We estimate the fake contribution from the same data sample in which we perform our analysis. We do this by folding in tau fake rates measured from separate control samples with jet multiplicities observed in the data sample at a stage in the analysis where the data is expected to be dominated by fake tau backgrounds.

6.1 Control Samples

We use five different control samples from CDF data to measure the rate at which a jet fakes a hadronic tau by passing the tau identification cuts for this analysis. The selection of these control samples and the selection of the candidate jets for these studies are described in Appendix B. They are called: the Conversion Sample, the $W \to e\nu$+jets Sample, the $W \to \mu\nu$+jets Sample, the Jet 20 Sample and the Jet50 Sample. These control samples are classified as lepton samples (Conversion Sample, $W \to e\nu$+jets Sample, the $W \to \mu\nu$+jets) and jet samples (Jet 20 Sample and the Jet50 Sample).

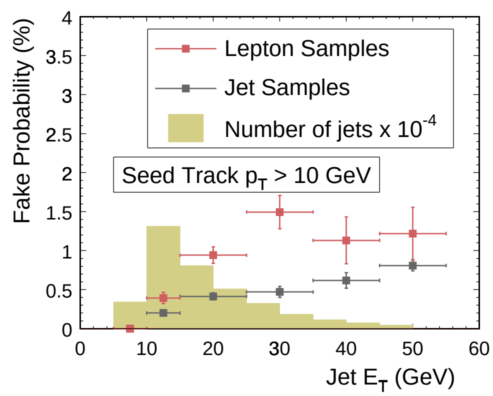

Figure 6.1: *Hadronic tau fake rates as measured in the lepton control samples compared with that measured in the jet control samples.*

6.2 Hadronic Tau Fake Rates

A fake rate is defined as the probability that a jet passes the hadronic tau identification requirements as described in Section 4.4. The only cut that is not included in the fake rate measurements is the opposite sign requirement. The efficiency of the opposite sign cut is measured separately. For all data control samples, we measure the fake rates in bins defined by the E_T of the jet associated with the tau candidate. We find that the fake rates measured from the lepton samples are approximately a factor of 2 higher than from the jet samples. The reason for this difference is not understood, so it is a systematic for the analysis. Figure 6.1 shows the fake rates measured from all three lepton samples combined and from both jet samples combined. The reason for the difference is unknown. We measure fake rates less than about 1% from the Jet20 and Jet50 samples, which are as good as previous Run 1 analyses [48]. The histogram in Figure 6.1 shows the E_T distribution of jets in the data sample just before tau identification cuts are applied. The fake rates are folded into this E_T distribution to predict the rate of fake tau background. Since the analysis is performed in a lepton sample, we use the fake rates measured from the lepton samples for this prediction. The discrepancy between the lepton samples and the jet samples is a systematic error as described below.

6.2.1 Systematic on Tau Fake Rates

Lepton vs. Jet Samples

The difference between the number of fakes predicted from the lepton sample fake rates and the number of fakes predicted using the jet sample fake rates as a systematic. This systematic is 57.1% and is the dominant systematic for this analysis.

Opposite Sign Requirement

We would naively expect fake taus to be opposite sign from the Tight Electron 50% of the time. From the lepton samples, we measure how often the fakes are opposite sign from the high-p_T lepton in the event. Here are the efficiencies measured in the different samples:

- Conversion Sample: $145/292 = 49.7 \pm 2.4\%$
- W$\rightarrow e\nu$+jets: $58/93 = 62.4 \pm 3.9\%$
- W$\rightarrow \mu\nu$+jets: $103/147 = 70.1 \pm 2.9\%$

The rate of opposite-sign fakes is consistent with 50% in the Conversion Sample, but the W+jets events tend to be opposite-sign. The combined efficiency of this cut from W+jets events is $67.1 \pm 3.0\%$. The difference between this and 50% is an additional systematic on the rate of fake taus. This systematic is $(67.1 - 50)/50 = 34.2\%$.

6.3 Applying Fake Rates to the Data

In order to estimate the number of fake taus expected to pass all of our cuts, we fold in our measured fake rates with the E_T spectrum of jets in the data sample, having applied all of our analysis cuts *except*:

- Tau ID Cuts
- Opposite Sign Requirement
- $\not{E}_{\tau_1,\tau_2} > 0$

There are 6478 events that pass these cuts and which contain at least one jet passing the fiducial cuts. We apply our measured fake rates to 6972 jets from these events. For each jet, we give it a weight equal to the fake rate measured for its E_T. For each event, the probability that an event contains a fake is the opposite of the probability that no jet fakes a tau. We expect 21.0 ± 12.1 back-to-back and 29.8 ± 16.8 non-back-to-back for a total of 50.8 ± 29.0 fakes before the remaining cuts are applied. We expect these events to be contaminated with 1.5 $Z \to \tau\tau$ and 3.2 $Z \to ee$ events.

The next cut to be applied is the opposite sign requirement. Taking the efficiency to be 50% and including the systematic error from this cut, we expect 10.5 ± 6.0 back-to-back and 14.9 ± 8.5 non-back-to-back for a total of 25.4 ± 16.9 fakes at this stage. We expect 0.6 (0.1) back-to-back (non-back-to-back) $Z \to \tau\tau$ and 1.3 (0.3) back-to-back (non-back-to-back) $Z \to ee$ events to contaminate this estimation.

The final cut is the $\not{E}_{\tau_1,\tau_2} > 0$ cut applied to the non-back-to-back events only. This is measured from the same background-dominated sample, but one of the jets in the event is required to contain a seed with $p_T > 10$ GeV, as in the analysis. 80/606 non-back-to-back events pass the $\not{E}_{\tau_1,\tau_2} > 0$ cut. The numerator is expected to contain 8.1 $Z \to \tau\tau$ events and 11.6 $Z \to ee$ events. The denominator is expected to contain 13.3 $Z \to \tau\tau$ events and 45.9 $Z \to ee$ events. After subtracting out this contamination, the efficiency for this cut on fakes is 11.0%. This brings the number of non-back-to-back fake events predicted to 1.5. Added to the back-to-back events, we expect $1.5 + 8.6 = 10.1$ events containing a fake hadronic tau to pass the analysis cuts.

Chapter 7

Optimizing Sensitivity

7.1 Introduction

Many of the cuts imposed in the Run 1 $A/h \rightarrow \tau\tau$ analysis were initially chosen as a "best guess" and then tuned to optimize our sensitivity to $A/h \rightarrow \tau\tau$ in the MSSM.

The cuts on six different variables are optimized. These variables have already been described in Chapter 4, with the exception of two. One is the charge deposited in the CPR (this detector component is described in Section 3) and the other is the transverse mass $M_T(e, \not{E}_T)^{uncorr}$, the mass deduced from the transverse components of the electron candidate and the missing energy in the event. We order the six variables "inside out" – beginning with cuts on the tau candidates and moving out to event-wide cuts such as $\not{E}_T$. The 6 cuts listed in order that they are tuned are: E_T of the second tau, p_T of the seed track, the CPR charge deposited by the electron candidate, ξ (the electron rejection variable on the second tau), ${\not{E}_T}^{uncorr}$, and M_T. We begin with all cuts at the best guess values, then optimize the E_T cut, set it to its optimal value, then optimize the p_T cut, set it to its optimal value, and so on.

We perform the optimization for two parameter space points: $m_A = 100, \tan\beta = 50$ and $m_A = 140, \tan\beta = 50$. We pick $m_A = 100, \tan\beta = 50$ because it is the highest $\tan\beta$ at the lowest mass not excluded by the previous $b\bar{b}b\bar{b}$ analysis (see Figure 2.6). The second point, $m_A = 140, \tan\beta = 50$, was chosen because it is approximately 2

RMS away from the first point in the di-tau mass variable.

We perform the optimization for a counting experiment including both back-to-back and non-back-to-back events. We then select the non-back-to-back events select and optimize the sensitivity again, this time binning the events in the di-tau mass variable.

The quantity that we optimize is the confidence level at which we can exclude the MSSM cross section for A/h production. We use a Bayesian likelihood (described in Appendix E) to get the expected limit, setting the hypothetical observed number of events equal to the expected number. When only the non-back-to-back events are considered, the likelihood is binned in 14 bins in the di-tau mass variable from 60 GeV to 200 GeV.

We first optimize the cuts considering statistical errors only. Then, the largest systematic errors are targeted and we reduce them by removing or tightening the cuts which contribute the most to those errors.

As a rule of thumb, we move 10 steps between the cut that is 100% efficient for signal and the cut that is 50% efficient for signal. If the confidence level plateaus beyond some cut value, then we pick the loosest cut along the plateau.

	No. events (CL) non-BTB + BTB	No. events (CL) non-BTB
$Z \to \tau\tau$	16.5	2.13
Fakes	5.4	0.88
$Z \to ee$	< 0.1	< 0.1
$m_A = 100, \tan\beta = 50$	1.1 (16.5%)	0.15 (5.2%,5.3%)
$m_A = 140, \tan\beta = 50$	0.25 (3.8%)	0.033 (1.1%,1.5%)

Table 7.1: *Numbers of events predicted before the cuts are optimized.*

7.2 Optimization Considering Statistical Errors Only

The best-guess cuts that we start with are: $E_T > 10$ GeV, $p_T > 5$ GeV, CPR>2 (arbitrary units for this purpose), $\xi > 0.15$, ${\not\!\!E_T}^{uncorr} > 10$ GeV and $M_T < 60$ GeV. With these cuts in place, we predict the numbers of events listed in Table 7.1. We also show the confidence levels at which one can exclude the MSSM Higgs cross section from a counting experiment using both back-to-back and non-back-to-back events, and then from a likelihood binned in di-tau mass using non-back-to-back events only (actually, for the latter we show both the binned and unbinned likelihood so that we may see how much is gained from the di-tau mass reconstruction).

After the optimization is performed considering statistical errors only, the cuts on the six variable are now: $E_T > 7$ GeV, $p_T > 5$ GeV, no CPR cut, no electron rejection, $\not{E}_T{}^{uncorr} > 5$ GeV and no M_T cut. The optimization gave a similar result for both the (BTB + non-BTB) counting experiment and the (non-BTB) binned likelihood for both parameter space points tested, so we use the same cuts for all four cases. Table 7.2 shows the predicted numbers of events and confidence levels after optimizing the cuts considering statistical errors only. We see a 50% improvement in the confidence levels for excluding the MSSM Higgs compared to those before the optimization. However, we now allow more background events to pass our cuts. The fake backgrounds in particular introduce large systematics errors which we address in the next section.

7.3 Reducing Systematics

Having tuned the cuts to maximize sensitivity taking into account statistical errors only, we have allowed more background events to pass our cuts. This means we have increased our systematic errors. Now, we start with the set of cuts tuned for statistical errors only and see what we can do to reduce the largest systematics. The results are summarized in Table 7.3. Here the quantity we are optimizing is the upper limit on

	Counting Exp. non-BTB + BTB	Non-Back-to-Back Region
$Z \to \tau\tau$	63.3	7.4
Fakes	27.4	4.3
$Z \to ee$	56.8	5.2
$m_A = 100, \tan\beta = 50$	3.9 (24.3%)	0.57 (9.6%,10.6%)
$m_A = 140, \tan\beta = 50$	0.8 (4.7%)	0.093 (1.5%,2.4%)

Table 7.2: *Numbers of events predicted after the cuts are optimized for statistical significance only.*

the cross section for $A/h \to \tau\tau$ in the MSSM at the parameter point $m_A = 100$ GeV and $\tan\beta = 50$.

For physics-dominated backgrounds ($Z \to \tau\tau$ and $Z \to ee$) and signal, the systematics are predominantly from deficiencies in the simulation and have been summarized in Table 4.8. The systematics associated with fake backgrounds have been summarized in Sections 6.2.1.

We start by moving the E_T cut up from 7 GeV to 10 GeV, the latter being more standard for CDF. This is also more of a compromise between the different E_T cuts which were shown to be optimal for the two different masses.

The first line of Table 7.3 shows the upper limit on the cross section at 95% CL for our benchmark parameter space point, $m_A = 100, \tan\beta = 50$ using the cuts that were optimized based on statistical errors and having moved the E_T cut to 10 GeV. We also list the systematic error on each background type, expressed in terms of numbers of events. This gives us an idea of which background is the largest contributer to the systematic error. Here, the largest contributer is the fake tau background.

To reduce the fake tau background, we could raise the seed p_T cut. We adopt the p_T cut used in [48]: $p_T > 10$ GeV. The second line in the table shows the effect this has on the limits. The limit that takes systematics errors into account remains about the same, but the number of fakes has been cut by a factor of 2, and we consider this to be a better situation, so we keep the p_T cut at 10.

The next largest systematic comes from $Z \to ee$, and a big contribution to the systematic on $Z \to ee$ comes from the error from modeling the $\not{E}_T{}^{uncorr}$ below 5 GeV. We try removing the straight cut on $\not{E}_T{}^{uncorr}$, and this removes the systematic associated with it. This did improve the limit, as shown on the third line of Table 7.3.

Removing the $\not{E}_T{}^{uncorr}$ cut made $Z \to ee$ the largest background (at this stage, we have 88.2 $Z \to ee$, 55.1 $Z \to \tau\tau$ and 14.1 fakes). Therefore, we reinstate the $\xi > 0.15$ electron rejection requirement and find that this improves the limit to 1100 pb.

We could have also reduced the $Z \to ee$ background by increasing the $\not{E}_T{}^{uncorr}$

cut. We try increasing it to the initial best-guess value of 10 GeV. See the second-to-last line of the table. Due to a decrease in the efficiency for Higgs events with this higher ${\not}E_T{}^{uncorr}$ cut, the limit based on statistical errors is degraded. Here we do not calculate the limit with systematics included because it could only be worse than the one based on statistical errors.

The last thing that we try is to replace the ${\not}E_{l,h} > 0$ cut in the non-back-to-back region with an M_T cut, $M_T < 60$ GeV, which was our best-guess cut before tuning See the last line of Table 7.3. This is motivated by the fact that the ${\not}E_{l,h} > 0$ cut is only $\approx 55\%$ efficient for Higgs events, and so a different method of background removal in the non-back-to-back region might be better. The $M_T < 60$ GeV cut targets the removal of W+jets events. We find that the M_T cut does not effectively reject background largely because W+jets is not a large enough contribution to the fake background. The ${\not}E_{l,h} > 0$ cut reduces fakes by a factor of 10 in the non-back-to-back region, and the $M_T < 60$ cut only reduces the background by a factor of 2.

Therefore, the set of cuts on the forth line of Table 7.3 gives the best upper limit on MSSM cross section. By targeting the largest systematics, we have reduced the limit by 30%. Thus, the final cuts for the six variable included in the optimization are:

	95% CL	95% CL	Error (No.events)[1]		
	w/o syst.	w/ syst.	$Z \to \tau\tau$	$Z \to ee$	Fakes
$p_T > 5$ GeV, $E_T > 10$ GeV $\not{E}_T{}^{uncorr} > 5$ GeV	745	1490	3.2	6.9	16.6
$p_T > 10$ GeV, $E_T > 10$ GeV $\not{E}_T{}^{uncorr} > 5$ GeV	952	1485	3.2	5.7	6.8
$p_T > 10$ GeV, $E_T > 10$ GeV	922	1310	3.1	4.5	8.6
$\mathbf{p_T > 10}$ **GeV,** $\mathbf{E_T > 10}$ **GeV** $\xi > \mathbf{0.15}$	**766**	**1100**	**3.0**	**0.2**	**8.1**
$p_T > 10$ GeV, $E_T > 10$ GeV $\not{E}_T{}^{uncorr} > 10$	1050				
$p_T > 10$ GeV, $E_T > 10$ GeV $\xi > 0.15$ Replace $ME > 0$ w/ $M_T < 60$	761	1270	2.5	0.1	11.3

Table 7.3: *Predicted 95% confidence levels (in pb) with and without systematics included, as cuts tuned on statistics only were modified to reduce systematics.*

	non-BTB + BTB	non-BTB
$Z \to \tau\tau$	42.4	4.1
Fakes	10.1	1.5
$Z \to ee$	0.6	0.05
$m_A = 100, \tan\beta = 50$	2.5	0.30
$m_A = 140, \tan\beta = 50$	0.51	0.06

Table 7.4: *Final predictions for backgrounds and signal with the final cuts for the analysis.*

- $E_T > 10$ GeV
- $p_T > 10$ GeV
- No CPR Cut
- $\xi > 0.15$
- No $\not{E}_T{}^{uncorr}$ Cut
- No M_T Cut

Thus, Table 7.4 shows the final predictions for backgrounds and signal having optimized the six variables.

Chapter 8

Results

This chapter summarizes the results of the search. First, we summarize the systematic errors for the backgrounds and signal. Next, we show the track multiplicity distributions for the hadronic tau candidates since an excess of 1-track and 3-track candidates is a signature for taus. We then set limits on direct A/h production in the MSSM based on a counting experiment using events in both the back-to-back and non-back-to-back regions. Finally, we show the di-tau mass distribution for the non-back-to-back events only, and compare the limits from a binned likelihood in the di-tau mass variable with the limits from the counting experiment.

8.1 Systematics

In Table 8.1, we summarize the systematics on the backgrounds and signal. $Z \to ee$ is not included in the table because the expected rate is based on a low number of background events. We expect 0.6 ± 0.3 $Z \to ee$ events in the counting experiment. The one systematic on Higgs events that varies significantly with mass is the error on the cross section due to the low $\sqrt{s}$ tail. Here are the systematic errors for each parameter space point considered in this note: $m_A = 100, \tan\beta = 50$, 0.5%; $m_A = 110, \tan\beta = 50$, 2.5%; $m_A = 120, \tan\beta = 50$, 3.5%, $m_A = 140, \tan\beta = 50$, 7.2%; $m_A = 140, \tan\beta = 80$, 21.3%. The systematics that come from simulating $A/h \to \tau\tau$,

$Z \to \tau\tau$, and $Z \to ee$ with QFL are described in Chapter 4. The systematics on the fake tau background are described in Section 6.2.1. The error on the luminosity comes from [41]. We obtain the jet energy scale systematic by moving energies of all of the jets (except electron jets) up and down by 5%. At the bottom of Table 8.1, we list the total systematic error for each background in %, and also in number of events (let us be clear that this is *not* the number of each background expected, but the error on the background). The error expressed in number of events is the true measure of which systematic dominates, which is clearly fake taus.

8.2 Track Multiplicity Plots

We plot the track multiplicity of the tau candidates in the events which pass our cuts because hadronic taus appear predominantly in the 1-track and 3-track bins. This plot allows us to compare the tau, fake composition in the data with the background estimates. We would also like to demonstrate that we do observe the irreducible background, $Z \to \tau\tau$.

Before we look at the track multiplicity plot, we impose all of the analysis cuts *except* the following cuts:

- $|\sum Q_i| = 1$

Systematic	$A/h \to \tau\tau$ ($m_A = 100, \tan\beta = 50$)	$Z \to \tau\tau$	Fakes
Luminosity	4.1	4.1	–
Cross section	0.5	1.7	–
Electron ID	1.8	1.8	–
Sample dependence of fake rates	–	–	57.1
Opposite sign	–	–	34.2
Jet Width	2.3	2.3	–
Jet Energy Scale	1.0	1.2	–
Trigger Eff.	1.6	1.7	–
Electron Rej.	4.1	4.1	–
Total Error (%)	7.0	7.0	66.6
Total Error (No. Events)		3.0	6.7

Table 8.1: *Summary of systematics on counting experiment for final cuts. All systematics are quoted as a percentage of the total number of events observed after all cuts are applied, except for the last line where they are quoted in terms of number of events. $Z \to ee$ is not included in the table because it is based on a low number of MC events. See the text.*

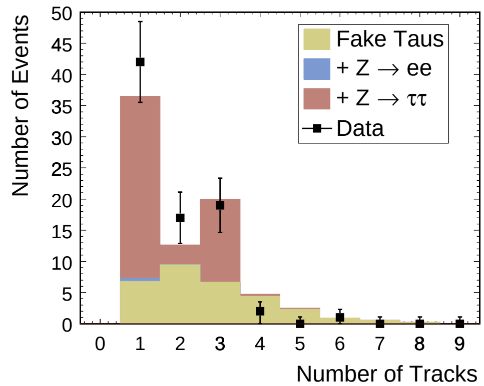

Figure 8.1: *Track multiplicity distribution for the counting experiment, but* without *the* $|Q| = 1$*, opposite sign, and* $N_{cone}^{trks} < 4$ *requirements.*

- $N_{cone}^{trks} < 4$
- Opposite sign requirement

Figure 8.1 shows the number of tracks in the 0.175 cone around the tau seed in the hadronic tau candidate in the event. We expect 78.2 events to appear in this plot and we observe 81. Remember that the events that pass all of our analysis cuts are a subset of the events that appear in Figure 8.1. Also remember that the events in Figure 8.1 do not have the three cuts listed above imposed, so the fake contribution is higher here than after all cuts are imposed.

Table 8.2 lists the number of events expected of each background type in Figure 8.1, and after the subsequent cuts are imposed. The data and the prediction show good agreement at each stage. Of the 47 final observed events, 35 are 1-track

	$Z \to \tau\tau$	$Z \to ee$	Fake Taus	Total	Obs.
# Tracks Plot	46.1	0.56	31.5	78.2	81
$\|Q\| = 1$,# Tracks< 4	42.4	0.56	20.2	63.1	61
Opposite Sign	42.4	0.56	10.1	53.1	47

Table 8.2: *Number of each background type expected, in the track multiplicity plot and after subsequent cuts are imposed, compared with the number observed.*

and 12 are 3-track. The final three cuts reduce the fake background in these two bins by a factor of 2 compared to that shown in Figure 8.1, and leaves the $Z \to \tau\tau$ background in those bins virtually unchanged.

8.2.1 Non-Back-to-Back Events Only

Figure 8.2 shows the track multiplicity distribution for the non-back-to-back events only (since we will be performing the di-tau mass reconstruction on these events). These events have passed the $\not{E}_{l,h} > 0$ requirement but the $|Q| = 1$, opposite sign, and $N^{trks}_{cone} < 4$ requirements have not been imposed. We expect 9.2 events to appear in the plot and we observe 15.

Table 8.3 lists the number of events expected of each background type in Figure 8.2 including non-back-to-back events only. We also show the expectation compared to

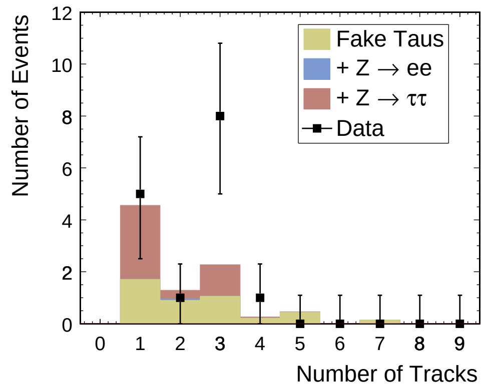

Figure 8.2: *Track multiplicity distribution for the non-back-to-back events* with *the* $\not\!\!E_{l,h} > 0$ *requirement, but* without *the* $N_{cone}^{trks} < 4$, $|Q| = 1$ *and opposite sign requirements.*

the observed after the subsequent cuts are imposed. The final 8 events contain 5 1-track events and 3 3-track events.

8.3 Limits

We use a Bayesian method to set limits. The method is outlined in Appendix E. For each point in parameter space, we set a limit on the cross section at 95% confidence level.

8.3.1 Benchmark Parameter Space Point

Considering statistical errors only, the expected 95% upper limit is 16.0 signal events. For $m_A = 100, \tan\beta = 50$ in the MSSM, this corresponds to 766 pb. Once

	$Z \to \tau\tau$	$Z \to ee$	Fake Taus	Total	Obs.
# Tracks Plot	4.4	0.05	4.5	9.2	15
$\lvert Q\rvert = 1$,# Tracks< 4	4.1	0.05	3.0	7.1	13
Opposite Sign	4.1	0.05	1.5	5.6	8

Table 8.3: *Number of each background type expected, in the track multiplicity plot and after subsequent cuts are imposed, compared with the number observed. Only non-back-to-back events are included.*

we include the systematics in Table 8.1, the expected limit is 23.0 signal events, corresponding to 1100 pb for the same parameter space point. Since we observed slightly fewer events than we expected, the observed limits are better than expected. The observed 95% upper limit would be 579 pb if we were to only consider statistical errors. The limit is 891 pb once systematics are included. Figure 8.3 shows the likelihood distribution based on the number of events observed with and without systematic errors included, showing the point at which the integral reaches 95% for each, in terms of the number of signal events.

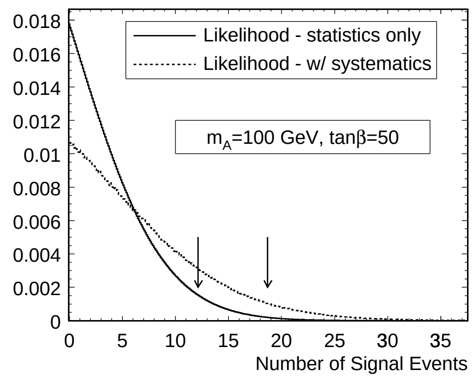

Figure 8.3: *Likelihood distribution for the counting experiment at* $m_A = 100$*,* $\tan\beta = 50$*, considering statistical errors only (solid) and after systematics smear the distribution (dashed). The arrows point to where the integral under each curve reaches 0.95.*

8.3.2 Counting Experiment

Limit vs. Mass

Table 8.4 shows the predicted and observed upper limits on the cross section for A/h production in the MSSM as a function of m_A at $\tan\beta = 50$. The limits on the cross section do improve with increasing mass since the efficiency improves, but we are less sensitive to the MSSM theory at higher mass due to the steeply falling predicted cross section.

Mass (GeV)	Cross Section pb	Eff. %	95% CL stat. only Exp.	95% CL w/ syst. Exp.	95% CL stat. only Obs.	95% CL w/ syst. Obs.
100	122	0.78	766	1100	579	891
110	64.3	0.91	656	943	496	767
120	44.1	0.97	615	887	465	718
140	17.8	1.1	555	812	420	660

Table 8.4: 95% CL limits vs. m_A for $\tan\beta = 50$.

Limit vs. $\tan\beta$

Since the cross section for producing A/h in the MSSM scales with $(\tan\beta)^2$, it is tempting to scale the sensitivity with $1/(\tan\beta)^2$. However, this would be a mistake. The Higgs width scales with $(\tan\beta)^2$, and the tail at low $\sqrt{s}$ also becomes more prominent with increasing $\tan\beta$, increasing the systematic error due to the uncertainty in the cross section in this region. At $m_A = 140$ and $\tan\beta = 80$, the error on the Higgs efficiency due to this low mass tail is 20%, compared to 7.2% at $m_A = 140, \tan\beta = 50$. Also, both effects bring down the efficiency at higher $\tan\beta$: at $m_A = 140$ and $\tan\beta = 80$, the efficiency is similar to the efficiency at a lower mass point: $m_A = 110, \tan\beta = 50$. Table 8.5 shows the limits for two different values of

$\tan\beta$	Cross Section pb	Eff. %	95% CL stat. only Exp.	95% CL w/ syst. Exp.	95%CL stat. only Obs.	95%CL w/ syst. Obs.
50	17.8	1.1	555	812	420	660
80	65.9	0.85	697	1210	527	981

Table 8.5: *95% CL limits vs.* $\tan\beta$ *for* $m_A = 140$ *GeV. All confidence levels are quoted in pb. The efficiencies shown do not include branching ratios.*

$\tan\beta$ for $m_A = 140$ GeV.

8.3.3 Di-tau Mass Reconstruction

In the non-back-to-back region, after all cuts are applied, we expect 5.6 events and observe 8. Figure 8.4 shows the di-tau mass distribution for these 8 events compared with the expectation. In this region, limits come from a binned likelihood, with 14 bins between 60 GeV and 140 GeV in di-tau mass.

Limit vs. Mass

Table 8.6 shows the upper limits on the MSSM cross section obtained from the binned likelihood for four different values of m_A for $\tan\beta = 50$. Again, the limits on

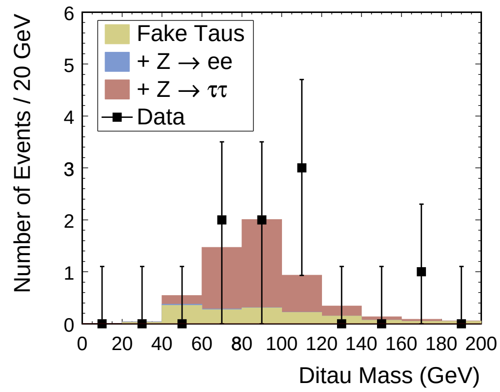

Figure 8.4: *Di-tau mass reconstruction for events in the non-back-to-back region. All confidence levels are quoted in pb. The efficiencies shown do not include branching ratios.*

the cross section do improve with increasing mass since the efficiency improves, but we are less sensitive to the MSSM theory at higher mass due to the steeply falling predicted cross section. At $m_A = 100$ GeV, where the Higgs mass is nearly on top of the Z mass and so the mass reconstruction does not give any improvement, the expected limit from the binned likelihood in the non-BTB region is approximately 2.4 times worse than the expected limit from the counting experiment including non-BTB and BTB events. At $m_A = 140$ GeV, which is approximately 2 RMS away from the Z in the di-tau mass variable, the expected limit from the binned likelihood using the non-BTB events is 2.1 times worse than the counting experiment limit, showing a modest improvement, but still not coming close to the limit extracted from the counting experiment.

Mass GeV	Cross Section pb	Eff. %	95% CL stat. only Exp.	95% CL w/ syst. Exp.	95% CL stat. only Obs.	95% CL w/ syst. Obs.
100	122	0.093	2470	2660	4170	4410
110	64.3	0.10	2210	2360	3980	4200
120	44.1	0.105	2010	2150	3800	4050
140	17.8	0.12	1615	1710	3200	3420

Table 8.6: *95% CL limits vs.* m_A *for* $\tan\beta = 50$. *All confidence levels are quoted in pb. The efficiencies shown do not include branching ratios.*

Limit vs. $\tan\beta$

Table 8.7 shows the upper limits obtained from the binned likelihood for two different values of $\tan\beta$. Again, we cannot scale the sensitivity with $(\tan\beta)^2$ because the efficiency is degraded at higher $\tan\beta$.

Mass (GeV)	Cross Section pb	Eff. (%)	95% CL (stat only) Exp.	95% CL (w/ syst) Exp.	95% CL (stat only) Obs.	95% CL (w/ syst) Obs.
50	17.8	0.12	1615	1710	3200	3420
80	65.9	0.09	2330	2920	4530	5980

Table 8.7: *95% CL limits vs.* $\tan\beta$ *for* $m_A = 140$. *All confidence levels are quoted in pb. The efficiencies shown do not include branching ratios.*

Chapter 9

Conclusions

9.1 Conclusions

We select a sample of di-tau events from a high-E_T electron triggered Run 1b data set and perform a search for neutral Higgs bosons in the MSSM.

Physics-dominated backgrounds are generated in Pythia 6.203 and modeled in a parameterized detector simulation. The modeling of variables that are used in the event selection are verified by comparing Z data control samples to Z MC samples. In some cases, a scale factor was necessary and in others, agreement was forced through the use of the acceptance rejection Monte Carlo technique. Detector-dominated backgrounds are estimated by measuring fake rates in the data sample itself.

The data sample is divided into two parts: events where the tau candidates are back-to-back and events where the tau candidates are not back-to-back. Events are subject to the same selection criteria in both regions with the exception of the $\not{E}_{l,h} > 0$ requirement which is only valid for non-back-to-back events. A counting experiment was performed using both back-to-back and non-back-to-back events and this is where the best limits are set. However, these limits do not surpass those set in the previous CDF search for Higgs bosons in the MSSM in the $b\bar{b}b\bar{b}$ channel.

We clearly observe $Z \to \tau\tau$ in the data in both the full sample and in the non-back-to-back sub-sample. This is a necessary first step in this di-tau search. At a benchmark parameter space point, $m_A = 100$ and $\tan\beta = 50$, we are sensitive to a cross section 9 times that predicted in the MSSM (1100 pb compared to the predicted 122 pb). The observed limit at this parameter space point is 891 pb. The limit on the cross section improves with increasing mass because the efficiency improves at higher mass. However, the sensitivity to the theory at higher mass is worse because the cross section falls so steeply.

Since the MSSM cross section is proportional to $(\tan\beta)^2$, it is tempting to scale the sensitivity by this factor at higher $\tan\beta$. However, the efficiency is lower and the systematic error higher as $\tan\beta$ is increased due to a broadening width and an enhanced tail at low $\sqrt{\hat{s}}$. Therefore, the sensitivity is worse at higher $\tan\beta$ than one would naively expect.

Using events where the tau candidates are not back-to-back, a di-tau mass reconstruction is performed for the first time in hadronic collider data. However, the modest sensitivity that one gains from a limit binned in mass is not nearly enough to make up for the hit in efficiency taken when only non-back-to-back events are considered. At $m_A = 100$ GeV, the binned mass limit at $\tan\beta = 50$ from non-back-to-back events alone is 2.4 times worse than from the full counting experiment. At $m_A = 140$ GeV, $\tan\beta = 50$, the binned mass limit is 2.1 times worse, showing a modest improvement as the Higgs mass is moved away from the Z mass.

Bibliography

[1] LSND Collaboration, (C. Athanassopoulos *et al.*, "Evidence for $\nu_\mu \to \nu_e$ Neutrino Oscillations from LSND," Phys.Rev.Lett.81:1774-1777,1998.

[2] Martin, Stephen P., "A Supersymmetry Primer," hep-ph/9709356.

[3] John F. Gunion, Howard E. Haber, Gordon Kane, Sally Dawson, "The Higgs Hunter's Guide," Redwood City, California, Addison-Wesley Publishing Company.

[4] ALEPH, DELPHI, L3 and OPAL Collaborations, The LEP Working Group for Higgs Boson Searches, "Search for the Standard Model Higgs Boson at LEP" Submitted to Phys.Rev.Lett.

[5] Spira, M., "HIGLU: A Program for the Calculation of the Total Higgs Production Cross Section at Hadron Colliders via Gluon Fusion including QCD Corrections," hep-ph/9510347.

[6] From Aaron Dominguez's thesis, http://hep.ucsd.edu/thesis/aaron.html.

[7] "The Review of Particle Physics," K. Hagiwara et al., Phys. Rev. D 66, 010001 (2002).

[8] ALEPH, DELPHI, L3 and OPAL Collaborations, The LEP Working Group for Higgs Boson Searches, "Searches for the Neutral Higgs Bosons of the MSSM: Preliminary Combined Results Using LEP Data Collected at Energies up to 209 GeV," hep-ex/0107030.

[9] The CDF Collaboration (T. Affolder *et al.*), "Search for Neutral Supersymmetric Higgs Bosons in p Anti-p Collisions at $\sqrt{s} = 1.8$ TeV," Phys.Rev.Lett.86:4472-4478,2001.

[10] C.W. Smith & C.D. Curtis, "Operation of the Fermilab H^- Magnetron Source," Proc. 4th Int. Symp. on the Production and Neutralization of Negative Ions and Beams, Brookhaven, US, AIP Conf. Proc. No. 158, (1986) 425.

[11] K. Junck, et. al., "Commissioning and First Operational Experience of the 400-MeV Linac at Fermilab," FERMILAB-Conf-94-181 (1994).

[12] H. Edwards, "The Tevatron Energy Doubler: A Superconducting Accelerator," Ann. Rev. Nucl. Part. Sci. 35 (1985) 605.

[13] M.D. Church & J.P. Marriner, "The Antiproton Sources: Design and Operation," Ann. Rev. Nucl. Part. Sci. 43 (1993) 253.

[14] A. Ruggiero, "The Fermilab Tevatron I Debuncher Ring," IEEE Trans. Nucl. Sci. 30 (1983) 2478.

[15] B. Austin, et. al., "Fast Betatron Cooling in the Debuncher Ring," IEEE Trans. Nucl. Sci. 30 (1983) 2478.

[16] A. Ando, et. al., "Design of an 8-GeV Accumulator Ring for the Fermilab Tevatron I Project," IEEE Trans. Nucl. Sci. 30 (1983) 2031.

[17] Particle Data Group, "High-Energy Collider Parameters," Phys. Rev. D 54, 128 (1996).

[18] L. Balka, et. al., "The CDF Electromagnetic Calorimeter," Nucl. Inst. Meth. A267 (1988) 272.

[19] S. Bertolucci, et. al., "The CDF Central and Endwall Hadronic Calorimeter," Nucl. Inst. Meth. A267 (1988) 301.

[20] P. Azzi, et. al., "SVX$'$: The New CDF Silicon Vertex Detector," Nucl. Inst. Meth. A 360 (1995) 137.

[21] F. Bedeschi, et. al., "Design and Construction of the CDF Central Tracking Chamber," Nucl. Inst. Meth. A 271 (1988) 387.

[22] G. Ascoli, et. al., "CDF Central Muon Detector," Nucl. Inst. Meth. A268 (1988) 33.

[23] J.D. Lewis, et. al., "The 1992 CDF Muon System Upgrade," CDF public note CDF/PUB/MUON/PUBLIC/2858 (1994).

[24] D. Cronin-Hennessy, A. Beretvas and P.F. Derwent, "Luminosity Monitoring and Measurement at CDF," Nucl. Instrum. Meth. A 443 (2000) 37.

[25] D. Amidei, et. al., "A Two Level FASTBUS Based Trigger System for CDF," Nucl. Instrum. Methods Phys. Res. A 269 (1988) 68.

[26] J. Carroll, et. al., "The CDF Level 3 Trigger," Nucl. Instrum. Methods Phys. Res. A 300 (1991) 552.

[27] http://www-cdf.fnal.gov/grads/tips/thesis_tips.html#cdfpics

[28] For a nice little book on the history of particle accelerators and the limitations of each type of machine, see "Accelerators: Machines of Nuclear Physics," Robert R. Wilson and Raphael Littauer, Garden City, New York, Anchor Books Doubleday & Company, Inc, 1960.

[29] The CDF Collaboration (A. Acosta *et al.*), "Search for Long-lived Charged Massive Particles in $\bar{p}p$ Collisions at $\sqrt{s} = 1.8$ TeV," Phys.Rev.Lett.90:131801,2003.

[30] http://www-cdf.lbl.gov/cdf_svx/cdf_svx.html.

[31] A study of the physics impact of the material in the silicon detector was performed by David Stuart, internal note /CDF/DOC/TRACKING/PUBLIC/5268.

[32] This study comparing material estimates with conversion data was performed by CDF collaborators Vivek Tiwari, Manfred Paulini and Barry Wicklund.

[33] T. Sjöstrand, P. Edén, C. Friberg, L. Lönnblad, G. Miu, S. Mrenna and E. Norrbin, Computer Physics Commun. 135 (2001) 238.

[34] D. Saltzberg, Pub. Proc. 9th Topical Workshop on Proton-Antiproton Collider Physics, Univ. of Tsukuba, Tsukuba, Japan, Oct. 18-22, 1993. FERMILAB-CONF-93/355-E.

[35] CDF Collaboration, "Search for Charged Higgs Boson Decays of the Top Quark using Hadronic Decays of the Tau Lepton," Phys.Rev.Lett.79:357-362, 1997.

[36] CDF Collaboration (F.Abe et al.), "Properties of Jets in W Boson Events from 1.8-TeV Anti-p p Collisions," Phys.Rev.Lett.79:4760-4765,1997.

[37] The CDF Collaboration, "Evidence for Top Quark Production in Anti-p p Collisions at $\sqrt{s} = 1.8$ TeV," Phys.Rev.D50:2966-3026,1994. Note that we do not use the corrections for underlying event or for energy loss outside of the cluster cone.

[38] R.K. Ellis, I. Hinchliffe, M. Soldate and JJ. Van Der Bij, "Higgs Decay to $\tau^+\tau-$: A possible signature of intermediate mass Higgs bosons at high energy hadron colliders," Nucl. Phys. B297(1988)221-243.

[39] CMS Technical Proposal, CERN/LHCC 94-38, December 1994, pp.191-192.

[40] "ATLAS Detector and Physics Performance Technical Design Report," http://atlas.web.cern.ch/Atlas/GROUPS/PHYSICS/TDR/access.html.

[41] D. Cronin-Hennessy, A. Beretvas, "Luminosity at CDF," CDF/DOC/CDF/CDFR/4721.

[42] Tania Moulik and Pasha Murat, "CDF Run II interface to TAUOLA, a decay library for polarized tau leptons," CDF/DOC/MONTECARLO/PUBLIC/5719.

[43] H. Baer, F. Paige, S. Protopopescu, X. Tata, "Isajet 7.48: A Monte Carlo Event Generator for pp, $\bar{p}p$, and e^+e^- Reactions," BNL-HET-99-43, FSU-HEP-991218, UH-511-952-00, hep-ph/0001086.

[44] Conversations with Steve Mrenna.

[45] A. Affolder, et al, "The Transverse Momentum and Total Cross Section of e^+e^- Pairs in the Z-Boson Region from P Anti-P Collisions at $\sqrt{s} = 1.8$ TeV," Phys.Rev.Lett. 84 (2000) 845-850.

[46] W.K. Sakumoto, P. de Barbaro, A. Bodek, H.S. Budd and J. Liu, internal note CDF4561.

[47] Wahl, John, "Electron Identification and Trigger Efficiencies in the R Analysis," CDF/ANAL/ELECTROWEAK/CDFR/4601.

[48] Leslie Groer, Ph.D. Thesis, Rutgers University, October 1998.

[49] "Comparison of Run1b Isolated Pions to Previous Studies and QFL Monte Carlo," C. Loomis, CDF/ANAL/JET/CDFR/3554.

[50] This method was suggested by Michael Spira through personal communication.

[51] A.Anastassov, S.Baroiant, M.Chertok, J.Conway, M.Goncharov, D.Jang, T.Kamon, V.Khotilovich, R.Lander, A.Lath, P.Murat, T.Ogawa, C. Pagliarone, G.M.Piacentino, F.Ratnikov, A.Safonov, A.Savoy-Navarro, J.R.Smith, D.Toback, S.Tourneur, E.Vataga, The CDF Collaboration"Selection of Tau Leptons with the CDF Run 2 Trigger System," Pub Proceeding of 9th Pisa Meeting on Advanced Detectors - La Biodola, Isola d'Elba, Italy, May 25-31, 2003.

[52] Talk given by Yuri Gershtein in, A.Astbury, B.A.Campbell, F.C.Khanna and M.G.Vincter (eds), "From Particles to the Universe. Proceedings of the 2000 Lake Louise Winter Institute", World Scientific (2000) 580 pp.

Appendix A

List of Selected Events

Run	Event
69781	824287
66392	210719
68265	656695
63188	529204
66064	267599
66225	239611
67534	98568
65259	283224
65601	196110
69878	121976
60634	174808
66615	35666
68374	215259
66248	249359
60746	195825

Table A.1: *Run and event numbers for the events that pass all of our cuts in the back-to-back region. Continued in Table A.2*

Run	Event
61271	262010
65495	66218
61073	132248
63719	73906
67476	236378
63418	13719
70541	62988
60486	104135
65298	223879
66185	403985
67757	256494
65834	616669
61270	361394
61069	41585

Table A.2: *Continued from Table A.1 and continued again in Table A.3. Run and event numbers for the events that pass all of our cuts in the back-to-back region.*

Run	Event
60952	45350
63625	646002
63522	439903
63650	88551
63650	279614
68805	70261
63581	404043
57711	98929
56914	97146
64400	40085

Table A.3: *Continued from Table A.2. Run and event numbers for the events that pass all of our cuts in the back-to-back region.*

Run	Event
64146	247097
69464	16881
70986	29711
68939	339389
64205	391756
57537	160264
58367	19919
70543	6568

Table A.4: *Run and event numbers for the events that pass all of our cuts in the non-back-to-back region.*

Appendix B

Selection of Data and Simulated Samples

All MC samples were generated in Pythia 6.203 and the detector was simulated in QFL.

B.1 Higgs Production

We generate the Standard Model Higgs direct production process, but fix the couplings to fermions to correspond to the $\tan\beta$ we are interested in. We force the Higgs to decay to two taus, and one tau to decay to an electron.

B.2 $Z \rightarrow ee$ Samples

Throughout this note, we use $Z \rightarrow$ data samples and compare with $Z \rightarrow ee$ MC events. We outline here how these samples are selected.

B.2.1 Data

We use two $Z \rightarrow ee$ data samples for the studies presented in this note, one with looser cuts, with more statistics but higher background contamination, and one with tighter cuts with fewer statistics but higher purity. Both samples require that there be one electron in the event passing all the identification requirements in Table B.1. We call this the *first electron*.

Loose $Z \rightarrow ee$ Data Sample

A "loose" $Z \rightarrow ee$ sample is used for studying electron ID variables. On this sample, we require that a *second electron* passes the loose requirements in Table B.2 and that the first and second electrons reconstruct a mass consistent with the Z mass. 3424 events make up the Loose $Z \rightarrow ee$ Data Sample.

To get an idea of the level of background present in the Loose $Z \rightarrow ee$ Data Sample, we look at how many events pass the same cuts, except with a same-sign requirement on the electron candidates. 133 same-sign events pass all other cuts,

Event is in the good run list
Event passes Level 2 trigger
First electron:
Central
Passes fiducial cuts
$E_T > 20$ GeV
$E/p < 1.8$
$E_{HAD}/E_{EM} < 0.05$
$Lshr < 0.2$
$\chi^2_{strip} < 10.0$
$\lvert\delta x\rvert < 1.5$ cm
$\lvert\delta z\rvert < 3.0$ cm
Electron is not a conversion candidate
Iso < 0.1

Table B.1: *Cuts imposed to select pure sample of $Z \to ee$ events for electron ID studies.*

Second Electron:
Central
$E_T > 20$
Passes fiducial cuts
Track is opposite charge from that of first electron
$66 < M_{ee} < 116$

Table B.2: *Cuts imposed on the second electron to select the Loose $Z \to ee$ Data and MC Samples.*

Second Electron:
All Electron ID cuts in Table B.1 Track is opposite charge from that of first electron
$66 < M_{ee} < 116$

Table B.3: *Cuts imposed on the second electron to select the Tight $Z \to ee$ Data and MC samples.*

which means that the Loose $Z \to ee$ Data Sample contains backgrounds at the ≈4% level.

Tight $Z \to ee$ Data Sample

A "tight" $Z \to ee$ sample is used for studying electron ID variables. On this sample, we make stringent electron identification requirements on both electrons, and require that they reconstruct a mass consistent with the Z mass.

The cuts which form the Tight $Z \to ee$ Data Sample are those made on the first electron listed in Table B.1 and those made on a second electron in the events, summarized in Table B.3. 1820 events make up the tight $Z \to ee$ sample. If we reverse the opposite-sign requirement, 2 events pass, so this sample is 99.9% pure.

B.2.2 MC

At the generator level, we require that each event contains an electron with $p_T > 16$ GeV and $|\eta| < 1.2$. We only generate events with $\sqrt{s} > 20$ GeV.

After simulation, these MC events must pass the same requirements as do the data events to be considered in the loose and tight samples.

B.3 $Z \to \mu\mu$ Samples

$Z \to \mu\mu$ Data and MC Samples were used to check isolation variables against $Z \to ee$ samples.

B.3.1 $Z \to \mu\mu$ Data Sample

The cuts in Tables B.4 and B.5 make up the $Z \to \mu\mu$ Data Sample used in these studies. 1992 events make up the $Z \to \mu\mu$ Fata sample. 12 events passes all of the same cuts with a same-sign requirement reversed, so the level of QCD background is $\lesssim$1%.

B.3.2 $Z \to \mu\mu$ MC Sample

At the generator level, we require that each event contains an electron with $p_T > 16$ GeV and $|\eta| < 1.2$. We only generate events with $\sqrt{s} > 20$ GeV. After simulation, these MC events must pass the same requirements as do the data events to be considered in the loose and tight samples.

Event is in the good run list	
Event passes Level 2 trigger	
First muon:	
Central	
$p_T > 20$ GeV	
$\|\Delta x_{CMU}\| < 2.0$ cm	
$\|\Delta x_{CMP}\| < 5.0$ cm	
$\|Z_0 - Z_v\| < 5.0$ cm	
$\|Z_v\| < 60$ cm	
If $p_T < 100$:	If $p_T > 100$:
$E_{EM} < 2$ GeV	$E_{EM} < 2.0 + 0.0115 \times (p_T - 100 \text{ GeV})$
$E_{HAD} < 6$ GeV	$E_{HAD} < 6.0 + 0.028 \times (p_T - 100 \text{ GeV})$

Table B.4: *Cuts imposed on the first muon to select the $Z \to \mu\mu$ Data and MC Samples for studying isolation variables.*

Second Muon:	
$\|\eta\| < 1.2$	
$p_T > 20$ GeV	
$\|Z_0 - Z_v\| < 5.0$ cm	
$\|Z_v\| < 60$ cm	
Track is opposite charge from first muon	
Track hits in 3/5 axial super-layers of CTC	
If $M_{\mu\mu} < 110$ GeV:	$M_{\mu\mu} > 110$ GeV:
$I = E_T^{cone} - E_T^{cluster} < 4$ GeV	$I/p_T < 0.1$
$66 < M_{\mu\mu} < 110$ GeV	
Reject cosmic candidates	

Table B.5: *Cuts imposed on the second muon to select the $Z \to \mu\mu$ Data and MC Samples for studying isolation variables. Cosmic rejection requirements are summarized in Table B.6*

Cosmic Rejection	
TDC_{top} and TDC_{bottom} Available	Only TDC_{top} or TDC_{bottom} Available
$-12 \leq TDC_{\mu_1\mu_2} \leq 20$ ns	$-12 \leq TDC_{\mu_1(\mu_2)} \leq 20$ ns
$\Delta TDC \geq -10$ ns	N/A
$\lvert\eta_{b-b}\rvert \geq 0.1$ or $\lvert\phi_{b-b}\rvert \geq 0.0175$	$\lvert\eta_{b-b}\rvert \geq 0.2$ or $\lvert\phi_{b-b}\rvert \geq 0.035$
$\lvert Z_{\mu_1} - Z_{\mu_2}\rvert \geq 10$	

Table B.6: *Cuts imposed to reject cosmics from the $Z \to \mu\mu$ Data Sample.*

B.4 MC Sample and Data Control Samples for Tau Efficiencies and Fake Rates

B.4.1 $Z \to \tau\tau$ MC Sample

For the $Z \to \tau\tau$ MC Sample used for the studies of tau efficiencies and fake rates, we include all cuts used in the analysis up to but not including the tau ID cuts. The cuts we impose are:

- Good run
- L2 high-E_T electron trigger
- ≥ 1 electron passing stringent identification cuts with $E_T > 20$ GeV

- Reject $Z \to ee$ candidate events

- $N_{jets} < 3$

B.4.2 W + jets Data

For the $W \to e\nu$+jets ($W \to \mu\nu$+jets) Data Samples, we include the following initial selection cuts:

- Good run

- L2 high-E_T electron trigger

- ≥ 1 electron (muon) passing stringent selection cuts with E_T (p_T) > 20 GeV

- Reject $Z \to ee$ ($Z \to \mu\mu$) candidate events

- $N_{jets} < 3$

- ${\not{E}_T}^{uncorr} > 30$ GeV

- $M_T > 60$ GeV

These set of cuts select events which are actually inside the signal region. However, the contribution from $Z \to \tau\tau$ is expected to be small, and the contribution from $A/h \to \tau\tau$ over an order of magnitude smaller. In each W+jets sample ($\to e\mu$ and

$\rightarrow \mu\nu$), there are approximately 100 events with a jet that fakes a tau. Approximately one of these is expected to be a $Z \rightarrow \tau\tau$ event due to the tight cuts on ${\not{E}_T}^{uncorr}$ and M_T.

B.4.3 Conversion Data

For the Conversion Sample, we include the following initial selection cuts:

- Good run
- L2 high-E_T electron trigger
- ≥ 1 electron passing strigent selection cuts
- Electron is a conversion candidate
- Reject $Z \rightarrow ee$ candidate events
- $N_{jets} < 3$

B.4.4 Jet Data Samples

For the jet data samples (Jet20 and Jet50), we only make the following two requirements for the event to be considered for the fake rate measurement:

- Good run

- L2 Jet trigger

When comparing fake rates and efficiencies between different analysis, it is important to pay attention to how the jets or taus in the "denominator" of the measurement are selected. We begin with a set of initial selection cuts, which are different for each sample.

We then consider all jet clusters (with a clustering cone of $\Delta R = 0.4$) with $E_T > 7$ GeV and make the following cuts to construct a sample of jets from which we measure the tau ID efficiencies. These cuts are made mainly to factor fiducial effects out of our efficiencies.

- $Z \to \tau\tau$ MC Sample only: Jet is within $\Delta R < 0.4$ of the direction of the visible energy from a tau, and that tau must decay hadronically.
- Lepton Samples: ΔR(tight lepton, jet) > 0.7[1]
- Lepton Samples: $|z_0^{\text{jet}} - z_0^{\text{tight lepton}}| < 5.0$ cm[2]
- Jet uncorrected $E_T > 7$ GeV[3]

[1] If there is more than one lepton in the event that passes the stringent lepton identification requirements, the lepton with the highest E_T is called the tight lepton.

[2] z_0^{jet} is defined to be the z_0 of the highest p_T track within $\Delta R < 0.4$ of the jet direction.

[3] This cut is set to $E_T > 10$ GeV in the analysis, but we loosen the cut for these studies to allow the cut to be lowered when the cuts are tuned. 7 GeV is the minimum jet E_T set in the jet clustering algorithm.

- At least one track within $\Delta R(\text{track, jet}) < 0.4$ must satisfy:
  - $p_T > 1$ GeV
  - $\eta_d^{\text{track}} < 1.1$
  - $|z_0^{\text{track}} + 130/\tan\theta^{\text{track}}| < 150$ cm (track stays in CTC fiducial)
  - Track passes the fiducial requirements designed for electron candidates
- $\eta_d^{\text{jet}} < 1.1$
- $|z_0^{\text{jet}}| < 60$ cm

Additional Requirements on Jet Samples: Removing Trigger Bias

We do not want the fake rates that we measure to be biased by the jet trigger requirements. Therefore, a jet from the Jet20 or Jet50 sample must pass the following requirements, in addition to those listed in Section B.4.4.

- Jet20 only: Jet is not the highest E_T jet in the event (special cuts are made on these jets at the trigger level).
- At least one other jet in the event is a "trigger-able" jet. A trigger-able jet satisfies the following requirements:

– The jet direction when clustered offline is within $\Delta R < 0.4$ of a jet passing the trigger requirements at L2.

– Jet20 (Jet50): L2 Jet $E_T > 20$ (50) GeV

Appendix C

Combinatorics Issues for Measuring Efficiencies from $Z \to ee$ Samples

C.1 Finding the Efficiency of the Stringent Electron Identification Cuts

When measured from events which contain two electrons, efficiencies need to be derived taking combinatorics into account. We use the method described in [47]. In the study outlined in Section 4.3.10, we begin with a sample of n events from the Loose $Z \to ee$ Data or MC Sample. These events contain at least one electron that passes the stringent electron identification requirements (called the *first electron*), and one electron which is only required to pass loose cuts. In the case where two electrons pass the stringent electron identification requirements, the highest E_T electron is called the first electron. We would like to measure the efficiency of these same stringent electron identification cuts using the second electron. Suppose the second electron passes the cuts in k events. Then in $m = n - k$ events, the second electron does not pass. The efficiency of this cut is given by

$$\epsilon = \frac{2 \times k}{m + 2 \times k} \tag{C.1}$$

This can be understood if you consider that there is only one way for both electrons to pass, but there are two ways for one electron to pass and the other to fail (the first electron passes and the second fails, or the first electron fails and the second passes). So the efficiency which one would naively expect:

$$\epsilon = \frac{k}{m + k} \tag{C.2}$$

needs to be modified by dividing the number where the second electron fails (m) by 2, which gives

$$\epsilon = \frac{k}{\frac{m}{2} + k} \tag{C.3}$$

which is equivalent to Equation C.1.

C.2 Finding the Efficiency of a Subset of the Electron ID Cuts

Where we quote the efficiency of a single electron ID cut which is a member of the set of stringent electron identification cuts, we again use equation C.1, where now k is the number of events where the second electron passes the single cut we are interested in and m is the number where the second electron fails. While not convinced that this is the proper equation to use in this instance, the efficiency of a single electron ID cut is not used anywhere in the analysis. The numbers are shown in tables only for comparison with previous analyses.

C.3 Finding the Efficiency of a Cut Which is Not Part of Electron Identification Cuts Made on the First Electron

For the efficiency of a cut which is not part of the stringent electron identification cuts made on the first electron, such as the tracking isolation cut or to determine the effect of our electron rejection on electrons, we simply consider the second electron and take the efficiency to be the ratio of the number that pass to the total number of events.

Appendix D

Prospects for Run 2a and the LHC

At the time of this writing, the Run 2 phase of data taking at the Tevatron has delivered more than twice the Run 1 integrated luminosity to CDF and DØ. The Large Hadron Collider (LHC) in Geneva, Switzerland is scheduled to begin colliding proton beams in 2007 at a center-of-mass energy of 14 TeV. Here we discuss the prospects for searches for $A/h \to \tau\tau$ at the Tevatron and the LHC.

D.1 Run 2a

D.1.1 Triggers

Both CDF and DØ have installed triggers that will allow the experiments to more efficiently record di-tau events. One of the major hits in efficiency in the Run 1 analysis appears at the trigger level where we require an electron with $E_T > 18$ GeV in the central region of the detector from a tau decay. Electrons from such decays tend to be much softer, typically $\sim$ 10 GeV, and so the efficiency of this high-E_T trigger on $A/h \to \tau\tau$ events is only 20%.

The tau triggers implemented at CDF [51] include an electron plus track trigger, a muon plus track trigger, a trigger requiring two hadronic tau candidates and one requiring a hadronic tau and $\not\!\!E_T$. The latter is designed for $W \to \tau\nu$ events, but the other three will improve the efficiency in the $A/h \to \tau\tau$ channel with thresholds at $p_T > 8$ GeV for the electrons and muons and $p_T \gtrsim 6$ GeV for the hadronic tau candidates. We find from Pythia MC that lowering the lepton p_T threshold from 18 GeV to 8 GeV increases the trigger efficiency from 20% to 40% for parameter point $m_A = 100$ GeV, $\tan\beta = 50$. The hadronic tau candidates are required to be isolated in a three-dimensional annulus between 10° and 30° surrounding a seed track. DØ has also implemented lepton + track triggers with similar thresholds [52].

Notice that the new trigger systems allow the all-hadronic decay mode (where both taus decay hadronically) to be included in this analysis. Since taus decay hadronically 65% of the time, all-hadronic modes account for $(65\%)^2 = 42\%$ of di-tau decays. The muon channel, which will also be new in Run 2b, is $2 \times 17\% \times 65\% = 22\%$ of the branching ratio. Recall that the branching ratio for the electron decay mode is $2 \times 18\% \times 65\% = 24\%$, so a Run 2 $A/h \to \tau\tau$ analysis can expect a factor of 3.7

increase in acceptance due to the addition of new decay modes.

D.1.2 Fake Tau Systematic

The largest systematic in this analysis comes from estimating the rate of backgrounds where a QCD jet fakes a hadronically decaying tau. Recall that fake rates measured from data control samples differ by a factor of 2 depending on the control sample under consideration. The $W \to e\nu$+jets, $W \to \mu\nu$+jets and Conversion Samples show tau fake rates that are a factor of 2 higher than those measured in the Jet20 and Jet50 Samples. It is unclear whether this difference is inherent in the physics processes that brought about each sample or if it is a bias from the triggers (notice that the former three samples were triggered with leptons and the latter two were triggered with jets).

Confirming the discrepancy in samples generated from MC would verify that the difference does indeed come from physics and not from triggers, if such is the case. However, note that in the Run 1 analysis, even if we had known that the discrepancy is inherent in the physics processes, then this would not have reduced the fake tau systematic. This is because the relative contribution to the fake tau background from different processes (conversions, $W \to e\nu$+jets, and events with one fake electron and one fake tau) was not determined. A study is underway at CDF using Run 2 data to estimate the relative contribution of the different background processes in a $Z \to \tau\tau$ search based on lepton isolation variables. Once these relative rates are known, and *assuming that the difference in fake rates comes from the physics processes*, then one could reduce the fake tau systematic by applying different fake rates to backgrounds with "real" and "fake" leptons, the former being measured from the lepton-triggered samples and the latter being measured from the jet-triggered samples.

If the difference in fake rates is not confirmed in MC samples, then it may be due to a trigger bias. The wider variety of triggers available in Run 2 may facilitate locating the origin of this bias.

D.1.3 Luminosity

The increased luminosity in Run 2a will of course improve the sensitivity for the counting experiment. Taking the current baseline projection of 2 fb^{-1} per experiment by 2008, we find a factor of 20 increase in statistics for the CDF analysis.

D.1.4 Sensitivity

We estimate the expected sensitivity for the $A/h \to \tau\tau$ search in Run 2b at CDF simply based on lowered trigger thresholds, the availability of additional decay channels, and the increase in luminosity. To be conservative, we assume that all of the systematics in the Run 1 analysis will still be present in Run 2. For the counting experiment, the 95% CL limit is proportional to:

$$\left(\frac{s}{\sqrt{\sum_i b^i + (\sum_i f_i b^i)^2}}\right)^{-1} \tag{D.1}$$

where s is the number of expected signal events for a given model at a given luminosity, b^i is the number of background events expected for a background type i and f_i is the fractional systematic error on each background. Refer to Table 8.1 for a summary of the systematics in the Run 1 analysis. For Run 2, we take $f = 0.67$ for fake tau backgrounds and $f = 0.07$ for $Z \to \tau\tau$ (same as Run 1). Since both s and b^i are proportional to the total integrated luminosity, branching ratio, and efficiency, the expected 95% CL limit on the signal cross section in Run 2b may be found from:

$$\frac{\sigma_{2b}}{\sigma_1} = \frac{L_1 B_1^s \epsilon_1^s}{L_{2b} B_{2b}^s \epsilon_{2b}^s} \times \frac{\sqrt{\sum_i L_{2b} B_{2b}^i \epsilon_{2b}^i b_{2b}^i + \sum_i (f_i L_{2b} B_{2b}^i \epsilon_{2b}^i b_{2b}^i)^2}}{\sqrt{\sum_i L_1 B_1^i \epsilon_1^i b_1^i + \sum_i (f_i L_1 B_1^i \epsilon_1^i b_1^i)^2}} \tag{D.2}$$

where the 1 (2b) subscript denotes Run 1 (Run 2b), so we take $L_1/L_{2b} = 20$. Under each square root sign, the first sum represents the statistical error and the second sum the systematic errors. We are assuming that the systematic errors on the signal may be neglected, which is valid for $m_A \lesssim 120$ GeV and $\tan\beta \lesssim 50$. We also neglect the $Z \to ee$ (and $Z \to \mu\mu$) background because the former was small in the Run 1 analysis.

We expect the muon triggered analysis to be similar to the electron triggered analysis presented in this thesis. We do not estimate the systematic errors for the all-hadronic mode, instead we only quote the expected sensitivity for the lepton triggered analyses combined. Adding the muon channel gives a factor of 2 increase in branching ratio, so $B_1^s/B_{2b}^s = 1/2$. As described above, the lowered trigger thresholds in Run 2b give $\epsilon_1^s/\epsilon_{2b}^s = 1/2$.

From Table 8.2, $b_1^{Z\to\tau\tau} = 42.4$ and $b_1^{fake} = 10.1$. We assume that lowering the lepton p_T threshold has the same effect on $Z \to \tau\tau$ as on $A/h \to \tau\tau$, so that $\epsilon_1^{Z\to\tau\tau}/\epsilon_{2b}^{Z\to\tau\tau} = 1/2$. We also need to know the effect of lowering this threshold on the fake tau backgrounds. We use the observed spectrum of recoil jets in the $W \to e\nu$+jets control sample, and find that lowering the E_T cut from 20 GeV to 10 GeV is a factor of 6 more efficient for these jets. We assume a similar spectrum for the fake backgrounds, so that $\epsilon_1^{fake}/\epsilon_{2b}^{fake} = 1/6$. We also assume that adding the muon trigger doubles the rate of each background type and signal, giving $B_1^s/B_{2b}^s = B_1^{Z\to\tau\tau}/B_{2b}^{Z\to\tau\tau} = B_1^{fake}/B_{2b}^{fake} = 1/2$. Inserting the numbers into equation D.2, we find that the Run 2 counting experiment actually does about a factor of 2 *worse* on a 95% CL limit than the Run 1 analysis ($\sigma_{2b}/\sigma_1 \approx 2$).

The degraded limit in the counting experiment is not a cause for concern because the larger data sample actually leads to a better limit from the binned di-tau mass reconstruction than from the counting experiment in Run 2. We perform the binned likelihood in di-tau mass as was done in the Run 1 analysis using the numbers of events and systematics predicted in Run 2. Recall that the binned likelihood considers only events in the non-back-to-back region and the counting experiment includes events from both the back-to-back and the non-back-to-back regions. For the benchmark parameter point $m_A = 100$, $\tan\beta = 50$, recall that the expected limit in the Run 1 analysis from the counting experiment was a factor of 9 from the theoretical prediction, and the limit from the mass reconstruction technique was a factor of 2.4 further from that. When a higher mass point is considered ($m_A = 140$, $\tan\beta = 50$), the mass reconstruction only shows a 15% improvement relative to the counting experiment in Run 1. For the Run 2b prediction laid out here at $m = 100$, $\tan\beta = 50$, the mass reconstruction technique is a factor of 3.0 *better* than the counting experiment, giving a limit a factor of 5.4 away from the theoretically predicted cross section. In the Run 2 prediction, as we move away from the Z mass to $m_A = 140$, $\tan\beta = 50$, the counting experiment gives a limit a factor of 80 from the theoretical prediction whereas the mass reconstruction gives a limit a factor of 7 from the theory, a dramatic improvement from the mass reconstruction. Recall that in Run 1, the best limit at this parameter point was a factor of 10 away from the theory.

These predictions are conservative since they include only the lepton channels at CDF (DØ is not included) and we make the pessimistic assumption that the systematics do not improve and background rates are not reduced.

D.2 LHC

The ATLAS collaboration has laid out their expected sensitivity to the $A/h \to \tau\tau$ in their physics technical design proposal [40]. They outline a search for events where Higgs bosons are produced directly or in association with two b quarks. They propose to search for events where one tau decays to a lepton and one tau decays hadronically, as in the Run 1 search presented in this thesis. At ATLAS, a stiff p_T cut may be made on the lepton candidate (they propose $p_T > 24$ GeV within $\eta < 2.5$) while achieving a high signal significance due to the high center-of-mass energy at the LHC.

The proposed analysis utilizes the di-tau mass reconstruction, requiring the events to pass $1.8 < \Delta\phi^{(\tau_h - lepton)} < 2.9$ or $1.8 < \Delta\phi^{(\tau_h - lepton)} < 2.9$ (this is the requirement that the taus be non-back-to-back) and $\not{E}_{l,h} > 0$. The di-tau mass must lie within ± 30

GeV of the hypothesized Higgs mass. The high center-of-mass energy at the LHC is expected to produce Higgs bosons with a stiffer p_T spectrum. Recall that a stiffer p_T spectrum means that the Higgs decay products tend to not be back-to-back, and from Figure 4.17, the di-tau mass resolution is improved. The ATLAS proposal shows a di-tau mass resolution of approximately 10% for a non-back-to-back requirement of $|\sin\Delta\phi| > 0.45$. The resolution quoted in this thesis for CDF is 22.5% for a non-back-to-back requirement of $|\sin\Delta\phi| > 0.3$. I believe that the improved resolution quoted for ATLAS is due to both a stiffer non-back-to-back requirement (ATLAS can afford to stiffen this cut because of a stiffer p_T spectrum), and the fact that the p_T of the Higgs bosons tend to be stiffer in the first place.

For $m_A = 150$ GeV and $\tan\beta = 10$, with 30 pb^{-1} of data collected, [40] reports an expected signal significance of 8.9 from the ATLAS detector, with ~ 100 signal events predicted.

Appendix E

Bayesian Limits

Here we briefly outline the procedure used to set Bayesian limits.

The likelihood function $\mathcal{L}$ is given by:

$$\mathcal{L}(\mu, N) = \sum \frac{\mu_i^{N_i} e^{-\mu_i}}{N_i!}$$

where $\mu = s + b$ is the sum of signal and background, and N is the number of events observed. The sum is over bins. For the counting experiment there is only one bin, and for the mass reconstruction in the non-back-to-back region, there are 14 bins, 10 GeV wide, from $m = 60$ GeV to $m = 200$ GeV.

The 95% CL upper limit on the number of signal events (s_{up}) is the point at which the integral from 0 to s_{up} is 95% of the total integral of the likelihood:

$$\frac{\int_0^{s_{up}} \mathcal{L}(s) ds}{\int_0^{s \infty} \mathcal{L}(s) ds} = 0.95$$

To include the effect of systematic errors, we smear μ assuming Gaussian errors for signal and background, and integrate the resulting smeared likelihood. Correlations between errors on different background types or between signal and background are taken into account.

To find the expected limit for a given parameter space point, we set the number of observed events equal to the number expected. The proper way to do this is actually to throw a (Poisson) die on the number of events observed for many tries, and take the average of the limit obtained for all tries. To the extent that a Poisson distribution is the same as a Gaussian distribution with the size of the numbers in the counting experiment, we find that we would get the same answer using either method.